Energy Yield Prediction of Solar Powered E-Bike Charging Station

Ajay Jamodkar

TU Delft Delft University of Technology

DCE&S DC systems, Energy conversion & Storage

PVMD Delft University of Technology
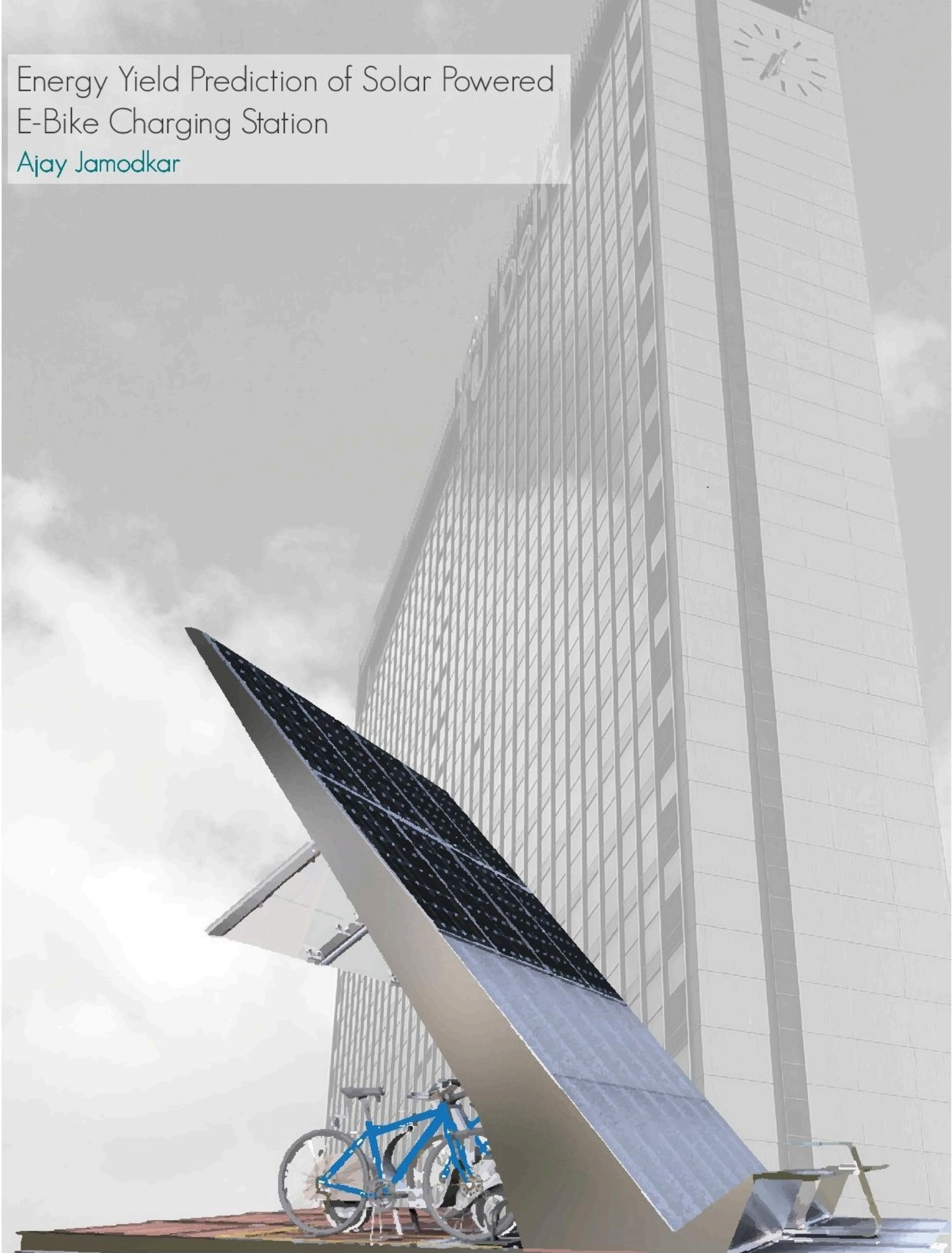
Energy Yield Prediction of Solar Powered E-bike Charging Station

by

Ajay Jamodkar

in partial fulfillment of the requirements for the degree of

Master of Science
in Electrical Sustainable Energy

at the Delft University of Technology,
to be defended publicly on Friday July 28, 2017 at 13:00 PM.

Supervisor:	Dr. Olindo Isabella	
	Dr. Rudi Santbergen	
	Dr. ir. Peter van Duijsen	
Thesis committee:	Prof. Dr. Arno Smets ,	TU Delft
	Dr. Olindo Isabella,	TU Delft
	Dr. Jianning Dong,	TU Delft

An electronic version of this thesis is available at `http://repository.tudelft.nl/`.

TUDelft Delft University of Technology

Abstract

Recent innovations in Electric Vehicles (EVs) will potentially change the future of the transportation industry. They will diversify the energy mix and reduce the dependence on fossil fuels. However, use of EVs only shifts the source of CO_2 production to electricity generation plants. A smart solution to overcome this problem is the use of localized generated power and solar-powered charging stations are the best way to achieve it.

A solar powered e-bike charging station, installed on the TU Delft campus is one such example. The charging station is equipped with a meteorological station, sensors for monitoring performance, inverters and batteries. The PV system installed at the e-bike station was thoroughly modeled, considering both the location and meteorological conditions of the final installation [1]. To maximize the station's utility, it is important to accurately predict the energy yield of the system. The modeling step comprises of several sub-models (irradiance, thermal and electrical model) which indicate the energy yield of the station as well as the power exchange with the grid. Though these models were based on (realistic) assumptions, there is a need to verify the assumptions against measured values.

In this thesis, the accuracy of existing irradiance, thermal and electrical models was evaluated by predicting the energy yield of the e-bike charging station. Further, the performance of these models, especially those related to the irradiance on the plane of the array and the instantaneous temperature of the PV modules, was improved. Also, two new decomposition models are introduced to improve the accuracy of obtaining diffuse irradiance from global horizontal irradiance specifically for the Netherlands. It was found that for accurate energy yield prediction it is necessary to optimize the models using location specific parameters like sky view factor, albedo, INOCT etc. The energy yield predicted, using the improved models in this thesis, was only 17 kWh less than the measured yield for the duration Oct'16-Apr'17.

Contents

1

Introduction

Today, renewable energy has become an essential part of the world's ongoing energy transformation. Providing sustainable, reliable and cost-effective energy is critical to meet growing energy demand and curb climate change. With the advancements in renewable energy technologies, renewables are becoming more affordable and readily available, driving their adoption around the world, especially in the power sector. For example, 90% of the investments in renewable power in 2015, were in wind and solar power. They are now competitive with conventional sources of electricity because costs have plunged in recent years. The cost of solar photovoltaic (PV) modules has fallen by 80% since 2009 and that of wind turbines by nearly a third [2]. These developments have made it possible to reach grid parity by reducing the levelized cost of electricity.

Among the various energy sources available, Photovoltaic (PV) systems, due to their modularity, scalability, low cost of maintenance and long life are emerging as a lucrative option. Significant cost reductions, accompanied by global awareness about sustainable development, have opened new markets for their rapid growth. Increase in global PV capacity from 40 GW in 2010 to 219 GW in 2015 is an example in this regard [2]. PV systems are enabling consumers not only to produce power for their needs but also to push the excess energy into the grid.

Continuous efforts to innovate and develop PV technologies that are more efficient, lighter and cheaper will enable the use of PV in non-conventional places such as on building facades, windows, roads and other surfaces. International Renewable Energy Agency (IRENA) estimates that the global solar PV capacity could reach 1,760 GW by 2030.

Following the success of solar power in the recent years, several countries are making massive investments in this sector. In the Netherlands, the share of renewable energy was just four percent, and the contribution of solar power was merely 1.4% in the year 2010. In 2011, it came up with a National Action Plan on Solar Power (NAZ), with the aim of increasing the installed capacity to 4 GWp by 2020 [3, 4]. To support this revolution, schemes like net metering, which is guaranteed till 2020, have been implemented.

1.1. Electric vehicles

The transportation industry is one of the biggest consumers of energy generated by fossil fuels. In the year 2012, 96% of the energy used by the transport sector came from fossil fuels resulting in 23% of the total current energy-related CO_2 emissions [5]. For the same year, fuel consumption by passenger vehicles alone accounted for 61% of the total world transportation energy consumption. This is a clear indication that the dependency of transport sector on traditional fuels must be decreased to achieve the sustainability goals. Recent innovations in Electric Vehicles (EVs) have proven that they can change the future of transportation industry, especially passenger vehicles, by diversifying the energy mix and reducing the dependence on fossil fuels. It is also important to recognize that the use of EVs only shifts the source of CO_2 production to electricity generation plants and the only way to completely solve the

problem is to produce the electricity in a sustainable way. In 2015, the number of electric cars (including battery-powered and plug-in hybrid vehicles) on the road crossed the global threshold of 1 million [6]. There is also a significant increase in number of Light Electric Vehicles(LEVs) or e-bikes around the globe. For instance, the Netherlands, which is also known as the bike capital of the world, has more than 22.5 million bicycles, of which 1.3 million are electrically supported whereas 8000 are fast electric bikes [7]. LEVs are popular as they are easy to use in densely populated areas and are easy to park.

1.2. Solar powered charging infrastructure

To promote the use of electric vehicles, governments and private organizations are coming together to improve the required charging infrastructure. However, traditional electricity distribution systems are not designed to accommodate such a large number of charging points for EVs, especially in urban locations [6] . A smart solution to overcome this problem is the use of localized generated power and solar-powered charging stations are the best way to achieve it.

Figure 1.1: The solar e-car charging station, located on the campus of University of IOWA, United States[8].

Figure 1.1 shows an electric car charging station installed on the campus of the University of IOWA which generates an estimated 70,000 kWh of energy annually and the same time allows for a projected reduction in gasoline use by 15,686 gallons [8]. It produces enough energy to recharge up to 40 campus utility vehicles on a sunny summer day.

In case of the Netherlands, currently most of the e-bikes are charged using the grid, causing indirect emissions. To make the charging infrastructure more sustainable, organizations are coming up with solutions like solar powered e-bike charging stations and plan to make e-bike charging less dependent on the grid. Such stations are also beneficial for the grid as they help to reduce the strain on the existing electricity network. The cost of restructuring the grid, especially in urban areas where power lines were not designed to handle the substantial and abrupt loads from charging vehicles are also reduced. Another advantage of using localized PV system is that it prevents unnecessary material waste and decreases electrical losses during transportation. Figure 1.2 shows the design and a picture of the e-bike charging station installed on the campus of TU Delft [1].

(a) Design of e-bike station [9]

(b) Original e-bike station
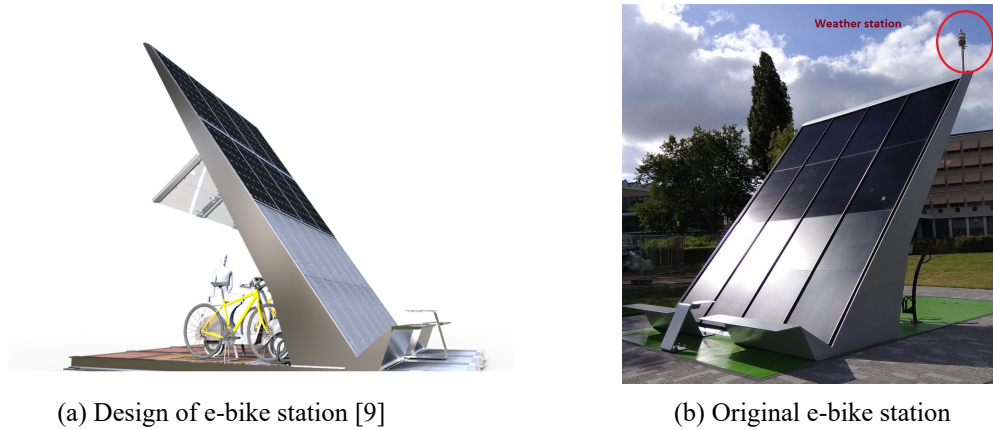
Figure 1.2: The E-bike charging station at TU, Delft.

Another purpose of this station is to carry out detailed research in the field of PV system design and contactless charging of light electric vehicles (LEVs). It is equipped with a weather station and various sensors to monitor the performance of the installed solar panels, inverters and batteries.

The PV systems used for the charging infrastructure of electric vehicles should not just operate efficiently in an urban environment, but their aesthetics should also please the eyes of the viewer. To make the system technically, financially and aesthetically viable, the most efficient design methodologies must be investigated. The following section discusses the basic design requirements for a PV system and how simulation models play a critical role in it.

1.2.1. Modeling of PV system

The design of a photovoltaic system involves a detailed analysis of parameters such as the irradiance, wind, ambient temperature and surrounding environment. Each of these factors affects the system output differently. Other factors, like the components of the system, also play an important role and are necessary to predict the overall performance. For example, a PV system installed on open ground will have more power output than a similar system installed in a location surrounded by buildings. To understand the effects of all these parameters, computer simulations and modeling are beneficial. Nowadays, with the availability of powerful computers and software, extremely complex system can be modeled and their performance can be predicted and analyzed. A typical PV system consists of several individual components like the PV module, inverters, storage system, etc.

Typically, PV system modelling is divided into three major parts as shown in figure 1.1.
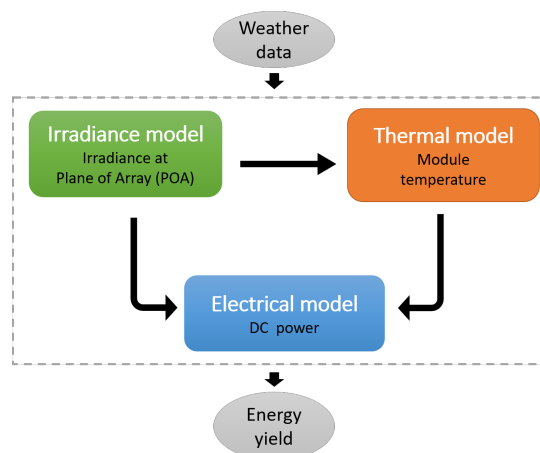
Figure 1.3: Major steps involved in modeling a PV system.

The first step of PV system modeling is irradiance modeling. It predicts the irradiance received on the Plane of Array (POA) of the solar modules. It takes care of factors like the tilt of module, movement of sun throughout the year, etc. The primary inputs to an irradiance model are measured Diffuse Horizontal Irradiance(DHI) and Direct Normal Irradiance(DNI) for a location but these data are rarely available for all the locations. On the other hand, Global Horizontal Irradiance (GHI) data is the most commonly available irradiance data, since the measurement equipment required for measuring it is simple and cost effective. Modeling irradiance on POA from just GHI data (refer fig. 1.4) involves two steps: 1) decomposing GHI into DHI and DNI using mathematical models usually referred as "Decomposition models" 2) transpose these components to POA of the modules using models referred to as "Transposition models". If both DNI and DHI are available, then the only transposition models are required.
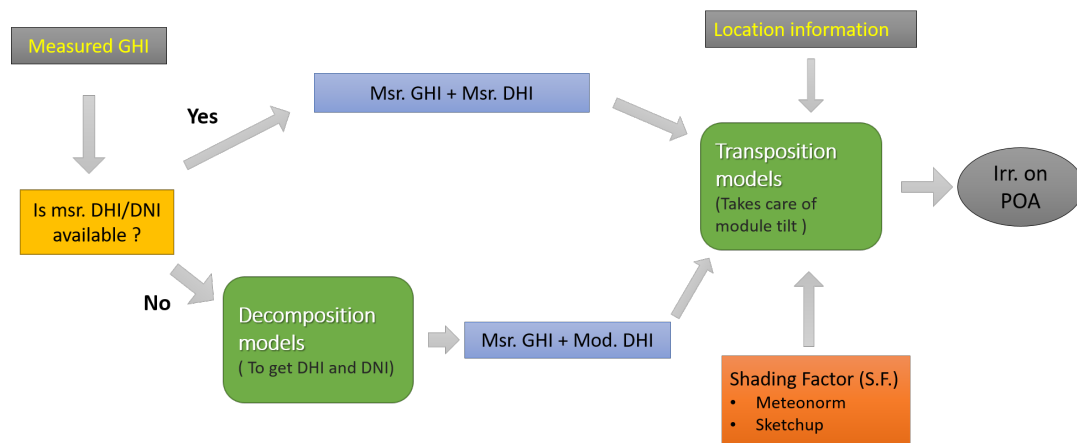
Figure 1.4: Detailed steps involved in irradiance modeling a PV system.

In the past, many decomposition and transposition models have been developed and evaluated [10–18]. However, the performance of these models is location and climate dependent and there is not much information available about their performance for the climate of the Netherlands. Transposition models also do not take care of shading due to near by objects which can lead to significant error in yield prediction in case the system is surrounded by buildings or other objects. Therefore, shading analysis, which can be done using various tools like Horicatcher and 3-D modeling, must be incorporated.

Solar cell temperature is the second most critical factor, after incident irradiance, for modeling a PV system. It directly affects the power output and efficiency of the PV module. Studies in the past have found it be dependent on several factors like incident irradiance, ambient temperature, wind speed, type of PV technology, etc. [19, 20]. There are several thermal models, available in literature to estimate temperature of the solar cells, with a varying degree of complexity [19, 21–23].

The third part of modeling is to model the power produced by the PV system. This step involves estimating the module's current-voltage (I-V) characteristics based on incident irradiance and module temperature. Many models exist to predict the electrical output of the modules. They can be broadly classified as models which are based on single diode equivalent circuits (referred to as "single diode models (SDM)") and models which estimate the change in efficiency using thermal coefficients of the module (referred to as "Point Value Model (PVM)") [19, 24–26]. The main difference between these two classes of models is that single diode models estimate the full I-V curve whereas the point value models estimate only certain points on I-V curve such as open circuit voltage (V_{oc}), short circuit current (I_{sc}) and maximum power point (P_{mpp}) [27].

As described above, one can use different combinations of irradiance, thermal and electrical models to design and predict the expected energy yield of a PV system. The performance of the models changes with the location. For example, Netherlands has a moderate maritime climate strongly influenced by the

North Sea and the warm Gulf Stream. It has a cloudy or rainy weather most of the time which directly affects the amount of irradiance received by the panels. Another peculiarity of the Dutch weather is that it is windy at all times of the year which strongly influences the temperature of the panels and hence the output of the PV system. Thus, the models and their combinations based on verified location-specific meteorological and temperature models to predict the energy yield of the PV systems need to be quantified.

1.3. Thesis Motivation

This thesis is motivated by the fact that there is an increasing need for sustainable charging stations for electric vehicles in urban areas of the Netherlands. The solar-powered charging station is an effective way to achieve this goal. The generation of power from PV systems has problems such as high investment cost for the complete system and the need to have a balance between performance and aesthetics of the system. While designing a small PV system like a charging station for LEVs in an urban location, it is critical to take care of location-specific weather and surrounding conditions. It would assure investors that the system would perform well despite highly variable weather conditions. Despite the availability of several simulation models, not all of them are verified for their effectiveness in different climatic conditions. For example, in 2008, Sandia National Laboratories evaluated the performance of various models used within the Solar Advisor Model (SAM), using measured data to study the accuracy of these models. The study, however, was specific to the PV system installed at Sandia's PV Systems Optimization Laboratory in Albuquerque, United States [28]. Albuquerque has a cold semi-arid climate which is usually sunny and dry which means that we cannot be sure that the best performing models of this study will also produce equally good results for a system in the Netherlands which has a cloudy sky most of the time [29] . Also, there is a need to find out the best practice to simulate the impact of shading effect due to surrounding buildings, etc. The focus of this thesis is to evaluate whether available irradiance, thermal and electrical models are accurate for predicting the energy yield of a solar powered system like the e-bike charging station and to suggest improvements for the same.

1.4. Research questions

1. For the climate of the Netherlands, study and improve decomposition models

   (a) Which is the most accurate decomposition model ?

   (b) What are the drawbacks of existing decomposition models and how they can be improved?

   (c) Is it possible to improve the performance of decomposition models using local irradiance data?

2. Evaluate and optimize transposition models to compute the irradiance on the plane of array of the e-bike station

   (a) Which are the most accurate transposition models to be used in urban location?

   (b) How can the performance of existing models be improved by using location-specific parameters like sky view factor and albedo?

   (c) How important is shading analysis to irradiance modeling and what is the most reliable technique to incorporate it?

   (d) What is the effect of using decomposition models instead of measured diffuse and direct irradiance?

3. Evaluate thermal models best suited for predicting module temperature of a closed system like the e-bike station

    (a) Which is the best performing thermal model?

    (b) Does the time step between data used for modeling have an impact on the performance of the models?

    (c) What is the effect of using weather data from nearby meteorological stations on the performance of thermal models?

4. Compare existing solar cell electrical models to compute the DC power and energy output of the e-bike charging station

    (a) How accurate are the existing electrical models ?

    (b) How much effect do the inaccuracies in irradiance and thermal models have on the energy yield prediction of the system?

    (c) Using the method of the designer of the e-bike station, how well does the energy yield predicted, match with the measured data after installation?

    (d) Do the improvements suggested in this thesis, improve the quality of prediction of energy yield?

1.5. Thesis outline

This report comprises of 6 chapters. Chapter 2-4 answers the research questions discussed above and chapter 6 concludes all the results obtained. A brief description of these chapters is given below:

Chapter 2- Irradiance modeling I : Decomposition models : In this chapter performance of the most commonly used decomposition models will be evaluated and modifications to improve their prediction will be suggested.

Chapter 3- Irradiance modeling II : Transposition models: This chapter deals with transposition models and effect of location specific parameters like albedo and shading due to near by objects on them.

Chapter 4- Thermal modeling: In this chapter, first, various thermal models are briefly explained. Further, they are validated with the data obtained from the thermocouples installed on PV modules. The reason for the discrepancy between the measured and predicted module temperature is analyzed.

Chapter 5- Electrical modeling : DC power and energy yield: In this chapter the energy models are evaluated based on the comparison of modeled and measured DC power and energy yield.

Chapter 6- Conclusions and Recommendation: The answers to the research questions and recommendations for future work are given in this chapter.

2

Irradiance modeling I : Decomposition models

To monitor the energy yield of a PV system in real-time, it is necessary to have information about both diffuse and direct components of the solar irradiance. However, irradiance data available in real-time, for most locations, is limited to Global Horizontal Irradiance (GHI). This has led to the development of several decomposition models to decompose GHI into diffuse or direct components. These models are composed of empirical correlations whose coefficients are typically dependent on local climatic conditions.

In this context, as mentioned in chapter 1, the following research questions are addressed :

For the climate of the Netherlands, study and improve decomposition models
- Which is the most accurate decomposition model?
- What are the drawbacks of existing decomposition models and how can they be improved?
- Is it possible to improve the performance of decomposition models using local irradiance data?

In this chapter, five different decomposition models are evaluated for the weather of the Netherlands (NL). The next section gives a brief introduction to solar irradiance measurements which is followed by a short description about existing decomposition models. Next, two newly derived decomposition models (based on the irradiance data for the Netherlands) are presented. These two models are intended to improve the accuracy of obtaining diffuse irradiance from GHI. Finally, results of the comparison between all the models will be discussed.

2.1. Solar irradiance data

To differentiate between energy and power of the solar radiation, the terms 'irradiance' and 'irradiation' are used extensively in this thesis. The term, 'irradiance' is used to denote the instantaneous solar power received per square meter of surface and is measured in W/m^2. 'Irradiation' is the integral of the irradiance over time and refers to the energy of the solar radiation in Wh/m^2 or kWh/m^2 [30]. Three main types of irradiance measurements are widely used for designing and monitoring PV systems. A brief description about them is given below.

Global Horizontal Irradiance (GHI) The total solar irradiance received by a horizontal surface on the earth is called as global horizontal irradiance. It is measured using an instrument called a pyranometer (refer #1, figure 2.1) that consists of a thermopile detector. The irradiance level is measured by translating the voltage generated across it. To measure GHI, the pyranometer is mounted horizontally so that
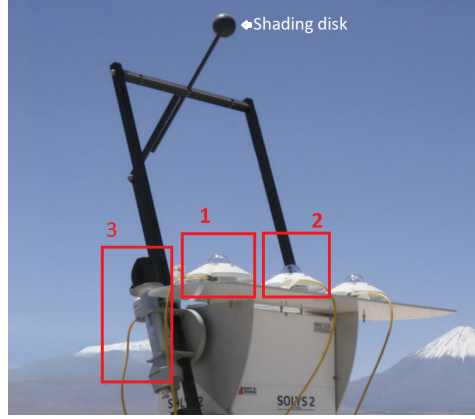
Figure 2.1: Measurement of solar irradiance.

it has a field of view of the whole hemisphere. It is the most widely available measurement because of the simplicity of the measuring equipment and its low maintenance.

Diffuse Horizontal Irradiance (DHI) is the diffuse irradiance received by a surface placed horizontally on the earth. DHI is measured using a horizontally mounted pyranometer with a shading disk to block the direct irradiance (refer #2 in figure 2.1). Measured diffuse irradiance data is rarely available due to high maintenance costs of the measuring device.

 Direct Normal Irradiance (DNI) is the direct component of the irradiance which is unaltered by the atmospheric scattering and reflection. It reaches the earth surface in a straight line and can be received by a surface by tracking the position of the sun in the sky. It is measured using a device called pyrheliometer (refer #3, figure 2.1) which works on the same principle as a pyranometer but is modified to have a limited field of view so that only a direct beam can enter it. It is mounted on a surface which is always perpendicular to the sun's rays. Like DHI data, getting measured DNI data is also difficult and is only available from meteorological institutes and private companies.

If any two of the above three components are available, then the third one can be easily derived using the relation given by equation 2.1, where θ_z is the solar zenith angle.

$$GHI = DNI \times \cos(\theta_z) + DHI \tag{2.1}$$

Table 2.1: List of decomposition models studied in this chapter.

Model	Input variables (to compute k_d)	Abbreviation
Orgill and Hollands[10]	k_t	OH
Erbs [11]	k_t	Er
Reindl 1 [12]	k_t	Re-1
Reindl 2 [12]	k_t, α_s	Re-2
Reindl 3 [12]	$k_t, \alpha_s, T_{amb}, RH$	Re-3
DISC [13]	k_t, α_s	DISC
Dutch-I	k_{tm}, α_s	Dutch-I
Dutch-II	k_{tm}, α_s	Dutch-II

2.2. Decomposition models

Decomposition models are used to decompose GHI into DHI and DNI. In this study, five different decomposition models have been evaluated (refer table 2.1) and their performance is compared with the two newly derived models.

2.2.1. Existing models

One of the first decomposition models was introduced by Liu and Jordan which showed a relationship between daily diffuse and global horizontal irradiance [31]. The work of Liu and Jordan was further developed to predict hourly diffuse fraction, k_d (refer eqn. 2.2), as a function of clearness index, k_t (refer eqn. 2.3) [10, 11].

$$k_d = \frac{DHI}{GHI} \tag{2.2}$$

$$k_t = \frac{GHI}{E_a} \tag{2.3}$$

where, E_a is the extraterrestrial irradiance given by eqn. 2.4, which incorporates the effect of elliptical nature of the earth's orbit on E_a.

$$E_a = E_{sc} \times (R_0/R)^2 \times \cos(\theta_z) \tag{2.4}$$

and
E_{sc} = solar constant ($1367 \ Wm^{-2}$)
R_0 = mean Earth-Sun distance ($149,598 \ km$)
R = Earth-Sun distance at the time of interest

Other authors developed diffuse fraction correlations dependent on factors like solar elevation, temperature, etc. in addition to k_t while some authors used modified clearness index by using a "clear sky" radiation instead of extraterrestrial irradiation [12, 13, 32, 33].
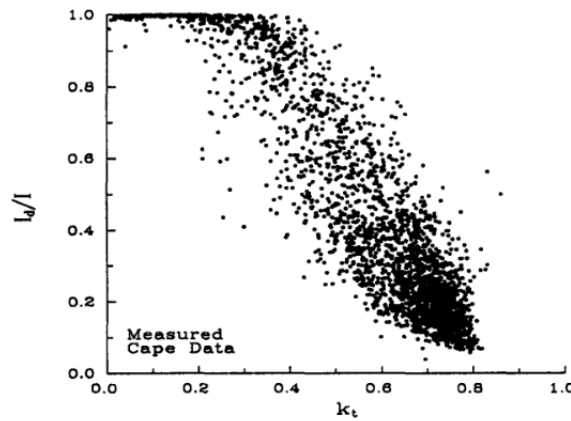
Figure 2.2: Measured diffuse fraction vs. clearness index for Cape Canaveral, FL, USA [12].

Figure 2.2 shows a sample scatter plot of k_t vs. k_d as used by Reindl et al. The main advantage of models based on k_t (referred as Liu-Jordan models) is that they require GHI and other readily available measured data to predict diffuse and direct component.

It is important to note that these decomposition models were initially developed using hourly irradiance data, but in this study, their performance is being evaluated for data available per minute. The

models were selected based on their reported performance in literature and availability of required measured data for model comparison [12, 34]. Detailed explanations of the decomposition models used in this study can be found in Appendix-I.

2.2.2. Development of new diffuse fraction correlations

The primary motivation behind developing new diffuse fraction correlations is to improve the prediction of decomposition models specifically for the Netherlands. The two new correlations are based on the Liu-Jordan models and will be referred to as "Dutch-I" and "Dutch-II". Both the correlations are dependent on clearness index and solar zenith angle. The first one (Dutch-I) is a set of linear correlations whereas the second one (Dutch-II) has quadratic correlations. The choice of predictors was based on the performance of the previously developed Liu-Jordan models and a comparison of performance of these models for the Netherlands (Refer section results 2.3.3)[12].

Three significant changes were adopted while developing the new models to improve their performance. First, the clearness index, k_t, has been modified to account for fluctuations in irradiance due to passing clouds based on the work of Woyte et al. and is denoted by k_{tm} as given by eqn. 2.5 [35].

$$k_{tm} = \frac{GHI}{E_a(\sin\delta\sin\lambda + \cos\delta\cos\lambda\cos(h))} \quad (2.5)$$

Where δ is the earth's declination angle, λ is the latitude of a certain location on the earth and h is the hour angle which expresses the time passed from the solar noon in degrees.
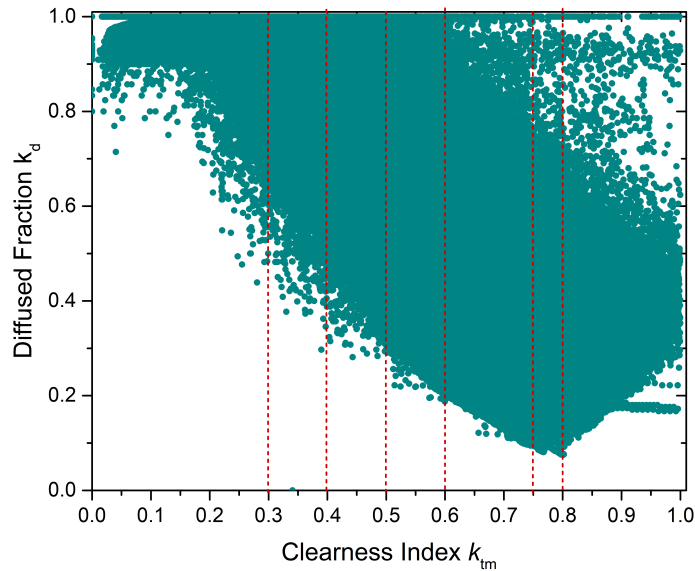
Figure 2.3: Ranges of k_{tm} used for Dutch-I and Dutch-II (based on Cabauw data,2016).

Secondly, irradiance data per minute is used to derive the correlations as compared to hourly or daily average irradiance data used in literature. The data was obtained from Cabauw Experimental Site for Atmospheric Research (CESAR), NL (refer section 2.3.1 for more details). The dataset was divided into seven distinct intervals (see fig. 2.3) based on the clearness index as compared to three in traditional models. It was divided into more intervals because in the range of $0.3 < k_{tm} \leq 0.8$, the number of data points are very high and dividing it into more intervals helps in getting a better fit. The ranges of the intervals were obtained by comparing results of multiple regression analysis.

The final version of correlations Dutch-I (linear) and Dutch-II (quadratic), are given below, where the values of coefficients are shown in Table 2.2 and 2.3 respectively.

Dutch -I

$$k_d = c_1 + c_2 k_{tm} + c_3 \cos(\theta_z) \tag{2.6}$$

Dutch-II

$$k_d = f_1 + f_2 k_{tm} + f_3 \cos(\theta_z) + f_4 k_{tm} \cos(\theta_z) + f_5 k_{tm}^2 + f_6 \cos(\theta_z)^2 \tag{2.7}$$

Table 2.2: Coefficients of decomposition model : Dutch-I

Range of clearness index	c_1	c_2	c_3
$0 \le k_{tm} \le 0.3$	0.99	-0.09	0.01
$0.3 \le k_{tm} \le 0.4$	1.14	-0.67	0.07
$0.4 \le k_{tm} \le 0.5$	1.54	-1.79	0.18
$0.5 \le k_{tm} \le 0.6$	1.65	-2.04	0.23
$0.6 \le k_{tm} \le 0.75$	1.49	-1.76	0.12
$0.75 \le k_{tm} \le 0.8$	-0.17	0.81	-0.32
$k_{tm} \ge 0.8$	0.00	0.69	-0.35

Table 2.3: Coefficients of decomposition model : Dutch-II

Range of clearness index	f_1	f_2	f_3	f_4	f_5	f_6
$0 \le k_{tm} \le 0.3$	1.00	-0.02	-0.02	0.08	-0.06	-0.01
$0.3 \le k_{tm} \le 0.4$	0.93	0.37	0.05	-0.08	-0.61	-0.04
$0.4 \le k_{tm} \le 0.5$	1.36	-0.16	-0.53	1.96	-2.76	-0.17
$0.5 \le k_{tm} \le 0.6$	2.36	-4.63	0.07	-0.69	2.56	0.67
$0.6 \le k_{tm} \le 0.75$	2.75	-7.75	3.03	-6.20	6.60	1.41
$0.75 \le k_{tm} \le 0.8$	12.57	-31.99	-0.65	-1.45	21.68	1.25
$k_{tm} \ge 0.8$	-2.45	6.97	-1.81	0.76	-3.79	0.73

Once diffuse fraction (k_d) is determined from the piecewise correlations, the DHI and DNI are obtained using eqns. 2.8 and 2.9

$$DHI = k_d \times GHI \tag{2.8}$$

$$DNI = \frac{GHI - DHI}{\cos(\theta_z)} \tag{2.9}$$

2.3. Model comparison

2.3.1. Data description

As the aim of this thesis is to improve energy yield prediction of a PV system in the Netherlands, all the analysis and estimations are done using solar irradiance data from the Netherlands. The main source of measured irradiance, as well as other weather data, is from the Cabauw Experimental Site for Atmospheric Research (CESAR) (see fig. 2.4) which is maintained by the Dutch meteorological institute - Koninklijk Nederlands Meteorologisch Instituut (KNMI). This dataset will be referred to

as "Cabauw data" in the rest of the thesis. KNMI also has other weather stations located across the Netherlands, but the one at Cabauw is a part of the Baseline Surface Radiation Network (BSRN) and provides very high-quality radiation measurements for climate research [36].

Figure 2.4: Map of KNMI meteorological stations in the Netherlands [36].

Data resolution

The weather data (irradiance, wind speed and temperature) obtained from Cabauw has a resolution of one minute. This temporal resolution has been used for all the analyses in this project unless specified. This resolution was important to study the effect of rapid fluctuations in irradiance on the performance of different modeling steps.

Time span

For this study, data from the period of 2014-2016 was used depending upon the requirement of the analysis.

Data check

The performance of any empirically derived relation depends on the quantity as well as the quality of the data. As the input data consist of minute data for one year, it is assumed that the quantity of data is sufficient but to ensure the quality of data, various data checks were performed based on the methods used in literature for decomposition models [12, 18, 34]. Firstly, data which violated physical limits were removed from the analysis: GHI, DHI and DNI values less than 0 W/m^2 or greater than 1300 W/m^2. Similarly, as DHI cannot exceed GHI, measurements of DHI which exceeded the corresponding GHI measurement were set equal to the GHI. Secondly, measurements which would produce spurious data points based on the combinations of diffuse fraction and clearness index were removed [11, 12]. To remove such measurements following two cases were used.

$$Case\,1: \frac{DHI}{GHI} < 0.90 \, and \, k_{tm} < 0.20$$

$$Case\,2: \frac{DHI}{GHI} > 0.80 \, and \, k_{tm} > 0.60$$

Case 1 eliminates spurious measurements by limiting the diffuse fraction under cloudy overcast conditions as it is reasonable to have a higher amount of scattered radiation due to cloud cover. Similarly, *Case* 2 is used to remove measurements which will give unreasonable diffuse fraction under clear sky

conditions. Thirdly, values corresponding to GHI measurements under 1 W m−2 and solar elevation of 1° were removed as the sensors perform less accurately in these ranges[34]. Once all the data checks were performed, the final data set consisted of 255,786 measured values which were used for this study. Table 2.4 summarizes the main information about the datasets used in this chapter.

Table 2.4: Summary of database used in this chapter

Database name	Source	Period	Variables used	Purpose
Cabauw data	CESAR, Nl	2016	$GHI, DNI,$ DHI	To derive the two new decomposition models (Dutch-I & Dutch-II)
Cabauw data	CESAR, Nl	2014, 2015	$GHI, DNI,$ DHI	To evaluate the performance of the two new decomposition models

2.3.2. Statistical parameters

To compare the performance of the models, four statistical indicators namely Mean Bias Difference (MBD), percentage Relative Difference (%RD), Root Mean Square Difference (RMSD) and Composite Residual Sum Squares (CRSS) as given by eqns. 2.10, 2.11, 2.12 and 2.13.

$$MBD = \frac{\sum_{i=1}^{n} \left(M_{(i)} - C_{(i)} \right)}{n} \tag{2.10}$$

$$RD_i = \frac{M_{(i)} - C_{(i)}}{M_{(i)}} \times 100 \ (\%) \tag{2.11}$$

$$RMSD = \sqrt{\frac{\sum_{i=1}^{n} \left[(M_{(i)} - C_{(i)})/M_{(i)} \right]^2}{n}} \tag{2.12}$$

where,

$M_{(i)}$ is the measured quantity and $C_{(i)}$ is the calculated quantity from the models and n is the total number of values in the dataset. While comparing irradiance prediction, MBD and RMSD will have the units of W/m^2.

$$CRSS = \sum_{i=1}^{n} \left[\frac{DHI_{c(i)}}{GHI} - \frac{DHI_{m(i)}}{GHI} \right]^2 \tag{2.13}$$

$DHI_{m(i)}$ denotes the measured diffuse horizontal irradiance, $DHI_{c(i)}$ is the computed diffuse irradiance.

Mean bias difference is an indicator of long-term performance of the model whereas the root mean square difference gives information regarding the short-term performance of a model. However, these two errors by themselves are not sufficient to draw a conclusion about the best model. For instance, a few large differences between modeled and measured values can lead to a significant increase in RMSD while the value of MBD might be small because the model has equally overestimated and underestimated the values. Therefore, apart from MBD and RMSD, the models are also evaluated based on CRSS and %RD. CRSS is an absolute number indicating the sum of the relative difference between the measured and the modeled value. For a given number of samples, a lower value of CRSS shows that the models have the least accumulated error [12].

2.3.3. Evaluation of decomposition models

In this section, the performance of the two newly derived decomposition models (Dutch-I and Dutch-II) for the Netherlands has been discussed. Their performance is compared with seven other most widely used decomposition models namely Orgill and Hollands (OH), Erbs (Er), three models by Reindl et al.(Re-1, Re-2 and Re-3) and Maxwell's quasi-physical model (DISC) for the year 2016 [10–13]. Further, to validate the results using data other than that used to derive the relations, the models were compared using irradiance data from Cabauw for the years 2014 and 2015.
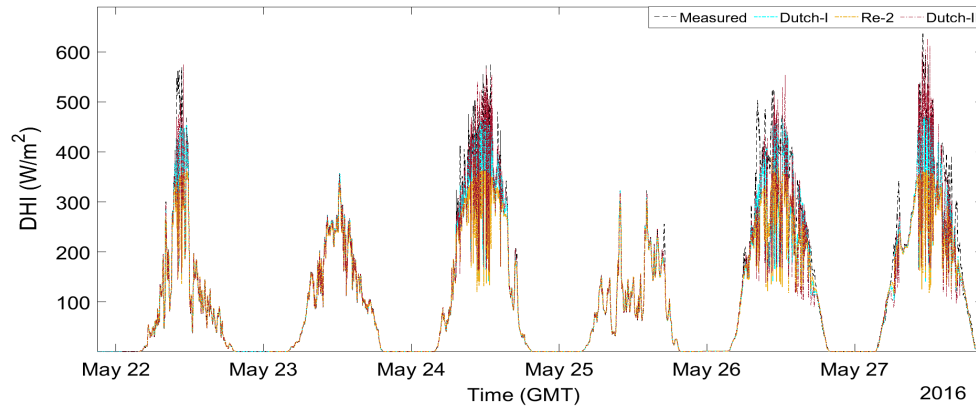
Figure 2.5: Measured and modeled diffuse horizontal irradiance for one week in May 2016 (based on Cabauw data).

Figure 2.5 shows the comparison of measured diffuse irradiance with the predicted values from the new models and Re-2 (representative of other existing models) for one week in May 2016. Clearness index values (k_{tm}) used for Dutch-I and Dutch-II models are referred to as k_t for simplicity. It can be seen that the Re-2 model underestimates the diffuse irradiance for higher values of irradiance and Dutch-II gives a better prediction in those regions.

(a) Spring days   (b) Summer days
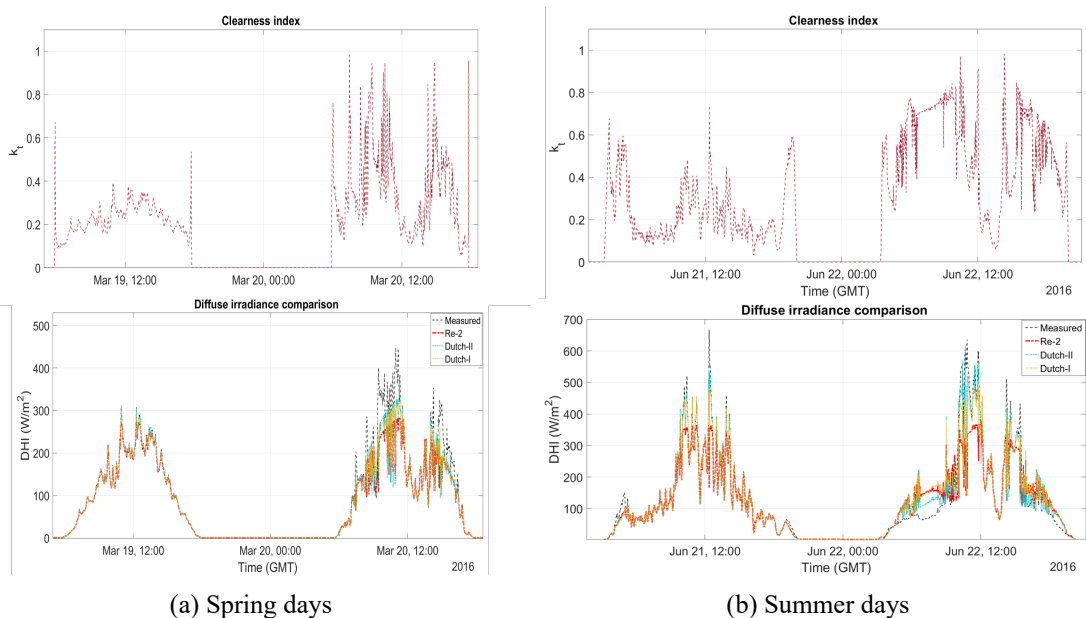
Figure 2.6: Comparison of clearness index and DHI for four days in 2016 based on Cabauw data.

To observe the difference in prediction by these three models in more detail, results for two days in March 2016 (Spring days) and June-16 (Summer days) are shown in figure 2.6a and 2.6b respectively.

The top figure shows the plot of clearness index whereas the bottom one compares the modeled and measured diffuse irradiance. From the figures, it can be observed that for clearness index less than 0.4 all the models predict the diffuse component accurately but when it is higher than 0.4, the two new models give a much better prediction, especially for values of $k_t > 0.6$. For instance, observing modeled diffuse irradiance on 22nd June (figure 2.6b), it can be seen that, when k_t values are greater than 0.6, Re-2 is underestimating the irradiance by more than 200 W/m^2 whereas the Dutch-II is almost overlapping measured values. Another important observation is that the performance of all models is poor when the values of k_t are fluctuating a lot and are in the range of 0.4 to 0.6, which represents days with moving clouds. This can be explained by the fact that the spread of k_d with respect to k_t (refer fig 2.3) is too high in the range of 0.4< k_t <0.6.
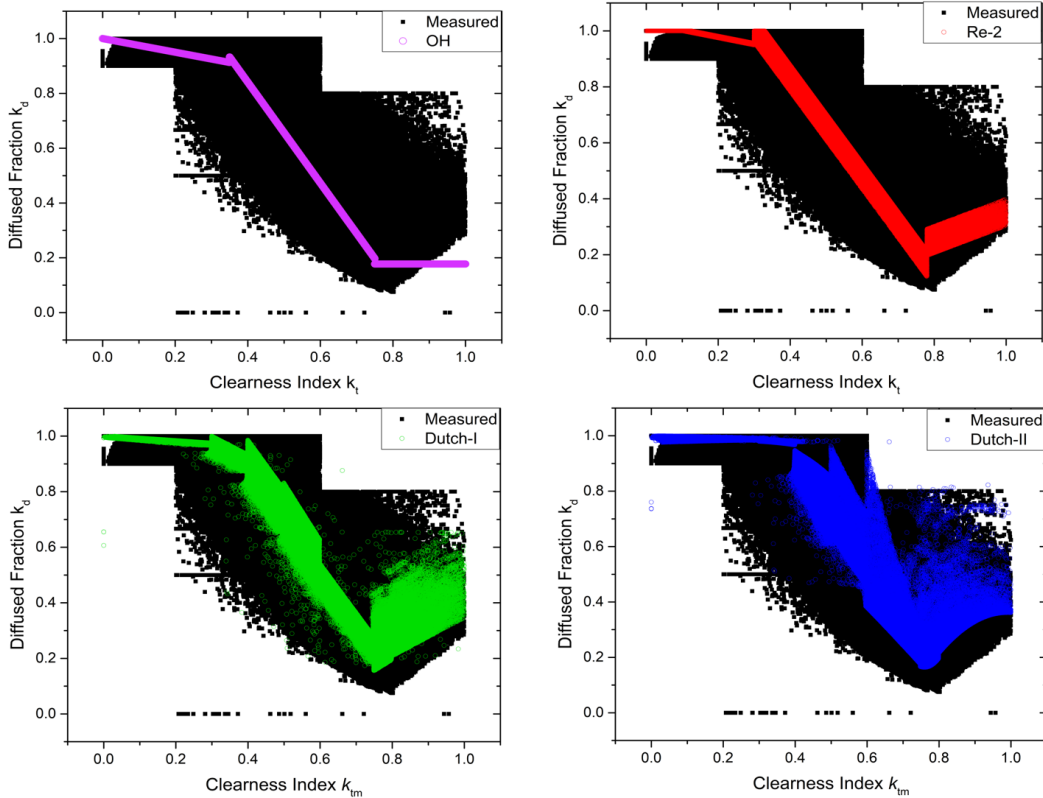
Figure 2.7: Comparison of scatter plots for decomposition models (based on Cabauw data 2015).

Figure 2.7 shows the scatter plot between clearness index and diffuse fraction. The measured values (after filtering the data for spurious measurements) are shown in black and the values predicted by OH, Re-2, Dutch-I and Dutch-II in colour. An ideal and 100% accurate model will be able to completely cover the scatter plot of the measured values, showing that it is able to predict the highly variable diffuse fraction for all the values of the clearness index. It can be observed, from fig. 2.7, that since OH uses linear correlations (dependent on k_t), it predicts values that are always on the straight lines and has a very limited coverage. Re-2 covers a larger part of the plot as it a function of k_t and solar zenith angle (θ_z). Even though Dutch-I also has linear correlations based on k_t and θ_z, similar to Re-2, it has a more distributed response which is because of use of more intervals of k_t to derive the correlations. Further, it is derived from climate specific irradiance data (from Cabauw) having per minute temporal resolution which contributes to its improved performance. Dutch-II improves on top of Dutch-I by using quadratic correlations in those ranges. Dutch-II covers the largest fraction of scatter plot. The overall performance of the two new models (Dutch-I and Dutch-II) is better than others as they are able to cover a larger spread of k_d. Certainly, no model is able to completely cover the scatter plot of

measured values because diffuse fraction of irradiance is not just a function of k_t, solar zenith angle or other atmospheric parameters like temperature, humidity, pressure, etc. but is also affected by factors like density of clouds, their shape and position in the sky. There is a need to assess and include the effects of all such parameters if one wants to make decomposition models more accurate.
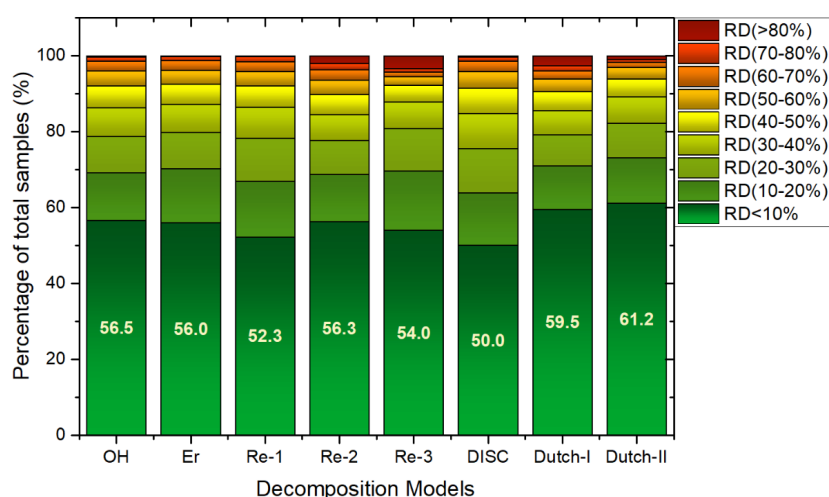
Figure 2.8: Comparison of decomposition models based on cumulative % relative difference (based on Cabauw data 2015). The bottom most box (dark green) in each bar shows % of total samples less than 10% RD whereas the topmost box (red) shows the % of samples having %RD greater than 80%.

To compare the performance of models over a complete year, RMSD, MBD, CRSS and cumulative %RD were computed. Figure 2.8 shows the comparison of cumulative %RD for all the eight models. The bar chart compares the percentage of the total number of samples which are in different ranges of % relative difference (Cabauw data 2015). The bottom most box (dark green) in each bar shows % of total samples with less than 10% RD (indicated by number) whereas the topmost box (red) shows the % of samples having %RD greater than 80%. For example in fig. 2.8, 56.01 % of total values predicted by the Erbs model have a %RD less than 10%. A model performs the best if it has the highest percentage of samples in the bottom most box and least percentage of samples in the topmost box of the bar graph. Thus, amongst the existing decomposition models, OH has the highest percentage of samples (56.5%) with a %RD less than 10% followed by Reindl-2 (56.3%). Dutch-I and Dutch-II improve the prediction of DHI from GHI as they have 3% and 4.7% more samples (%RD < 10%) as compared to OH respectively. The increase in % of samples is significant as the total number of samples were more than 200,000. Table B.1, summarizes this information numerically for the year 2014 and 2016, which also shows similar improvement in the results.

Comparison based on RMSD (see fig. 2.9a) indicates that Dutch-I and Dutch-II consistently have the lowest values for all the three years. Similarly, figure 2.9b compares the composite residual sum squares which also shows that the two new models have the least accumulated error. Based on the results of %RD, RMSD and CRSS, it can be said that the newly developed models can predict more accurate values of DHI from GHI as compared to the existing models. Detailed results of RMSD, MBD and CRSS for all the decomposition models for the three different years (2014-16) are available in Appendix B (table B.2).

(a) Root mean square difference

(b) Composite residual sum squares.
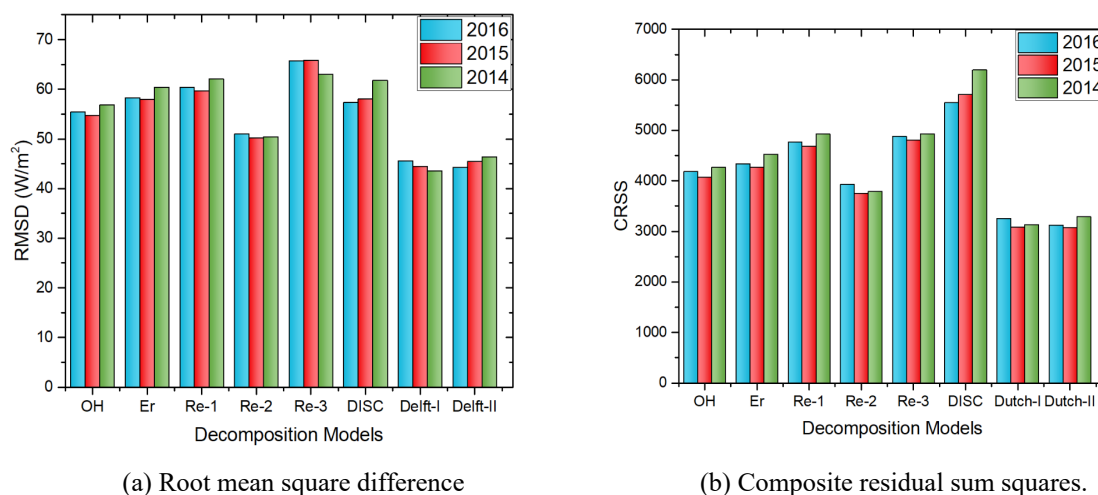
Figure 2.9: Comparison of models performance based on RMSD and CRSS for 3 years of Cabauw data

2.4. Conclusions

Decomposition models play a significant role in design and monitoring of a PV system as they are required to derive diffuse irradiance from widely available global horizontal irradiance.

In this chapter, the following research questions were addressed:

Which is the most accurate decomposition model ?

It was found that amongst the existing decomposition models, RE-2 and OH perform the best for the climatic conditions of the Netherlands. These results agree with previous studies in the literature [32].

What are the drawbacks of existing decomposition models and how they can be improved?

The best performing existing models are developed using hourly irradiance data and thus they ignore the fluctuating nature of solar radiation. Nowadays, irradiance data having a temporal resolution as low as a minute is available and it should be used to update the coefficients of existing models. Also, the number of piecewise correlations used to fit the irradiance data is limited to three in the existing models but, to better cover the highly scattered distribution of diffuse fraction with clearness index, the number of correlations should be increased.

Is it possible to improve the performance of decomposition models using local irradiance data?

To improve the performance of the models, specifically for the Netherlands, two new decomposition models, namely Dutch-I and Dutch-II, were developed using minute data for one year (2016). The performance of the newly developed models was then validated with existing models using weather data for two different years 2014 and 2015 obtained from the same database (Cabauw). It showed that the two new models (Dutch-I and Dutch-II) reproduce measurement results more accurately. For the year 2015, results derived using these models had an RMSD in the order of 44 W/m^2 and CRSS of around 3075. For the same year, the number of total samples having %RD less than 10% increased by 4.7% and 3%

when using Dutch-II and Dutch-I respectively as compared to the best performing existing model (OH).

It was also observed that, in general, all the models were able to predict diffuse irradiances accurately during fully cloudy days ($k_t < 0.4$) and prediction error was the highest on partially clouded days ($0.3 < k_t < 0.6$). The improved performance of the two new models is mainly because of use of k_{tm} instead of k_t, the number of intervals of clearness index to define piecewise correlations and use of minutely irradiance data obtained locally from Cabauw, Netherlands. Thus, it can be concluded that the performance of existing models is dependent on local weather conditions and can be significantly improved by using location-specific irradiance data to derive the coefficients of the piecewise correlations.

3

Irradiance modeling II : Transposition models

Accurate Plane Of Array (POA) irradiance modeling is crucial to designing and monitoring a PV system. Depending upon the location of a PV system, often PV modules are titled to optimize the irradiance received by them. To estimate the irradiance on the tilted plane, one should evaluate beam, diffuse and ground reflected components from global and diffuse horizontal irradiance. In the past, several models have been developed to derive these components, referred to as "transposition models" as they transpose the irradiance data on the horizontal plane to the plane of array of the modules. In the case that the modules are located at a place surrounded by buildings or other objects; transposition models are not enough to accurately predict the irradiance received by the modules and shading analysis becomes essential.

In this context, as mentioned in chapter 1, the following research questions are addressed :

Evaluate and optimize transposition models to compute the irradiance on the plane of array of the e-bike station

- Which are the most accurate transposition models to be used in an urban location?
- How can the performance of existing models be improved by using location-specific parameters like sky view factor and albedo?
- How important is shading analysis to irradiance modeling and what is the most reliable technique to incorporate it?
- What is the effect of using decomposition models instead of measured diffuse and direct irradiance?

In this chapter, performance of the five most commonly used transposition models: Isotropic, Hay/Davies, Reindl, Sandia and Perez is evaluated for the location of the e-bike station. Techniques like shading analysis and use of location specific factors to improve their prediction are discussed. Additionally, a new transposition model, based on ray tracing simulations, is discussed and its performance is compared with the traditional models. Finally, the effect of using decomposition models on the performance of transposition models when only GHI data is available is also evaluated in this study.

3.1. Introduction

To optimize the energy received by the panels throughout the year, the angle between the PV installations and the sun needs to be tuned. Maximum energy is produced by a module when it is always perpendicular to the sunlight. It can be achieved by using a two-axis solar tracker, but due to financial and design constraints, they cannot be utilized for all types of PV system installations. In such

cases, modules are installed at a fixed tilt angle to capture the maximum energy as in the case of e-bike charging station. An important step in designing and monitoring such fixed tilt systems is irradiance modeling at the plane of array and it will be discussed in briefly in this section.

3.1.1. Geographic location

The e-bike charging station is installed on the campus of the Delft University of Technology (52° North; 4.36° East) as shown in figure 3.1. It faces the southwest direction, i.e., an azimuth of 204° w.r.t to North and has an angular tilt of 51° w.r.t to the horizontal plane. The choice of azimuth and tilt was to optimize the energy production during the winter months [1]. In front of the e-bike station, there is a tall building, the faculty of Electrical Engineering, Mathematics and Computer Science (EEMCS) and it casts a shadow on the e-bike station for a significant duration of the day. Apart from that, on the east of the bike station, the faculty of Civil Engineering and Geosciences (CEG) blocks the sun radiation during early hours of the morning.

Figure 3.1: Google earth image of the location of the e-bike station and nearby buildings.

3.1.2. Irradiance modeling on a tilted plane

The total irradiance received by an inclined plane (G_{POA}) consists of three main components, given by eqn. 3.1. Figure 3.2 shows the three main components of G_{POA}.

$$G_{POA} = G_{dir} + G_{ground} + G_{dif} \tag{3.1}$$

where, G_{dir} is the direct beam component. G_{ground} refers to the irradiance received by the modules after being reflected from the ground. In case the modules are surrounded by other objects like buildings, trees, etc., the light reflected from them will also be accounted for in this component. G_{dif} is the diffuse component received by the modules and is a fraction of the total diffuse horizontal irradiance. It is also referred to as the sky diffuse component.
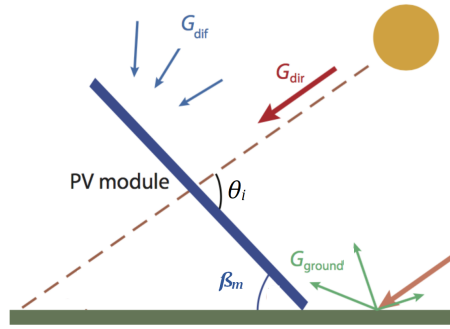
Figure 3.2: Components of solar irradiance received by a tilted plane [19].

Direct beam component

The direct beam component, G_{dir}, depends on the angle of incidence (θ_i) and DNI. It is usually calculated using the eqn. 3.2 . The accuracy of prediction of G_{dir} depends upon the accuracy of available DNI data for the location.

$$G_{dir} = DNI \times cos(\theta_i) \tag{3.2}$$

Ground Reflected component

The ground-reflected component, G_{ground}, depends upon the reflectivity of ground, nearby surroundings, and tilt of the modules. It becomes significant when modules are surrounded by highly reflecting objects like glass covered buildings, snow, etc. Accurate modeling of G_{ground} requires knowledge of albedo which is defined as the ratio of ground reflected irradiance and the global horizontal irradiance. In general, G_{ground} is modeled using eqn. 3.3 which considers the effect of tilt of the module (β_m) and uses a fixed value of albedo (ρ).

$$G_{ground} = GHI \times \rho \times \frac{1 - cos(\beta_m)}{2} \tag{3.3}$$

Equation 3.3 can also be written in terms of the Sky View Factor (SVF) of the tilted module, as given by eqn. 3.4. The SVF is the fraction of the sky as seen by a titled surface. It is a function of tilt of the module and is given by eqn. 3.5. Location specific SVF and albedo are discussed in more detail in section 3.2.2

$$G_{ground} = GHI \times \rho \times (1 - SVF) \tag{3.4}$$

$$SVF = \frac{1 + cos(\beta_m)}{2} \tag{3.5}$$

Diffuse Irradiance

The most complicated part of modeling G_{POA} on a tilted surface is modeling the diffuse irradiance(G_{dif}) received by the tilted modules since, at any moment, the diffuse irradiance is dependent on the state of the sky like the presence of clouds, their movement and several other factors which are difficult to predict [15].
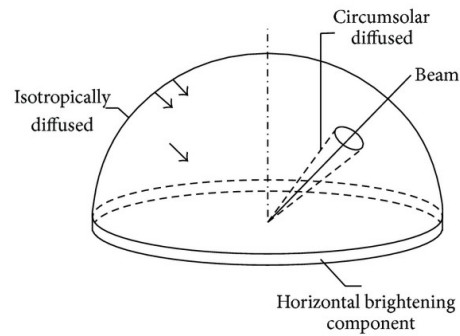
Figure 3.3: Components of diffuse irradiance.

Several models have been developed in the past to calculate G_{dif} and have different degrees of complexity. The main difference is in the way they model the three sub-components of diffuse radiation: circumsolar, horizon brightening, and isotropic diffuse radiation. Circumsolar radiation is due to forward scattering of radiation concentrated in the solar disk. Horizon brightening represents the increased diffuse radiation when the sun is near the horizon. It is caused by the increased path length of the sunlight which leads to more scattering and internal reflections by the earth's atmosphere. The isotropic diffuse component is the radiation uniformly diffused over the sky dome.

3.2. Standard transposition models

Since irradiance measurements are mostly available for the horizontal plane, transposition models are used to transpose them from the horizontal plane to the plane of the modules. These models mostly differ in the way they calculate the sky diffuse component. In this chapter, five standard transposition models (also referred to as sky diffuse models) are evaluated. The models are briefly described in Appendix A. Table 3.1 summarizes the main characteristics of the transposition models used. It can be observed that the isotropic model does not account for the circumsolar or horizon brightening component of diffuse irradiance. The Sandia model uses empirical relation for the horizon brightening and circumsolar beam components of diffuse irradiance and is optimized for Albuquerque, New Mexico. The only difference between Hay/Davies and Reindl is that Reindl has an additional term for calculating horizon brightening component which becomes dominant only during sunset and sunrise. All of these models compute the direct beam and ground-reflected component using eqns. 3.2 and 3.3. Also, all the models assume a constant albedo of 0.2 except for the Sandia model which uses a sun elevation dependent value (eqn. A.35).

Table 3.1: Comparison of Transposition models. While comparing complexity of the models, 5 stars represent the highest level of complexity.

Model name	Characteristics	Complexity
Isotropic (Iso) [37]	Isotropic component only	★
Hay and Davies (H/D) [14]	Isotropic and circum-solar	★ ★
Sandia (Sa) [38]	All, but circum-solar and horizon-brightening components are modeled empirically	★ ★
Reindl 1990 (Reindl) [15]	All	★ ★ ★
Perez (Pz) [16, 17]	All, highly complex in nature	★ ★ ★ ★

A major disadvantage of these models is that they assume that the modules are located in a shade free environment and have an unobstructed horizon. It means that the shading effect due to nearby objects like buildings, trees etc. has to be modeled separately. Also, the performance of these models can be further improved by using location-specific SVF and albedo instead of using standard values.

3.2.1. Shading analysis

An important part of irradiance modelling is shading analysis, especially, if the modules are located in an urban environment. During the design phase, it helps to figure out the position of panels where it will be least shaded and during monitoring it helps to account for the decrease in power. There can be different sources of shade at different times of the day and can be classified as static (nearby objects like buildings) and dynamic (moving clouds) sources of shading. For instance, in figure 3.1 it can be seen that on the e-bike station, the primary sources of shadows are the EEMCS building during noon and nearby trees during the evening. Figure 3.4 shows the effect of shading on the PV power output, for 19th January due to moving clouds(region marked by A), EEMCS building (marked by B) and trees (marked by C).
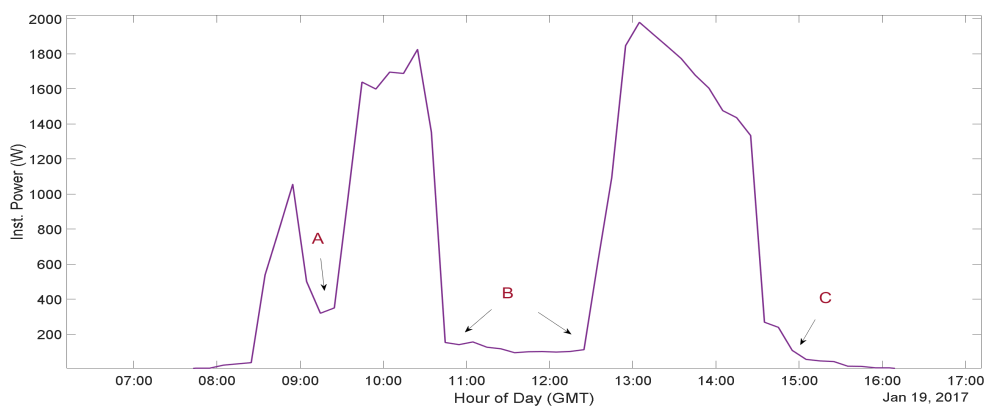
Figure 3.4: Power output of the e-bike station for June 19,2017.

Scope of Shading Analysis

In this thesis, it is assumed that solar modules mounted on the e-bike station are always shaded homogeneously and the performance of modules decreases almost proportionately to the reduction in irradiance [39]. Effect of partial shading is not taken into consideration due to the complexity involved in modeling it and time constraint. Further, shading analysis is performed only for static objects and it is assumed that it mainly affects the direct beam and the ground-reflected component. Shading due to clouds is considered to be taken care of by the irradiance measurements, but it should be noted that it is highly dependent on the size, shape and trajectory of clouds. For instance, it is possible that a cloud casting a shadow on the e-bike station might not be shading the measurement sensors in Cabauw. Hence, shading due to clouds could cause a huge difference between irradiance predicted and measured on the e-bike station.

Shading analysis tools

Different analysis techniques exist to model the effect of shading due to static objects on the modules. In this thesis, two most widely used techniques will be evaluated.

Meteonorm-Horicatcher

Horicatcher, also known as a fisheye camera, consists of a digital camera mounted above a highly reflective bell-shaped horizon mirror as shown in figure 3.5b. The complete setup is kept in front of the

modules or desired location (fig 3.5a) and an image of the reflection in the horizon mirror is taken. This image is further processed, using an associated software of Meteonorm called as "Horizon", to generate a file having hourly shading factor for the location [40]. Figure 3.6 shows the processed image generated by Horizon having the shaded region superimposed over the sun path[1] diagram for the location.

(a) Horicatcher setup in front of the e-bike station .

(b) Image taken by the fish eye camera.

Figure 3.5: Horicatcher setup.
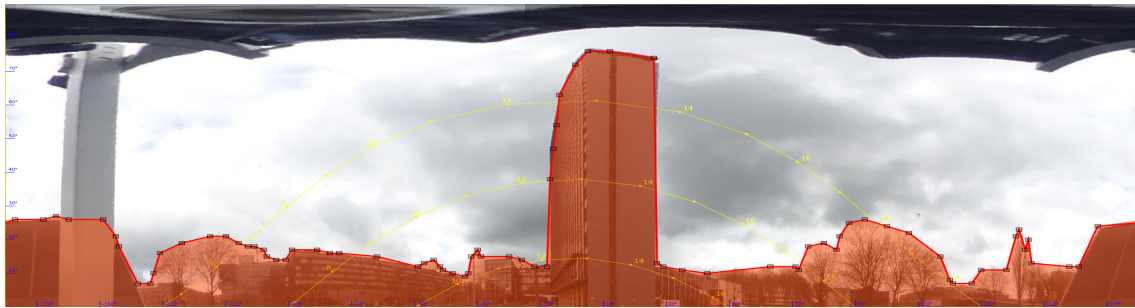
Figure 3.6: Processed Horicatcher image using Horizon/Meteonorm.

The Shading Factor (SF) is calculated by the software using eqn. 3.6 where the irradiance data for the site is obtained from its repository.

$$Shading\ Factor(SF) = \frac{DNI\ with\ horizon}{DNI\ without\ horizon} \tag{3.6}$$

The irradiance data available in Meteonorm is representative of the data for a location and has temporal resolution of one hour [41]. It means that the shading factor calculated by Meteonorm also has an hourly time step and it ignores any shading that occurs in between the time steps, leading to significant errors in the shading analysis.

Another source of error is that for a particular day, real-time weather conditions (such as a clear or overcast day) may be very different from the conditions recorded in the Meteonorm database. For instance, it is possible that a day which is a completely overcast day according to its database might be a clear sky day in reality and therefore no shading for such a day will be predicted.

3D modeling using Sketchup

Another widely used method to model and simulate the effect of location specific shading is using a 3-D modeling software. Amongst the various available 3-D modeling software, Sketchup by Trimble,

---

[1]Sun path diagrams represent the annual changes in the path of the sun through the sky

USA was chosen because of its user-friendly nature and wide support of plugins to analyze the effect of shading[42]. Another advantage of Sketchup is that it comes with an inbuilt sun path algorithm and objects can be geolocated using Google maps which makes the shadows realistic.

First, the e-bike station was modeled and geolocated on the campus of TU, Delft (see fig 3.7). It should be noted that only two buildings (EEMCS and CEG) surrounding the e-bike station were modeled whereas nearby trees, poles and other buildings were ignored.
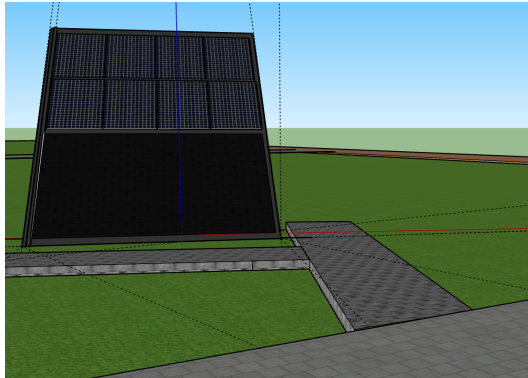
| (a) 3D model e-bike (front side). | (b) 3D model e-bike (Back side). |

Figure 3.7: Sketchup 3D model of e-bike charging station.
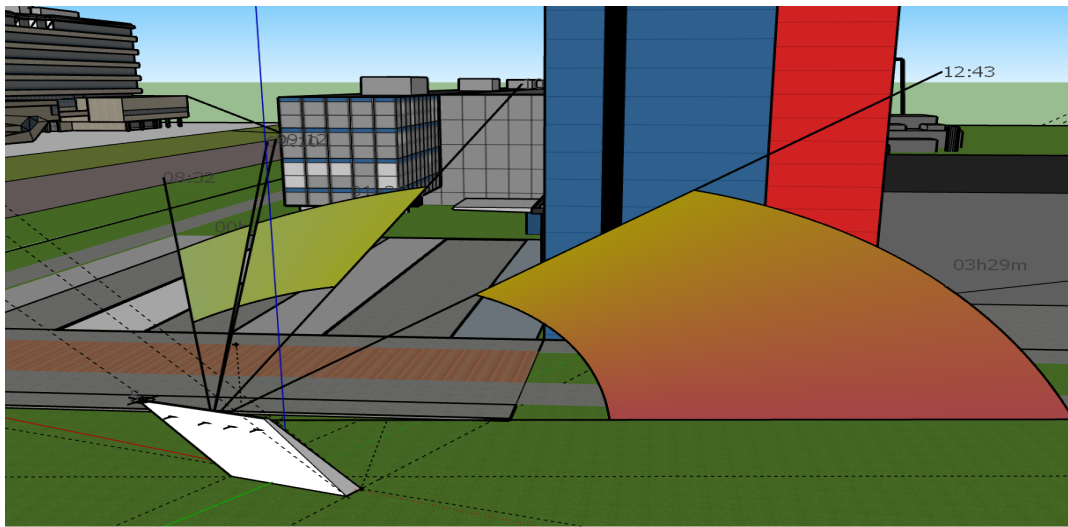
Figure 3.8: Calculation of shading factor using Sketchup for 19-Jan-2017.

Next, the shading analysis was carried out for the complete year of 2017 using a plugin called "LSS Chronolux" which carries out a ray tracing analysis for the test point and give the number of hours the test point was receiving direct sunlight. For instance, fig. 3.8 shows analysis for 19th January 2017 where the high building is blocking the sunlight during the noon hours (between 10:30 A.M – 13:00 P.M.) which matches with the dip in power produced (refer fig. 3.4) on that day. Finally, the data obtained from Sketchup was processed using MATLAB to compute per minute shading factor for the e-bike station. It is important to note that the SF given by Sketchup is binary and only indicates whether the test point was shaded or not. On the other hand, SF given by Horicatcher ranges between 0 and 1.

3.2.2. Location specific SVF and Albedo

Sky View Factor (SVF)

To obtain a more realistic SVF, in this study, 3-D modeling using Sketchup (refer section3.2.1) was used as shown in figure 3.9. It was found that the modules have an SVF of 0.61 as compared to 0.815 (predicted by eqn. 3.5), which is expected as not just the module tilt but also the presence of EEMCS and CEG affect the SVF of the modules. Due to nearby buildings the SVF of e-bike station decreases by almost 20%. In reality, the value of SVF could be even less as the effect due to nearby trees, poles, etc. was not taken into consideration.

(a) Dome showing the actual SVF.   (b) 3D model of e-bike station and its surroundings.
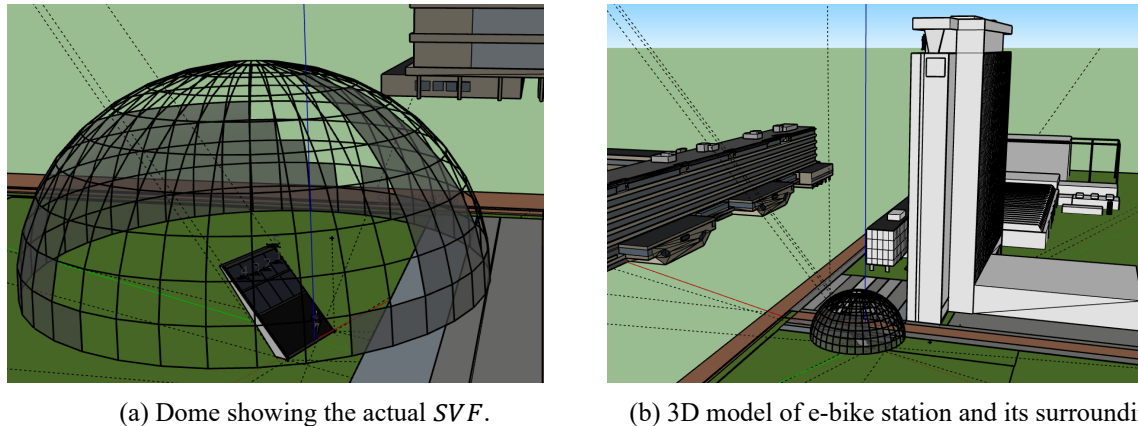
Figure 3.9: Calculation of Sky View Factor (SVF) using Sketchup.

Albedo

Determination of correct values of albedo is crucial to calculating the ground-reflected component of irradiance received by the tilted modules. In general, an albedo of 0.2 is used while modeling G_{POA} received by PV systems in urban locations, but it is always the best practice to obtain location specific albedo [43]. For the location of the e-bike station, the albedo was measured using an albedometer which consists of two pyranometers attached back to back (see fig 3.10). The measurement was performed by fixing the setup at the height of 1.5 m above ground, in such a way that one pyranometer faced upwards (measuring the GHI) and the second one faced towards the ground (measuring the ground reflected components). The values of albedo measured on different surfaces are tabulated in table 3.2. As concrete tiles and grass mostly surround the e-bike station, an average albedo value 0.20 was used for initial simulations.
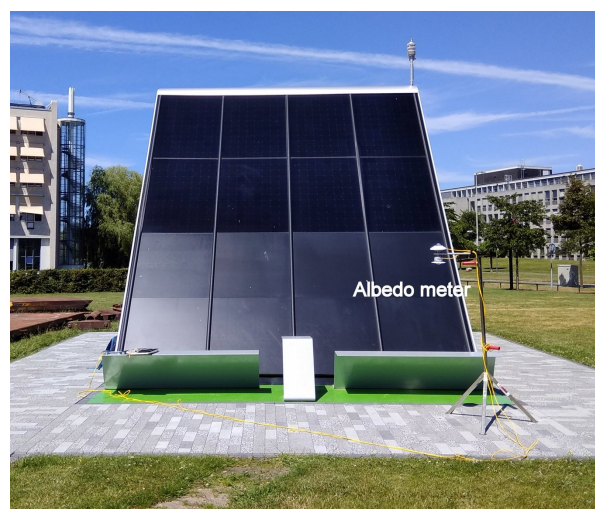
Figure 3.10: Measuring albedo in-front of the e-bike station using an albedometer.

Table 3.2: Average albedo values of materials around the e-bike station

Material		Average Albedo
Concrete blocks		0.16
Small tiles (Footpath)		0.13
E-bike station tiles		0.21
Cycling path		0.12
Grass		0.19

Characteristics of Albedo

It has already been found that using a constant average value of location specific albedo gives satis-
factory results for modeling ground reflected irradiance [43, 44]. To study the variation of albedo on
factors like GHI and position of the sun, albedo values were measured for one complete day in front of
the e-bike station. The obtained albedo values were fitted with values of GHI and sun elevation angle
(refer figure 3.11).
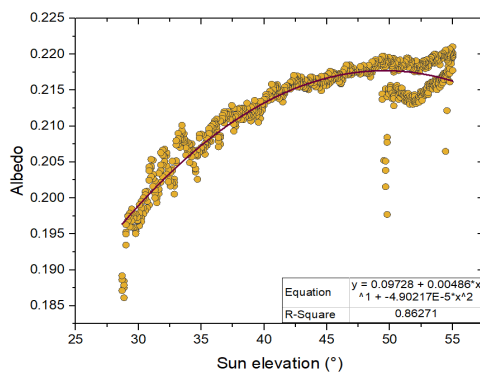
(a) Albedo vs Sun elevation (α_s).
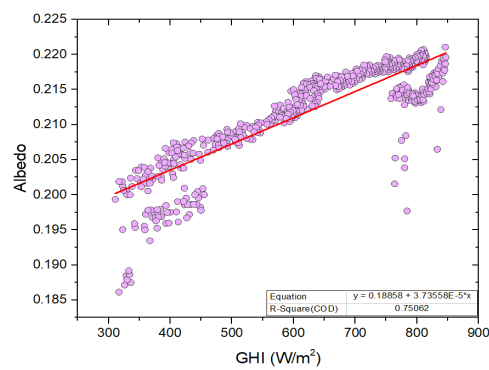
(b) Albedo vs GHI.

Figure 3.11: Dependence of albedo on sun elevation and GHI.

It was found that albedo (ρ) shows a slight dependence on the sun elevation angle (α_s) as expressed

by eqn. 3.7 and it is in line with earlier findings in literature [43, 45].

$$\rho = 0.0972 + 0.0048\alpha_s - 4.9021\alpha_s{}^2 \tag{3.7}$$

The dependence of albedo on GHI was not very clear but it can be inferred from figure 3.11b that albedo is directly proportional to the GHI.

It is certain that albedo strongly depends on the site and its environment. As albedo is key to predicting G_{ground}, there is a need for a more detailed study involving albedo measurements over a longer period to find its dependence on parameters like GHI, α_s, etc.

3.3. Ray tracing model using LightTools

Recently Santbergen et. al. introduced a new method to determine G_{POA} of a PV system. It determines a sensitivity map for the PV system using a ray tracing software and combines it with the sky map obtained from the Perez model [17, 46]. This method will be referred to as the "Ray tracing" method in the rest of the thesis. This method is found to be accurate in determining the irradiance received by systems having a complex geometry.
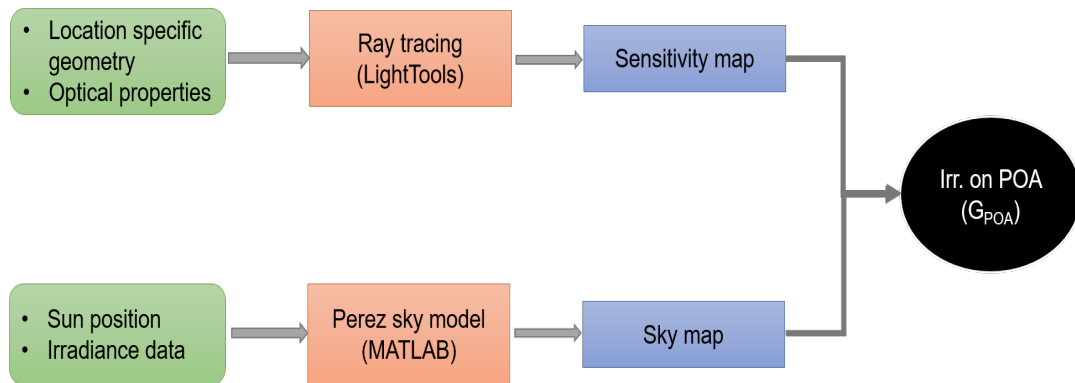
Figure 3.12: Flowchart showing steps involved in determining G_{POA} using ray tracing method.

In this study, ray tracing was performed using an advanced ray tracing software called LightTools (LT). Figure 3.12 shows a simplified flow chart of the steps involved in determining the G_{POA} using the ray tracing method. The method involves use of two models. The first model requires a detailed modeling of the PV system and its surroundings (see fig. 3.13a) in the LightTools. Next, ray tracing simulations are carried out in LightTools and its results are processed to get a so-called sensitivity map for the PV system (see fig. 3.13a). A sensitivity map is simply a representation of the surface's sensitivity to the incident light as a function of hemispherical angle of incidence. The second model uses the Perez model which reconstructs the luminance distribution of the circumsolar and diffuse light across the sky from DHI and DNI values. This is called a sky map. Finally, the output of the two models (Sky map and sensitivity map) are combined to predict the G_{POA} incident on the module. Santbergen et. al. have discussed this irradiance model in detail [17, 46].
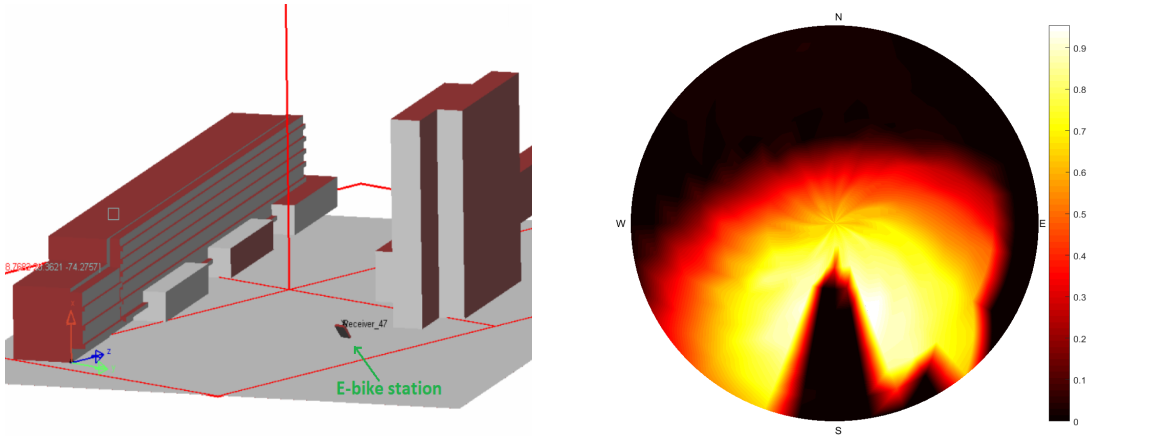
(a) Model of the e-bike station and its surrounding buildings in LightTools.

(b) Sensitivity map of the panels installed on the e-bike station .

Figure 3.13: LightTools model and sensitivity map obtained for the e-bike station.

The main advantage of this method is that it does not require additional shading analysis. Further, it not only includes the ground reflected component but also the reflections from the surfaces of nearby buildings. The only disadvantage is that one requires advanced ray tracing simulation software like LightTools which are very expensive.

3.4. Model comparison

3.4.1. Data description

In addition to the Cabauw data (refer section 2.3.1), in this chapter, data from the e-bike charging station was used, which will be referred to as "e-bike data" in the rest of the thesis.

The e-bike charging station on the campus of TU Delft is installed with a state-of-art weather station (Lufft - WS503-UMB Smart Weather Sensor) which measures various weather parameters as summarized by table 3.3.

Table 3.3: Data measured at the e-bike station.

Data variable	Unit
Irradiance (G_{POA})	W/m^2
Air pressure	Pa
Wind speed	m/s
Ambient temperature	$°C$
Relative humidity	$\%$
DC Power generated	Watts

Data resolution

Data recorded at the e-bike station had a temporal resolution of 10 minutes initially which was then reduced to 1 minute.

Time span

For this study, data from the period of October 2016 to April 2017 was used. The time span was restricted by the availability of Cabauw and e-bike data.

Data Check

To ensure the quality of data used, a rigorous quality check was carried out. In addition to data checks explained in section 2.3.1, it was also ensured that while comparing results based on two or more data sets, only points available in all the datasets were used for analysis. It is important to mention that, as the e-bike station was newly installed (Oct-16) there were some problems with the communication system of the weather sensor, causing loss of several hours of data which has been discussed in Appendix C.

Once all the data checks were performed, the final data set consisted of 56,243 samples which were used for this study. Table 3.4 summarizes the purpose and duration of the datasets used in this chapter.

Table 3.4: Summary of database used in this chapter.

Database name	Source	Period	Variables used	Purpose
Cabauw data	CESAR, Nl	Oct'16-Apr'17	GHI, DNI, DHI	Used as input to transposition models
e-bike data	E-bike station, Delft, Nl	Oct'16-Apr'17	G_{POA}	Comparing output of the transposition models

3.4.2. Evaluation of transposition models

In this section, first, the accuracy of the five standard transposition models is evaluated by comparing the predicted and measured irradiance on the plane of array (G_{POA}) of the e-bike station. The input to the irradiance model is the measured GHI, DHI and DNI from Cabauw data for the period of Oct'16 -Apr'17. An albedo of 0.20 was used while computing the ground-reflected component. Next, the effect of using shading analysis, location specific SVF and albedo values on the performance of models is discussed. It is followed by the evaluation of the new ray tracing method. Finally, a comparison is made between G_{POA} prediction using just transposition models and a combination of transposition and decomposition models. Performance of the models is evaluated using statistical indicators; namely, MBD (W/m^2), %RD and RMSD (W/m^2).

Figure 3.14 shows the plot of modeled and measured G_{POA} at the e-bike station for three days in February 2017. The first two days are clear sky days whereas the third day is partly clouded in the second half of the day. It can be seen that all the models predict irradiance within a close range to the measured one during morning and evening hours. During afternoon, the dip in the measured values is due to shadow of the EEMCS building. The region marked by a circle on the third day shows that all the models underestimate the irradiance as compared to measured data which could be because the sky might be covered with clouds in Cabauw from where input data is obtained. Also, isotropic model predicts lower irradiance than other models as it does not consider the horizon brightening component of the diffuse irradiance.

Shading analysis (Meteonorm-Horicatcher vs Sketchup)

To model shading due to EEMCS and CEG, shading factor using Meteonorm-Horicatcher and Sketchup was calculated and incorporated in the transposition models.
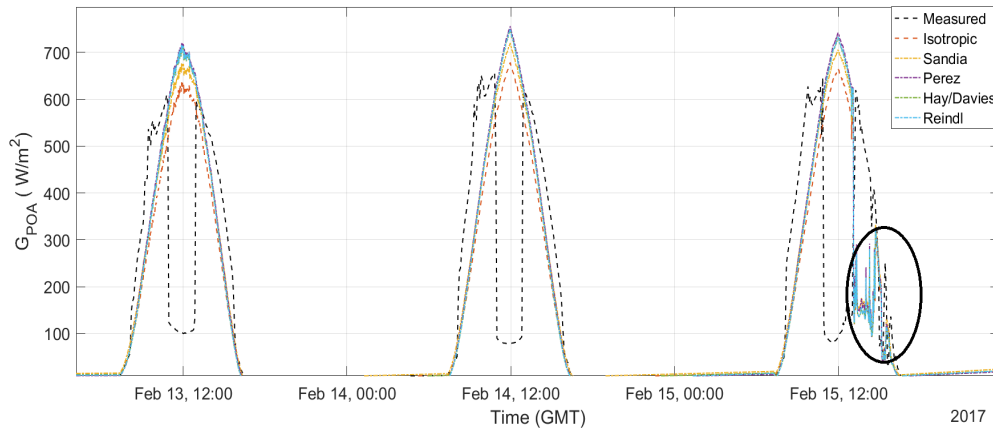
Figure 3.14: Measured and modeled incident irradiance on the e-bike station.
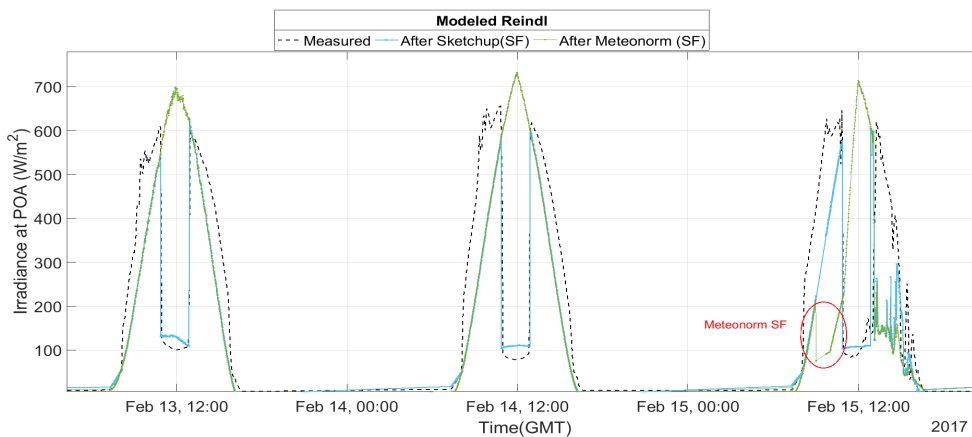
Figure 3.15: Measured and modeled incident irradiance on the e-bike station after using shading factor from Sketchup and Meteonorm-Horicatcher.

Figure 3.18, shows the modeled and measured irradiance for the same three days after using shading factor. Though Meteonorm uses a location-specific image, the shading factor obtained after image processing from Meteonorm is not as accurate as Sketchup. It can be seen that for the first two days, Meteonorm does not predict any shading. The reason could be that these two days must be completely cloudy days in its database($DNI = 0$) and therefore, it does not predict any shading. Even on days when it does predict SF (see region marked by red circle in fig. 3.18), it is not as accurate as it does not take care of shadows occurring within the hourly time steps [47]. Comparing the RMSD and MBD (figure 3.16), it is clear that using Sketchup is the most efficient way to model shading due to nearby objects. Use of shading factor from Sketchup decreased the RMSD by almost $50 \, W/m^2$ and MBD by $30 \, W/m^2$ for all the models.

To get a complete picture of the improvements in the irradiance prediction after using SF from Sketchup , bar charts comparing cumulative %RD for the models, are shown in figure 3.17. Each bar chart compares the percentage of the total number of samples which are in different ranges of % relative difference. The bottom most box (dark green) in each bar shows % of total samples less than 10% RD (indicated by number) whereas the topmost box (red) shows the % of samples having %RD greater than 80%. A model performs the best, if it has the highest percentage of samples in the bottom most box and least percentage of samples in the topmost box of the bar graph. From the two bar charts, it can be seen that the number of samples below 10% RD increased at least by 1% (except for Sandia model)

(a) RMSD comparison

(b) MBD comparison
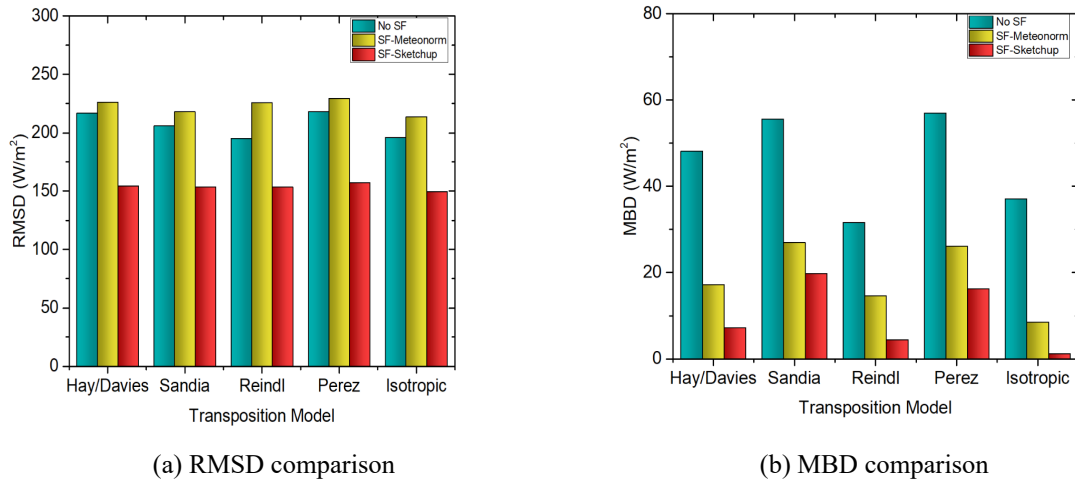
Figure 3.16: Root mean squared and mean bias differences between modeled(with and without shading analysis) versus measured for each of the five transposition models (based on Cabauw data Oct'16- Apr'17).

after using shading factor from Sketchup. Given the fact that most of the days were partially or fully cloudy during the observation period, an increase of 1% is also quite significant.

It is evident from the comparison of RMSD, MBD and %RD that Reindl, Hay/Davies and Isotropic are the best performing models for the location of the e-bike station .

(a) Without any shading factor

(b) After using shading factor from Sketchup.
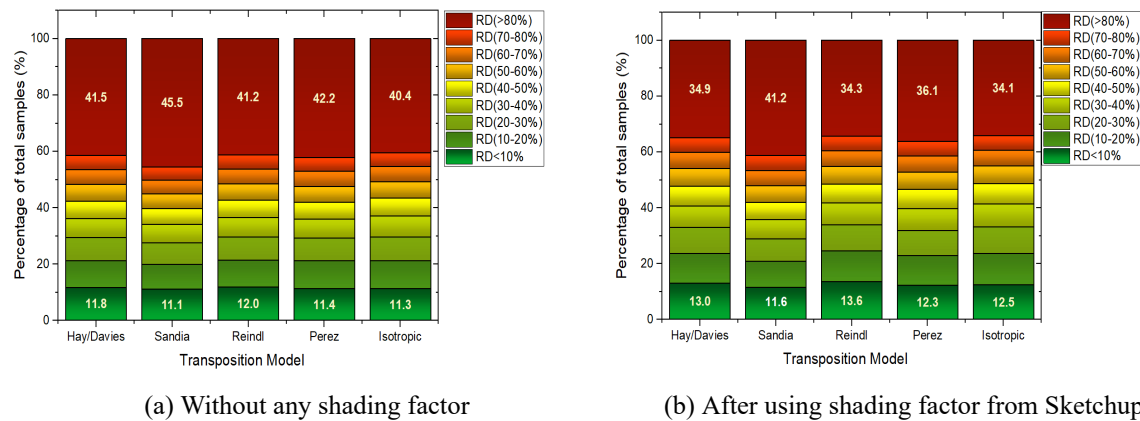
Figure 3.17: Comparison of standard transposition models based on cumulative % relative difference (based on Cabauw data Oct'16-Apr'17). The bottom most box (dark green) in each bar shows % of total samples less than 10% RD whereas the topmost box (red) shows the % of samples having %RD greater than 80%. versus measured for each of the five transposition models.

Effect of using location specific SVF and dynamic albedo

Figure 3.18 shows the comparison of cumulative %RD when Reindl model was modified using location specific parameters. The comparison is made among four different cases: first (No SF), when no SF is used and a fixed value of albedo (0.20) and module tilt dependent SVF (0.81) was used, Second (Sk-SF), when SF from Sketchup was used(albedo and SVF same as first case), third (Sk-(SF,SVF) when SF and SVF obtained from Sketchup were used whereas albedo value was constant and finally in the fourth case (Sk-(SF,SVF),Dy-Al), in addition to SF and SVF from Sketchup, albedo dependent on sun elevation was used.

It was found that the modeled value of SVF using Sketchup, not only increased the percentage of samples below 10% RD by 1% but also decreased the number of samples having %RD greater than

80% by 7%. On the other hand, the results did not improve with the use of 'dynamic albedo' i.e. albedo dependent on the sun elevation. Similar results for Hay/Davies and Isotropic models can be found in Appendix B. In the rest of the thesis, while referring to transposition models (Reindl, Hay/Davies and Isotropic) it is understood that the improvements suggested in this section are included.
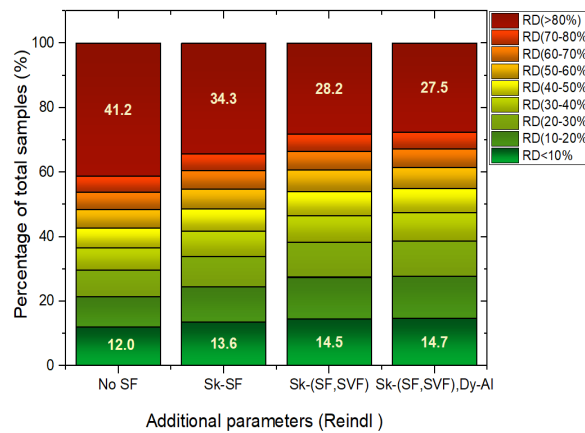
Figure 3.18: Comparison of cumulative % relative difference to evaluate effect of using location specific parameters on transposition model (Reindl) (based on Cabauw data, Oct'16-Apr'17).

It is implied from the results that location specific parameters such as SVF and albedo do improve the prediction of G_{POA}. It should be noted that the relation between albedo and sun elevation angle was found using just one day of albedo measurements and it can be further improved by taking measurements over a longer period. At the same time, the dependence of albedo on other factors such as clearness index, GHI and DNI should be studied.

Ray tracing method vs traditional transposition models
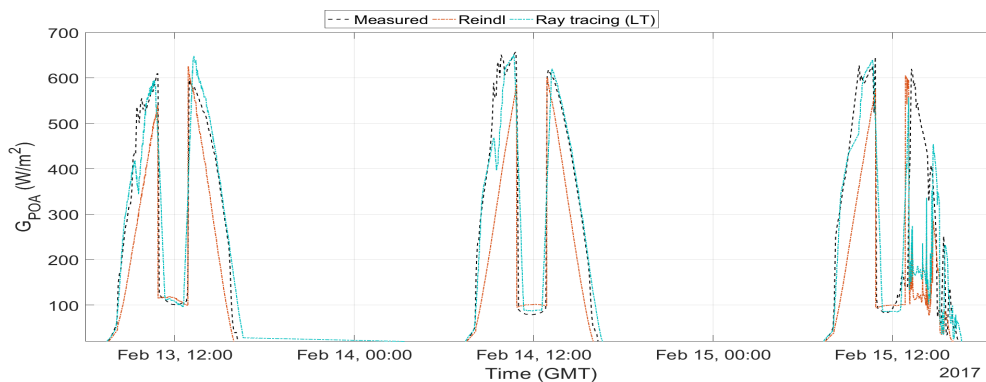
Figure 3.19: Measured and modeled incident irradiance on the e-bike station.

Irradiance on the plane of array was calculated using the new irradiance model by obtaining a sensitivity and a sky map for the location of the e-bike station. Figure 3.19 shows the comparison of modeled irradiance using improved Reindl model (includes location specific SVF and dynamic albedo) with that of the ray tracing method. It can be seen that the irradiance predicted using ray tracing almost overlaps with the measured data and though Reindl uses location specific parameters it underestimates the irradiance. This is mainly because Reindl only models sky diffuse, direct beam and ground reflected irradiance received by the modules but as the e-bike station is surrounded by buildings and trees there will be an additional reflected component from these objects as well. Since the ray tracing method uses simulations to calculate these reflections it is able to predict the measured irradiance more accurately.
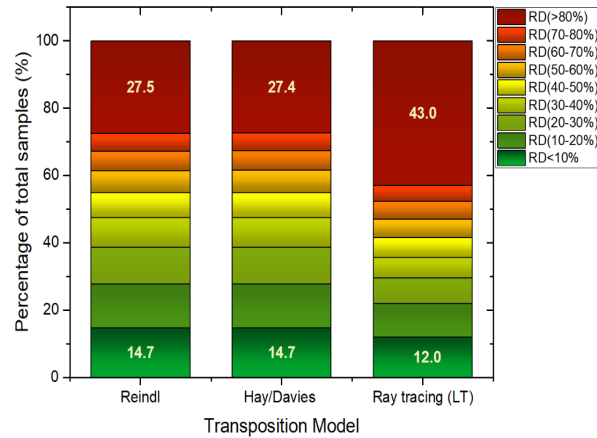
Figure 3.20: Comparison between standard transposition models and ray tracing method (LightTools) using cumulative % relative difference (based on Cabauw data Oct'16-Apr'17).

To compare the performance of the ray tracing method over the complete duration of the study (Oct'16-Apr'17), cumulative %RD was calculated. Figure 3.20 shows a comparison between the performance of the Reindl and Hay/Davies model with the ray tracing method. Surprisingly, the performance of the ray tracing method was found to be poorer than other models. The reason behind it could be understood by looking at the modeled irradiance by ray tracing method for a partly clouded day (see figure 3.20). During the morning hours, when there are a lot of fluctuations in irradiance, the irradiance predicted by ray tracing method differs more from the measured irradiance than the Reindl model does.However, in the afternoon (after 14:00 pm), the prediction almost overlaps with the measured values.The results imply that the performance of the ray tracing model is inferior to other models which perform better for cloudy conditions. Since the duration (Oct'16-Apr'17) over which model performance has been evaluated consist of mostly fully or partly cloudy days the overall result is poor. It is expected that it will perform much better for summer months when the number of clear sky days are much higher.
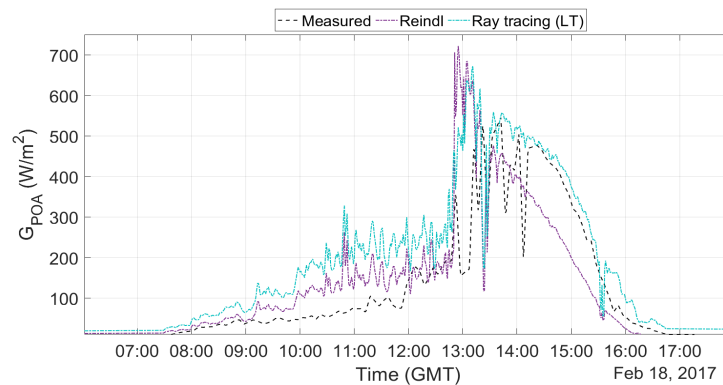
Figure 3.21: Measured and modeled incident irradiance on the e-bike station.

A combination of transposition and decomposition model

It is well known that for most locations, DHI and DNI data are rarely available, and they are obtained from GHI using decomposition models (For more details refer Chapter 2). Hence, it is important to verify the effect of using decomposition models in combination with transposition models to predict G_{POA}. Three decomposition models, namely Delft-I, Delft-II and OG, were chosen based on their performance to predict DHI from Cabauw and were combined with the Reindl transposition model.

Figure 3.22 indicates that the combination of models does not undermine the prediction of G_{POA}. The number of samples having %RD less than 10% differs only by 0.7% in case of Reindl and Delft-II-Reindl. However, to make definite conclusions about the performance of combinations of models, there is a need to study their performance over a complete year.
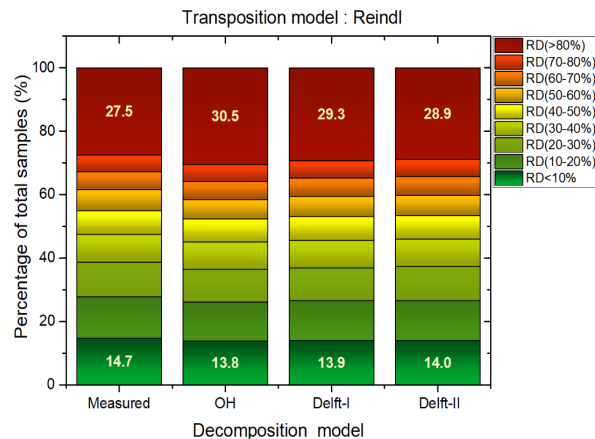
Figure 3.22: %Relative difference comparison for combination of decomposition and transposition models (based on Cabauw data Oct'16- Apr'17).

3.5. Conclusions

In this chapter, the following research questions were addressed :

Which are the most accurate transposition models to be used in urban location?

In this chapter, five widely used transposition models were studied and their performance was evaluated by comparing the modeled G_{POA} to the measured one, for the e-bike charging station on the campus of TU Delft based on the irradiance data for Oct'16-Apr'17 obtained from Cabauw. It was found that Reindl and Hay/Davies models are most suited for the climate of Netherlands.

How important is shading analysis to irradiance modeling and what is the most reliable technique to incorporate it?

For the location of the e-bike station, shading analysis can reduce RMSD in irradiance prediction by almost $50\ W/m^2$ (i.e almost 5% of incident power during noon) for all the models. Two different methods of shading analysis : Meteonorm-Horicatcher and 3-D modeling were compared. It was found that Sketchup is the most accurate way to do shading analysis. The number of modeled values having %RD below 10% increased by almost 1% and those having %RD greater than 80% decreased by almost 6% for the all the models except for the Sandia model. It is a significant percentage as the number of samples compared were 56,243.

How can the performance of existing models be improved by using location-specific parameters like sky view factor and albedo?

The effect of location-specific parameters like SVF and alebdo was studied on Reindl, Hay/Davies and isotropic models. Using 3-D modeling it is possible to account for near by buildings while calculating SVF. For the e-bike station, it was found to be 0.62. The

EEMCS building reduces the SVF by approximately 20%. Next, albedo near the e-bike station was measured, to improve the ground-reflected component, using an albedometer. It was found that the albedo value does not remain constant throughout the day and shows some correlation with the sun elevation angle. Using both location-specific SVF and elevation dependent, albedo improved the prediction of G_{POA} as the number of samples having %RD below 10% increased by almost 1% and those having %RD greater than 80% decreased by almost 7% for the all the models.

What is the effect of using decomposition models instead of measured diffuse and direct irradiance?

It was found that in the absence of measured DHI and DNI, decomposition models provide a good alternative to derive those values from GHI. When a combination of decomposition and transposition models was used, they produced almost equivalent results as compared to the use of just transposition models.

Finally, it can be concluded that the performance of existing models can be significantly improved by using location-specific parameters such as SVF and albedo. Further studies are needed to improve the prediction of the ground-reflected component.

4

Thermal modeling

To accurately predict the energy output of the e-bike station, it is necessary to have a good estimate of the individual cell temperatures under operating conditions. Several thermal models have been developed to predict the cell temperature and have varying degrees of complexity. The primary inputs to any thermal model are G_{POA} and T_{amb}. More complex models take into account effect of wind speed, module parameters, type of installation etc. The primary inputs can either be measured on the location of the PV system or can be modeled using data obtained from nearby meteorological stations. Generally, measured data is rarely available for installed systems and data is obtained from nearby weather stations.

In this project, as measured weather and module temperature data were available for the e-bike station, it is possible to evaluate the performance of different thermal models. Further, data from the Cabauw weather station was also used to see the difference in the performance of the models and evaluate factors affecting it.

In this context,as mentioned in chapter 1, the following research questions are addressed :

Evaluate thermal models best suited for predicting module temperature of a closed system like the e-bike station
- Which is the best performing thermal model?
- Does the time step between the data used for modeling have an impact on the performance of the models?
- What is the effect of using weather data from nearby meteorological stations on the performance of thermal models?

In this chapter, the three most widely used temperature models, namely NOCT, Duffie-Beckmann and Fluid-Dynamic, are evaluated. Their performance is validated by comparing the results obtained after modelling with measurements made at the e-bike charging station. Further, the effect of factors like varying wind speed and irradiance levels on the performance of the models is also studied.

Module Parameters

To discuss the details of thermal models, it is necessary to be familiar with module parameters which are used by them. In this section, relevant parameters are briefly explained.

Standard Test conditions (STC): It refers to the industry-wide accepted conditions for testing a solar module. At STC, modules are tested under an irradiance of 1000 W/m^2 having an AM 1.5 spectrum and a module temperature of 25°C. The module parameters defined on the datasheet of a PV module correspond to STC and often need to be calculated for ambient temperature.

Nominal Operating Cell Temperature (T_{NOCT}) : It is the temperature of a solar cell operating under an irradiance of 800 W/m^2 , ambient temperature of 20 °C and external wind speed of 1 m/s [1]. Usually, its value is provided by the manufacturer on the datasheet.

Installed Nominal Operating Cell Temperature (T_{INOCT}) It is the modified value of T_{NOCT} which considers the effect of module's mounting configuration. It can be determined experimentally by measuring the temperature of the installed modules under NOCT conditions. Table 4.1 summarizes the T_{INOCT} values for most commonly used configurations [21].

Table 4.1: Derivation of the T_{INOCT} from the T_{NOCT} for various mounting configurations [21].

Panel configuration	T_{INOCT}
Rack Mount	$T_{INOCT} = T_{NOCT} - 3\,°C$
Direct Mount	$T_{INOCT} = T_{NOCT} + 18°C$
Standoff	$T_{INOCT} = T_{NOCT} + X\,°C$
where X is given by	
W (inch)	X ($°C$)
1	11
3	2
6	-1

4.1. Thermal models

In this section, first, the scope of the thermal models, evaluated in this thesis (see table table 4.3), is discussed followed by a description about each model.

4.1.1. Scope of the Models

For this thesis, it is assumed that the complete solar module has an uniform temperature, which means that the module temperature (T_m) is assumed to be equal to the cell temperature (T_{cell}). In reality, the module temperature would be lesser than the actual cell temperature as absorption of light takes places in the cells. Still, the approximation is valid considering the relatively low thickness of the active layer and low heat capacity of the cell layer [19]. The approximation is also necessary because it is challenging to measure the cell temperatures as they are enclosed inside the module. The terms cell temperature and module temperature will be used interchangeably.

Table 4.2: Thermal models evaluated in this project. While comparing complexity of the models, 5 stars represent the highest level of complexity

Model Name	Input	Complexity
NOCT	$T_{amb}, T_{NOCT}, G_{POA}$	⋆
Duffied Beckman	$T_{amb}, T_{NOCT}, G_{POA}, \eta_{STC}, W_s$	⋆ ⋆
Fluid dynamic (Steady-state)	$T_{amb}, T_{NOCT}, G_{POA},$ W_s, module parameters	⋆ ⋆ ⋆
Fluid dynamic (Transient)	$T_{amb}, T_{NOCT}, G_{POA},$ W_s, module parameters	⋆ ⋆ ⋆ ⋆

4.1.2. NOCT model (NOCT)

It is one of the simplest models to calculate the operating temperature of the cell. The main input of this model is T_{NOCT}. It considers the effect of G_{POA} and ambient temperature(T_{amb}) but ignores the effect of wind speed (W_s). The expression for cell temperature (T_{cell}) is given by eqn. 4.1.

$$T_{cell} = T_{amb} + \frac{T_{NOCT} - 20°}{800} G_{POA} \tag{4.1}$$

4.1.3. Duffie-Beckmann model (DuffieB)

The Duffie-Beckmann model is an extension of the NOCT model, but it also takes into consideration the effect of wind speed on the temperature of the cells. It considers that at steady state, the solar energy incident on the module is transformed into thermal and electrical energy. At the same time, a part of the thermal energy is dissipated to the environment by heat transfer. The energy balance of a unit area of the module is given by the equation 4.2 [22, 23].

$$(\tau\alpha)G_{POA} = \eta_m G_{POA} + U_L(T_{cell} - T_{amb}) \tag{4.2}$$

Where, τ is the transmittance of the front surface and α is the absorbance of the PV layer. U_L is the thermal loss coefficient that accounts for losses due to convection, conduction and radiation. η_m is the module's electrical efficiency. The transmittance-absorbance product is used to predict the total energy absorbed by the module. The value of $\tau\alpha$ is generally not known and an approximated value of 0.9 is widely used [22].

Substituting eqn. (4.2) with NOCT conditions, one obtains eqn. 4.3 which can be then combined with eqn. 4.1 to obtain the cell temperature at any ambient temperature (see eqn. 4.4).

$$(\tau\alpha)800 = \eta_m G_{POA} + U_{L,NOCT}(T_{NOCT} - 20) \tag{4.3}$$

$$T_{cell} = T_{amb} + \frac{G_{POA}}{800}\left(\frac{U_{L,NOCT}}{U_L}\right)\frac{T_{NOCT} - 20°}{800}\left(1 - \frac{\eta_m}{\tau\alpha}\right) \tag{4.4}$$

Further, Duffie-Beckmann approximated the loss coefficients (U_L and $U_{L,NOCT}$) using an empirical relation in terms of W_s . The final correlation to obtain T_{cell} is given by eqn. 4.5.

$$T_{cell} = T_{amb} + \frac{G_{POA}}{800}\left(\frac{9.5}{5.7 + 3.8W_s}\right)\frac{T_{NOCT} - 20°}{800}\left(1 - \frac{\eta_m}{\tau\alpha}\right) \tag{4.5}$$

4.1.4. Fluid-Dynamic (FD) Model

The fluid dynamic model is based on detailed thermal energy balance between the module and its surroundings. It was first developed by Sandia National Laboratories (SNL) to improve the prediction of module temperature using commonly available weather data and module parameters [21] [5]. The main inputs for this model are T_{INOCT}, T_{amb}, G_{POA}, W_s and other module parameters such as thermal coefficients, the area of the module, etc. Another simplified version of FD model was developed which solves the energy balance equation assuming the steady state condition [19]. The original model by SNL will be referred to as the "FD- Transient (FD-TR)" and the simplified one as "FD-Steady state (FD-SS)".

The main assumption for both the models is that the module is a single uniform mass at temperature T_m and exchanges heat with the surroundings by conduction, convection and radiation (refer fig. 4.1).
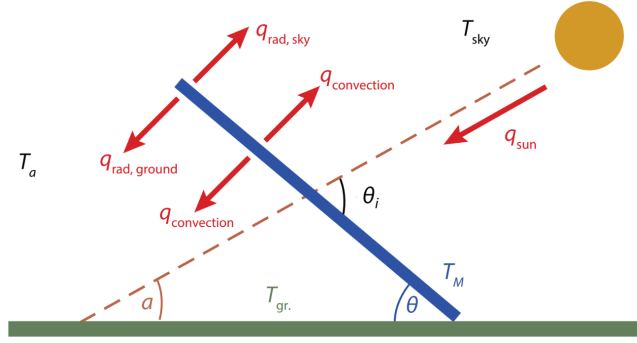
Figure 4.1: Image showing net heat exchange between a tilted module surface and the surroundings.

The balance of heat transfer is given by eqn. 4.6 .

$$mc\frac{dT_M}{dt} = \varphi G_{POA} - h_c(T_M - T_{amb}) - \varepsilon_{top}\sigma\left(T_M^4 - T_{sky}^4\right) - \varepsilon_{back}\sigma\left(T_M^4 - T_{gr.}^4\right) \tag{4.6}$$

The equation 4.6 can be divided into four parts as explained below. The term on the left side of the equation, mc, represents the thermal mass of the module where m is the mass of the module and c is the heat capacity of the module.

On the right-hand side,

The first term φG_{POA} represents the total energy absorbed by the module from the incident irradiance where phi is the absorptivity of the module. The second term, $h_c(T_M - T_{amb})$, accounts for the heat exchanged with the surrounding air by convection from both front and back surface of the module. Here, h_c denotes the overall convective heat transfer coefficient of the module.

The next two terms take care of heat exchange by radiation. $\varepsilon_{top}\sigma\left(T_M^4 - T_{sky}^4\right)$ calculates the radiative heat exchange between the upper module surface and the sky whereas $\varepsilon_{back}\sigma\left(T_M^4 - T_{gr.}^4\right)$ calculates the radiative exchange between the back surface and the ground. ε_{top} and ε_{top} are the emissivity of the module's top and back surfaces respectively. σ is Stefan-Boltzmann's constant and T_{sky} and T_{grnd} are the temperatures of the sky and the ground respectively. The above equation ignores the conductive heat transfer between the module and the mounting structure as its contribution is negligible, given the small area of contact between modules and the structure. Equation 4.6 can be further simplified by linearizing the radiation terms using relation (eqn. 4.7) .

$$(a^4 - b^4) = \left(a^2 + b^2\right).(a + b).(a - b) \tag{4.7}$$

It is safe to assume the product term ,$\left(T_M^2 + T_{sky}^2\right).\left(T_M + T_{sky}\right)$, as a constant since it changes less than 5% for a 10° variation in module temperature [21]. Therefore, the radiation terms can now be expressed as given by eqns. 4.8 and 4.9.

$$h_{r,sky} = \varepsilon_{top}\sigma\left(T_M^2 + T_{sky}^2\right).\left(T_M + T_{sky}\right) \tag{4.8}$$

$$h_{r,gr.} = \varepsilon_{back}\sigma\left(T_M^2 + T_{gr.}^2\right).\left(T_M + T_{gr.}\right) \tag{4.9}$$

Finally, the energy balance equation eqn. 4.6 can be rewritten as

$$mc\frac{dT_M}{dt} = \varphi G_{POA} - h_c(T_M - T_{amb}) - h_{r,sky}\left(T_M - T_{sky}\right) - h_{r,gr.}\left(T_M - T_{gr.}\right) \tag{4.10}$$

Two types of solutions (steady state and transient + steady state) can be obtained from the equation.

The FD-Steady State model considers that if the time step between changes in the irradiation is greater than 10 minutes, the module can be assumed to be in a steady state. This approximation is valid because, due to the thermal mass of the module, its temperature does not change significantly over a short period (10 minutes) when compared to change in irradiation. Rather, module temperature follows an exponential lagging behind the variations in irradiation and has a time constant of around 7 minutes [19]. With this approximation, the term on the right-hand side of eqn. 4.10 becomes zero and the equation can be rearranged to obtain the T_M as given by eqn. 4.11.

$$T_M = \frac{\varphi G_{POA} + h_c T_{amb} + h_{r,sky} T_{sky} + h_{r,gr.} T_{gr.}}{h_{r,sky} + h_{r,gr.} + h_c} \tag{4.11}$$

The FD-Transient model makes no such assumptions and models irradiance as a linear function of time, given by eqn. 4.12.

$$G_{POA} = G_{POA,(t-1)} + \Delta G_{POA} \frac{t}{\Delta t} \tag{4.12}$$

Where, Δt is the time step between measurements, $G_{POA,(t-1)}$ is the insolation from the previous time step and ΔG_{POA} is the smallest step change in G_{POA}. Δt is assumed to be small enough so that the equation remains continuous. Therefore, by substituting eqn. 4.12 in the eqn. 4.11 and integrating it, an explicit expression for T_M can be obtained, given by eqn. 4.13.

$$T_M = \frac{(\varphi(G_{POA,(t-1)} + \Delta G_{POA}/L) + h_c T_{amb} + h_{r,sky} T_{sky} + h_{r,gr.} T_{gr.})(1 - e^L) + \varphi \Delta G_{POA}}{h_{r,sky} + h_{r,gr.} + h_c} + T_{M,(t-1)} e^L \tag{4.13}$$

Where $T_{M,(t-1)}$ is the module temperature from the previous step and

$$L = \frac{-(h_{r,sky} + h_{r,gr.} + h_c).\Delta t}{mc}$$

In general, the term $1/L$ represents the thermal lag or the capacitance of the module. To obtain T_M from either the FD-SS or FD-TR model, one has to calculate various parameters like h_c, h_{sky}, etc. The detailed description to calculate them can be found in the following references [19, 21].

Since the FD-SS model assumes that the module temperature does not change significantly for a shorter time step, it might lead to an erroneous prediction of module temperature especially when irradiance values are high and are fluctuating. Also, as the time step between two data points is 1 minute, it is likely that due to the assumptions (about steady state) made by FD-SS, it will underperform as compared to the reported performance in the literature [19]. FD-TR is expected to have a superior performance as it considers the effect of continuous variation in irradiance as well as ambient temperature.

4.2. E-bike station and assumptions

Solar panels and its parameters

The e-bike station has 8 Sunpower X20 – X20-327 BLK solar panels. These panels are based on monocrystalline silicon technology and have an average efficiency of 20.3%. The main module parameters are summarized in table 4.3. More details about the modules can be found in the appendix E.

This section gives the details of the parameters which were calculated differently than the references, to incorporate the effect of location and modules used in the e-bike station.

Table 4.3: Data sheet values of Sunpower X20 327 W_p PV module.

Name	Value
Brand	Sunpower X20-327-BLK
Type	Mono-crystalline silicon
Pmax STC(W)	327
T_{NOCT} (°C)	43
Width (m)	1.56
Height (m)	1.05
Area (m^2)	1.64
Efficiency nom. STC (%)	20.3
V_{oc} STC (V)	67.6
I_{sc} STC (A)	6.07
Temp. coeff Pmmp (%/°C)	-0.3
Temp. coeff Voc (%/°C)	-0.3
Temp. coeff Isc (%/°C)	0.06

Absorptivity and emissivity

Absorptivity (φ) and emissivity (ϵ) of the solar module are critical inputs for the Fluid-Dynamic model. Absorptivity is defined as the fraction of incident radiation that gets converted into thermal energy [22]. It is related to the reflectivity (R) and efficiency (η_m) of the module as given by the equation

$$\varphi = (1 - R)(1 - \eta_m) \tag{4.14}$$

Emissivity (ϵ) is the ratio of energy radiated to the amount that would be radiated if the surface was a perfect black body [22]. For this thesis, absorptivity and emissivity were based on the work of Wei Li et al. , who experimentally calculated these values for Sunpower's solar modules (same as that used in e-bike station) [48]. The module efficiency was obtained from the module's datasheet. Table 4.4 summarizes all these values.

Table 4.4: Module parameters

Parameter	Value
Reflectivity(R)	0.07
Efficiency (η_m)	0.203
absorptivity (φ)	0.727
Emissivity top (ϵ_{top})	0.63
Emissivity back (ϵ_{back})	0.66

Wind speed

Though wind speed data is measured at the e-bike station, while using data from Cabauw, it was scaled down using eqn. 4.15 because, at the meteorological station, wind speed is measured at a height of 10

meters whereas the height of panel in the e-bike station is around 4 meters [49].

$$W_s = W_{s,ref} \, ln(h/z_0)/ln(h_{ref}/z_0) \tag{4.15}$$

where,

W_s= wind speed at height h above ground level.

$W_{s,ref}$= reference speed, i.e. a wind speed we already know at height h_{ref}. h = height above ground level for the desired velocity.

z_0 = roughness length in the current wind direction. Roughness lengths are summarized in the table D.1 appendix D. In this thesis, a value of 0.8 is used, which refers to a location having large buildings.

h_{ref} = reference height, i.e. the height where we know the exact wind speed $W_{s,ref}$.
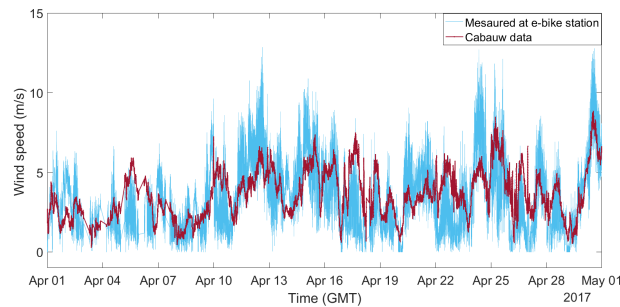
Figure 4.2: Measured (e-bike station) and modeled wind speed using wind speed measured at Cabauw for one week in April-17.

Figure 4.2 shows a comparison between wind speed measured at the e-bike station and the scaled down version of wind speed data from Cabauw for one week of April. It can be seen that the scaled wind speed data matches well with the actual recorded data. The measured and modeled values have an RMSD of 0.226 m/s. It is important to note that due to the presence of EEMCS building just in front of the e-bike station, the wind often becomes turbulent and is very difficult to model.

Ambient Temperature

Figure 4.3 shows a plot of ambient temperature measured at the e-bike station and at Cabauw weather station. The measured temperature at both the locations matches very well, except for the night time when the temperature measured at Cabauw is lower than that measured at the e-bike station. It is mostly because the Cabauw weather station is located in a remote area, surrounded by vegetation. As the concerned period for evaluating module temperature is during the day, these differences will not affect the performance of the thermal models.
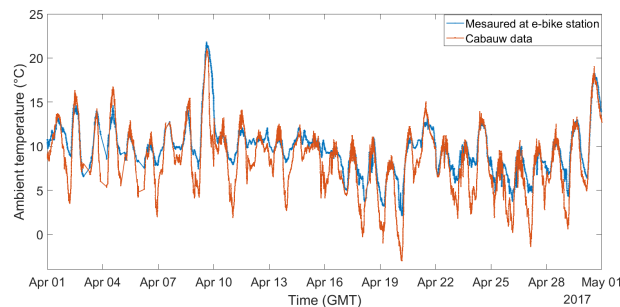
Figure 4.3: Measured ambient temperature at the e-bike station and Cabauw weather station.

Module temperature at INOCT

T_{INOCT} is the value of T_m of an installed module when it is subjected to NOCT conditions. Though table 4.1 gives a generalized formula to obtain the T_{INOCT} values for an installation, considering the unique design of the e-bike station, it would be more accurate to get it from the measured module temperatures. Therefore, the complete dataset of recorded module temperatures was scanned for conditions which correspond to NOCT conditions ($T_{amb} = 20\ °C$, Irradiance = $800\ W/m^2$ and $W_s = 1\ m/s$) and the set of values found (refer figs. 4.4 and 4.5) was averaged to obtain the value of T_{INOCT}. A value of $52.5°C$ was obtained using this method and is used as the T_{INOCT} for rest of the calculations.
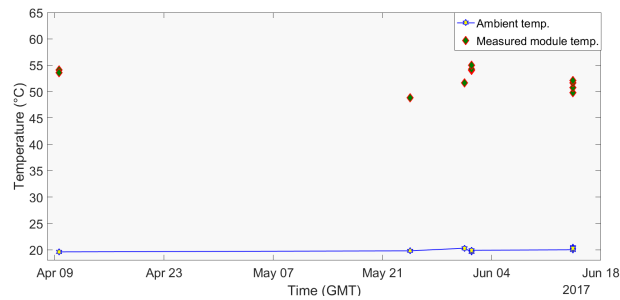
Figure 4.4: Measured module temperature of e-bike station at approx. NOCT conditions.

If one refers to table 4.1, the value of X becomes $9.5°C$ which is also logical as the mounting configuration of panels in the e-bike station is similar to a standoff configuration having a width of 5 inches but closed on all sides. Additionally, the experimentally determined value of T_{INOCT} also gives the least RMSD when used to calculate the module temperature using Fluid-Dynamic model (FD-TR).
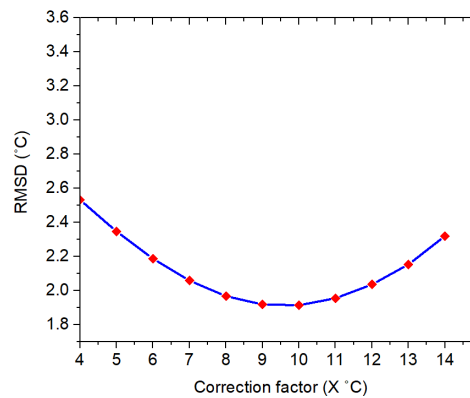
Figure 4.5: Comparison of root mean squared difference modeled versus measured module temperature for different values of INOCT correction factors.

4.3. Model comparison

4.3.1. Data description

For comparing thermal models, data from Cabauw and the e-bike station was used. For more details about the datasets, refer section 2.3.1 and 3.4.1 . The specific changes applied to those datasets are discussed below.

Time span

E-bike data for the duration of March-May 2017 was used for studying the performance of the thermal models. The reason behind limited months of data is that the module's temperature sensors were not

working initially and became fully functional only after 8th March 2017. In the case of Cabauw data, measurements from only April-17 were available to compare the results. Details of the datasets along with the periods when data were missing are available in the appendix C.

Data checks

In addition to data checks performed in section 2.3.1 and 3.4.1, while comparing the measured and predicted module temperatures, attention was given to remove data points having spurious wind speeds and ambient temperatures. Records corresponding to wind speed less than 0 and ambient temperature below -25 $°C$ and above 45 $°C$ were removed from all the data sets.

Once all the data checks were performed, the final data set consisted of 40,357 in the case of Cabauw data and 69,759 in the case of e-bike data samples. Table 4.5 summarizes the datasets used in this chapter.

Table 4.5: Summary of database used in this chapter

Database name	Source	Period	Variables used	Purpose
e-bike data	E-bike station, Delft, Nl	Mar. '17-May'17	$T_{amb}, T_M,$ W_s, G_{POA}	Used to compare accuracy of thermal models
Cabauw data	CESAR, Nl	Apr. '17	$T_{amb}, W_s,$ GHI, DNI, DHI	To evaluate effect of using data from nearby meteorological station on performance of thermal model

4.3.2. Statistical parameters

The performance of the models was evaluated using four different statistical indicators which are MBD ($°C$), % RD, RMSD ($°C$) and R-square(R^2). For more details of RMSD, MBD and %RD, refer section 2.3.2.

R-Square R-square is a widely used statistical parameter to determine how well a mathematical model fits the measured data [50, 51]. It determines the closeness of modeled data to the fitted regression line and can be expressed by eqn. 4.16).

$$R^2 = \frac{Explained\ variation}{Total\ variation}$$ (4.16)

Values of R^2 always lie between 0 to 1 where 0 indicates that the model fails to explain the variability of the response around its mean and 1 means that the model completely fits the data. A higher value of R-square indicates that the data points fall close to the fitted regression line and the used model can predict the measured data very well.

4.3.3. Evaluation of thermal models

In this section, performance of the thermal models is evaluated using e-bike data (see 4.3.1) for the duration of Mar-May'17. Measured ambient temperature, wind speed and incident irradiance at the e-bike station are used as inputs to the thermal models and the predicted values are compared with the recorded module temperature.

Measured module temperature is close to the ambient temperature at night but during the day it increases significantly. The difference between the two can become more than 40 $°C$ on a bright sunny
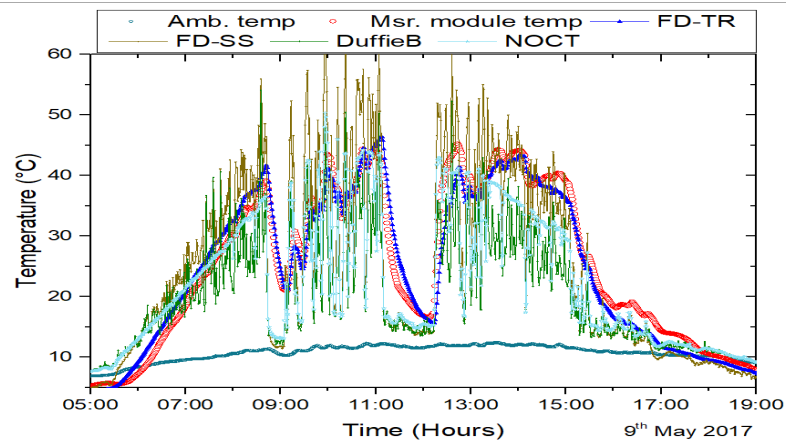
Figure 4.6: Comparison of temperatures predicted by thermal models with the measured module temperature.

day. Figure 4.6 shows a plot of modeled as well as measured module temperature for a day (9-May-17). It can be observed that the predicted values by FD-TR almost overlap with the measured values. FD-SS and NOCT models also predict the temperature within a close range, but during higher module temperatures (corresponding to higher G_{POA}) the deviation is higher. Duffie-Beckmann is found to predict temperatures less than the expected.

To compare the performance of the modules quantitatively, scatter plots between measured and modeled module temperatures are shown in Figure 4.7. A model is perfect when all the dots on the scatter plot are aligned close to the diagonal line.
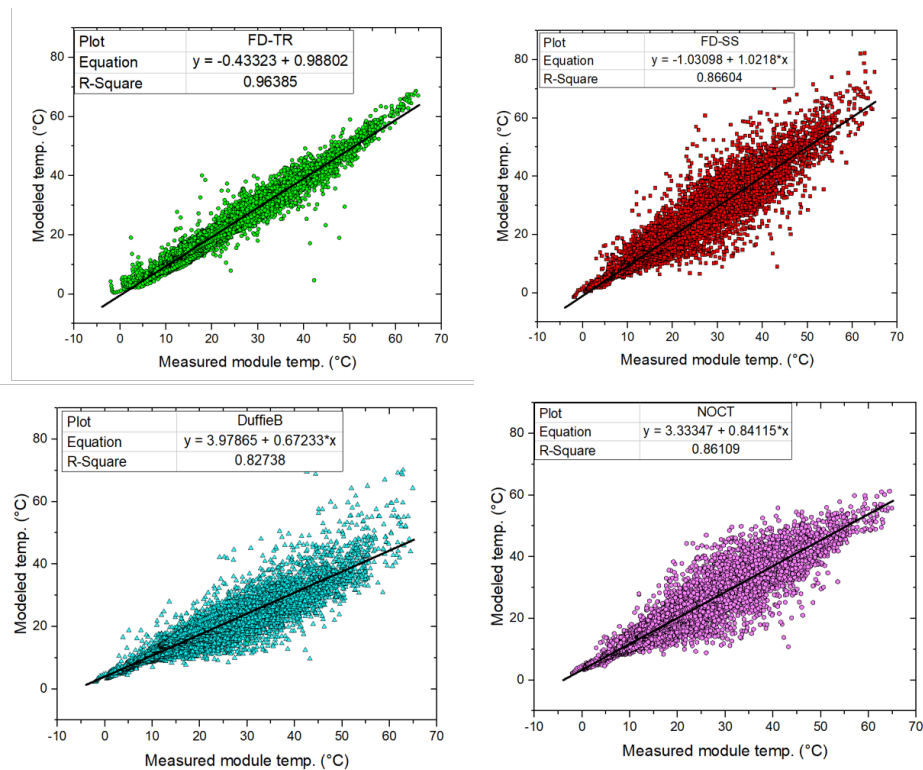
Figure 4.7: Scatter plot of thermal models.

It can be seen that FD-SS has the least spread in data points and has the most linear relationship. Com-

paring the R-square values for each of the scatter plots, it can be said that the FD-TR is the best per-forming model followed by FD-SS and NOCT model. The findings are also supported by comparison of cumulative % relative differences in the prediction of module temperature as shown in figure 4.8. Each bar in the figure compares the percentage of the total number of samples which are in different ranges of % relative difference. The bottom most box (dark green) in each bar shows % of total samples with less than 10% RD (indicated by number) whereas the topmost box (red) shows the % of samples having %RD greater than 80%. A model performs the best if it has the highest percentage of samples in the bottom most box and least percentage of samples in the topmost box of the bar graph. From the bar chart, it is evident that, using FD-TR, more than 90% of samples have less than 20% RD indicating that it is able to accurately predict module temperature.
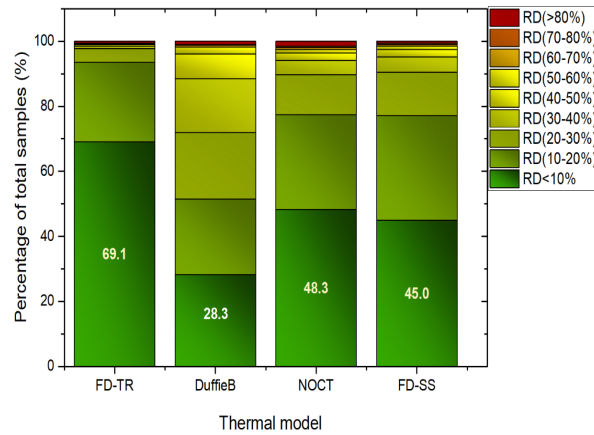
Figure 4.8: Comparison of thermal models based on cumulative % relative difference (using e-bike data Oct.'16-Apr.'17). The bottom most box (dark green) in each bar shows % of total samples less than 10% RD whereas the topmost box (red) shows the % of samples having %RD greater than 80%.

The results of MBD and RMSD, as shown in table 4.6, also indicate that FD-TR has the lowest RMSD (1.91 $°C$) and MBD (-0.72 $°C$).Therefore, FD-TR is the most suited model for predicting the temperature of modules at the e-bike station.

Table 4.6: RMSD and MBD of thermal models

Model name	MBD ($°C$)		RMSD ($°C$)	
	Minute data	Hourly data	Minute data	Hourly data
FD-TR	-0.70	-0.69	2.34	2.05
DuffieB	-3.39	-3.36	6.23	5.66
NOCT	-0.24	-0.13	4.35	3.25
FD-SS	-0.54	-0.67	4.72	2.72

Another interesting observation is that though both FD-SS and FD-TR models are derived from same equations and only differ in the way a solution of the energy balance equation is found, there is a significant difference between their performance. Figure 4.9, displays the plot of modeled temperature using the FD-TR and FD-SS models for two days in May-17. The first day (May 5th) has lower values of incident irradiance as compared the second one (May 6th) which was a clear-sky day. The effect of the difference in irradiance can be easily seen on the module temperature. From the subfigure 4.9b, it is seen that, when hourly weather data was used to predict the module temperature, both the models
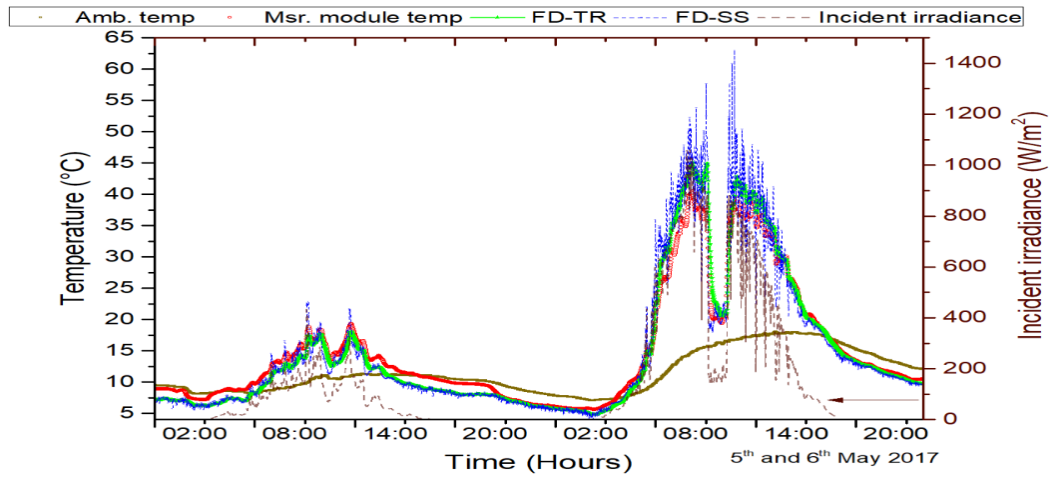
(a) Data with time step of 1 Minute
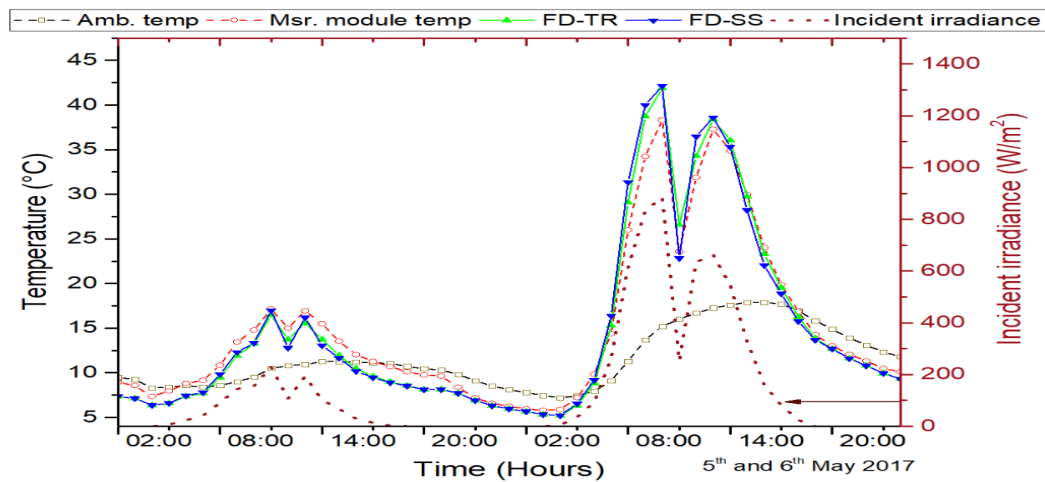
(b) Data with time step of 1 Hour

Figure 4.9: Modeled module temperature by FD-TR and FD-SS as compared with measured temperature for two days in May 2017.

predicted similar module temperature with minimal variation for both the days. On the other hand, when per minute data was used (see subfigure 4.9a), FD-SS greatly overestimates the variability in the module temperature for higher values of incident irradiance on the clear sky day.The difference is negligible for lower values of irradiance on both the days. The FD-SS model is based on the assumption that the module temperature does not change for a time step of 10 minutes (see section 4.1.4) and thus, neglects the effect of continuously varying irradiance on the module temperature [19]. The assumption does not have much effect for low values of irradiance but for higher values, it introduces a large error in the prediction. Statistical results (refer table 4.6) also indicates that the performance difference between FD-TR and FD-SS, when using hourly data steps, is almost negligible. The difference between MBD is almost zero and for RMSD is just $0.7\,°C$.

To see the effect of different time steps on the performance of FD-SS and FD-TR, additional simulations were run, using data having temporal resolution of 5 minutes, 15 minutes and 30 minutes. Figure 4.10, shows the differences in RMSD as the time step between data point changes. It is clear that, as the time-step decreases, the performance of FD-SS model declines. Further, it can be said that FD-SS model should only be used when the step size between measured data is much greater than 10 minutes.
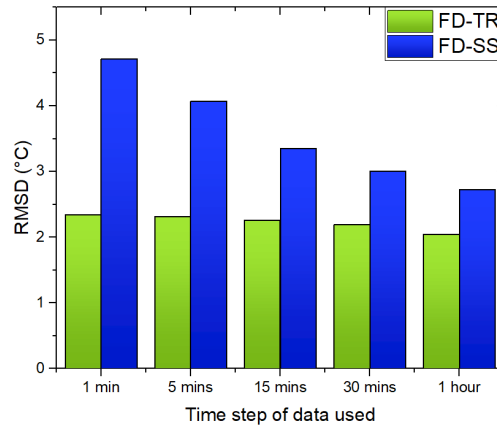
Figure 4.10: RMSD for FD-TR and FD-SS for different time steps.

Effect of using modeled input data

In the previous section, the performance of models was analyzed using measured weather data at the e-bike station as an input to the models. However, measured weather data is not always available for all the locations and one might have to obtain it from nearby weather stations. In such a case, irradiance received by the modules, is obtained using transposition models (discussed in chapter 3) and wind speed is be scaled down to the system's height (see section 4.2).

To study the effect of using meteorological data that is not measured on the module's location, data from Cabauw for the month of April'17, was used. Figure 4.11 shows the RMSD for the four models for three different cases as compared to the case where both G_{POA} and W_s were measured at the e-bike station. In the first one, W_s was scaled down for the location of e-bike station whereas measured values of G_{POA} were used (Mod. W_s + Msr. G_{POA}). In the second case, G_{POA} was modeled using a transposition model (Reindl as discussed in Chapter 3) whereas W_s used was locally measured (Mod. G_{POA} + Msr. W_s). Finally, for the third case, modeled versions of both W_s and G_{POA} were used (Mod. W_s + G_{POA}). 'Msr. W_s + G_{POA}' indicates results when both the values measured at e-bike station were used as an input and all other results are compared to it. Comparing the RMSD in temperature prediction, it can be seen that, when using Mod. W_s + G_{POA}, the RMSD increases more than $8°C$ as compared to just $2°C$ for both Msr. W_s + G_{POA}. The decrease in quality of T_m prediction is acceptable given the fact that effect of inaccuracies in module temperature do not have much effect on power prediction as compared to the effect of inaccuracies in G_{POA} prediction (discussed in chapter 5, refer 5.4).

It is also clear that the performance of models is highly dependent on the value of G_{POA} as compared to W_s. It can be explained by the fact that G_{POA} is the main source of heat produced in the module and hence its knowledge is important for predicting module temperature whereas the role of W_s is limited to cooling down the module. Thus, the accuracy of transposition models not only affects G_{POA} prediction but also the prediction of module temperature.

4.3.4. Discussion

In this section, a brief discussion is presented analyzing the performance of the different models evaluated in this chapter.

In general, it was seen that FD-TR is the best performing model followed by FD-SS and NOCT models. Duffie-Beckmann was found to have the least accuracy in predicting he module temperature. Surprisingly, NOCT model was found to be as good as the FD-SS model mainly because the FD-SS model is not designed for predicting module temperature when the time step between data points is less than 15 minutes. It was also observed that the performance of FD-SS improves significantly for hourly data. FD-TR takes care of all the shortcomings of the other three models and is able to predict module
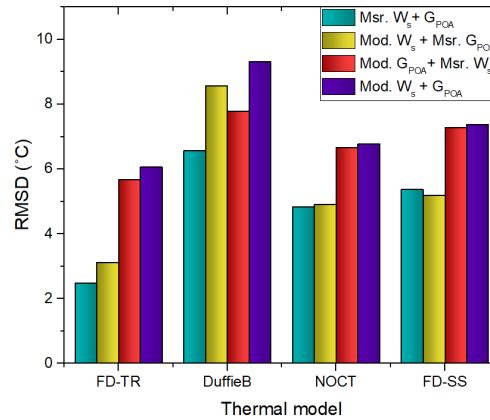
Figure 4.11: Root mean squared differences between modeled versus measured module temperature using Cabauw data for April '17. The results are compared for four cases,ie 1) Measured (Msr.) W_s and G_{POA} used as input to thermal models, 2) Modeled (Mod.) W_s and Msr. G_{POA}, 3) Mod. G_{POA} and Msr. W_s, 4) Mod. W_s and G_{POA}.

temperature accurately.
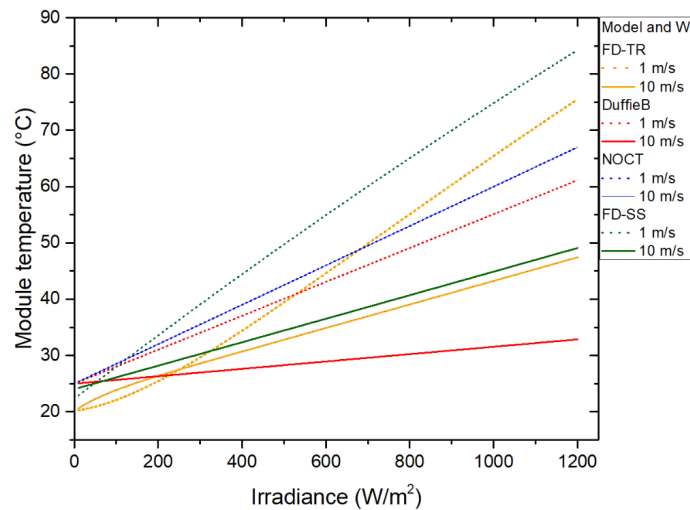
Figure 4.12: Performance of thermal models under varying incident irradiance for two different wind speeds.

The performance differences can also be understood by observing the effect of incident irradiance and varying wind speed, for constant ambient temperature, on the modeled temperatures (see figure 4.12). The NOCT model does not consider the effect of wind speed, but it does follow the increase in module temperature due to increased incident irradiance. Its accuracy decreases at higher wind speeds as the difference between module temperature and T_{NOCT} becomes significant. Duffie-Beckmann predict T_m lower than other models and the difference becomes notable as the irradiance increases. It underperforms because of two reasons. First, it uses T_{NOCT} as an input whereas for more accurate predictions T_{INOCT} should be used, incorporating the effect of mounting configuration on T_m. Secondly, it keeps convective heat transfer as a constant. Usually, heat transfer coefficients change with wind speed and mounting configuration of modules. FD-TR and FD-SS models predict module temperature in-between NOCT and Duffie-Beckmann models and show dependence on both wind speed and incident irradiance. The difference between FD-SS and FD-TR becomes pronounced at lower wind speeds where FD-SS predicts higher temperatures than FD-TR. It is because FD-SS ignores the thermal mass

of the module which plays an important role at lower wind speeds.

Finally, observing the performance of the models when meteorological data from a nearby station was used as an input to the thermal models, it can be said that most of the error in T_M prediction was introduced due to inaccuracies in the transposition model and not by the thermal models themselves.

4.4. Conclusions

Knowledge of the module temperature is critical for modeling the power output of a solar cell. Several models exist to predict the module temperature from ambient temperature and have different degrees of complexity. In this chapter, three thermal models were studied, namely NOCT, Duffie-Beckmann and Fluid-Dynamic, to compare the modeled and measured module temperature at the e-bike station for the duration of March to May 2017. Additionally, the effect of using steady-state assumptions for the Fluid-Dynamic model (FD-SS) was evaluated.

In this chapter, the following research questions were addressed :

> *Which is the best performing thermal model?*
>
> Analyzing the results discussed in section 4.3.3, it can be said that FD-TR is best suited for predicting the module temperature at the e-bike station. It has the least RMSD of $1.91°C$ and an MBD of $-0.71°C$. It has the highest number of samples having (69%) %RD less than 10%.

> *Does the time step between the data used for modeling have an impact on the performance of the models?*
>
> Not all the models are affected by the time-step of the data used except for the FD-SS model. Even for the FD-SS model, the performance with minute data is poor only for higher values of incident irradiance. The overall performance of FD-SS increases significantly when the time step between samples is increased to an hour instead of a minute.

> *What is the effect of using weather data from nearby meteorological stations on the performance of thermal models?*
>
> The effect of using weather data from the nearby meteorological station (Cabauw data, April-17) as an input to the thermal models was evaluated. Results showed that use of modeled G_{POA} and W_S introduces higher errors in the prediction of module temperature as compared to the case when measured G_{POA} and W_S are used, but the errors are within the acceptable range. It was observed that most of the error gets introduced due to inaccuracies in the transposition model and not by the thermal models itself. Thus, there is a strong need to improve transposition models.

In general, it was observed that the NOCT model predicts higher values of module temperature as it does not take wind speeds into account. The Duffie-Beckmann model underperforms as it does not consider the effect of the mounting configuration on convective heat transfer. Finally, it can be concluded that, to accurately model the temperature of the modules mounted on a closed system like the e-bike station, the FD-TR model should be used. The NOCT model is found to be the second best, despite its simplistic nature and thus can be employed for predicting module temperatures when one wants to avoid complicated calculations involved with FD-TR model.

<div align="right">

5

</div>

Electrical modeling : DC power and energy yield

A number of models exist to predict the electrical output of PV cells. To accurately predict the power produced by the e-bike station, it is important to use the best performing electrical model.

In this context, as mentioned in chapter 1, the following research questions are addressed:

> **Compare existing solar cell electrical models to compute the DC power and energy output of the e-bike charging station**
>
> - How accurate are the existing electrical models?
>
> - How much effect do the inaccuracies in the irradiance and thermal models have on the energy yield prediction of the system?
>
> - Using the method of the designer of the e-bike station, how well does the energy yield predicted match with the measured data after installation?
>
> - Do the improvements suggested in this thesis improve the quality of prediction of energy yield?

The primary inputs to any electrical model are G_{POA} and T_M which can be either measured on the location of the PV system or can be modeled using data obtained from nearby meteorological stations. While measured G_{POA} and T_M can be obtained for an installed system, it has to be obtained from nearby weather stations when designing a new system. Apart from G_{POA} and T_M, models use module parameters, which are either given on the module datasheet or obtained experimentally.

In this project, first, the performance of electrical models is evaluated by comparing modeled power output (using measured G_{POA} and T_M at the e-bike station) with the measured power output. Next, weather data from Cabauw is used to obtain G_{POA} and T_M (using transposition and thermal models) which was then used as an input to the electrical models. Figure 5.1 shows the flowchart of the above explained comparison.
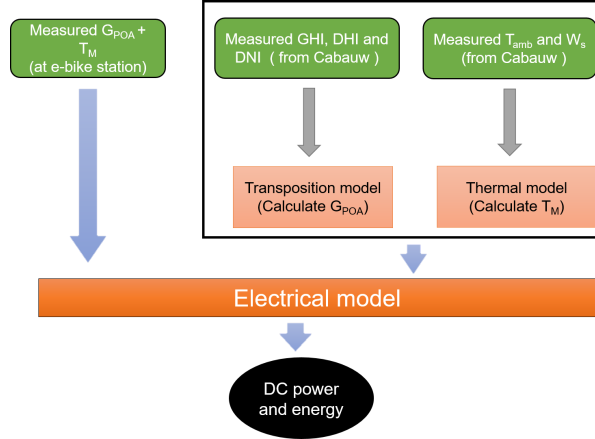
Figure 5.1: Evaluation of electrical model using data obtained locally and from nearby meteorological station.

The next section gives a brief description of the two types of electrical models compared in this chapter. The choice of models was affected by factors like availability of pre-requisite module parameters and reported performance of the models in literature [19, 26, 27, 52].

5.1. Electrical models

Electrical models are used to determine the electrical characteristics of a PV cell from which one can determine the power and energy output of the PV system. It is the final step in PV system modeling and requires basic knowledge of semiconductor physics. In this chapter, two most commonly used electrical models of solar cells, namely Single Diode Model (SDM) (by De Soto) and Point Value Model (PVM) have been compared [19, 24]. The major difference between these two class of models is that single diode models estimate the full I-V curve whereas the point value model estimates only certain points on the I-V curve, such as open circuit voltage (V_{oc}), short circuit current (I_{sc}) and maximum power point (P_{mpp}).

5.1.1. Point Value Model (PVM)

Point value model, also known as simple efficiency model, predicts specific points on the I-V curve, depending upon the change in the incident irradiance and module temperature. It is one of the simplest electrical models to predict power output of a PV module and can be easily implemented using the information provided on module's datasheet. The model calculates the operating efficiency of the module using eqn. 5.1.

$$\eta(T_M, G_M) = \eta(25°C, G_M)\left[1 + k(T_M - 25°C)\right] \tag{5.1}$$

where $\eta(25°C, G_M)$ is the efficiency of the module at the given irradiance and 25 °C.
and

$$\kappa = \frac{\partial \eta}{\partial T}\frac{1}{\eta(STC)}$$

Typical values for κ (temperature coefficient of P_{mpp}) are -0.0025/ °C for CdTe, -0.0030/ °C for CIGS, and -0.0035/ °C for c-Si [53]. The detailed steps to obtain the efficiency at any irradiance or module temperature are provided in the reference [19]. The power output ($P_{DC,M}$) of the module at maximum power point can be determined by eqn. 5.2, using the area of the module (A_M).

$$P_{DC,M} = \eta(G_M, T_M) \cdot G_M \cdot A_M \tag{5.2}$$

Cell temperature and module efficiency

Figure 5.2 shows the effect of increasing irradiance on module efficiency. It is visible that the module efficiency decreases with increasing incident irradiance. Incident irradiance directly affects the cell temperature (T_{cell}), whereas module efficiency has an inverse relation with T_{cell}. When the temperature of cell increases, the band gap of the intrinsic semiconductor material decreases. This reduces its open circuit voltage (V_{oc}). Though a decrease in band gap also leads to an increase in the short circuit current (I_{sc}), due to increased absorption of light, the drop in V_{oc} is more dominant than the increase in I_{sc}.
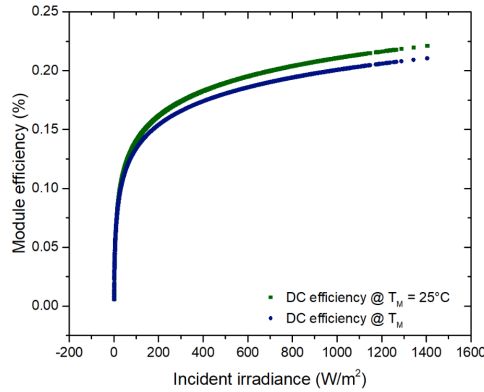
Figure 5.2: Comparison of $\eta(25°C, G_{POA})$ and $\eta(T_M, G_{POA})$ module efficiency in dependence of the incident irradiance.

5.1.2. Single Diode Models (SDM)

Single diode models are based on the equivalent circuit of a solar cell as shown in figure 5.4. The current through the load (I_L) can be expressed by eqn. 5.3

$$I_L = I_{ph} - I_o \left(e^{q(V_L + I.N_S.R_S)/nkN_S T_M} - 1\right) - \frac{V_L + I.N_S.R_S}{N_S.R_{sh}} \tag{5.3}$$

Where q is the electronic charge ($1.602 \cdot 10^{-19}C$), k is Boltzmann's constant ($1.380 \cdot 10^{-23}JK^{-1}$), I_o is the diode's reverse saturation current, T_M is the cell/module temperature, R_s is series resistance, R_{sh} is shunt resistance, n is diode ideality factor and N_s is the number of cells in series.
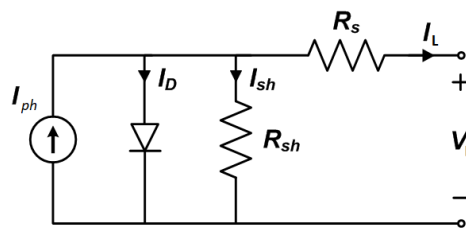
Figure 5.3: Single diode equivalent circuit of a solar cell.

It should be noted that eqn. 5.3 is a generic equation for solar cells as well as modules. For modules, it assumes that the cells are well matched and hence the voltage across a cell is approximately module voltage divided by the number of cells in series. Also, the equivalent circuit (see fig. 5.4) can be used to define the I-V curve of an individual cell, a module consisting of several cells or even an array composed of several modules[22]. The power output of the module is given by the product of voltage across the load (V_L) and current through it (I_L).

I_{ph}, I_o, R_s, R_{sh} and R_{sh} are primary parameters to all single diode equivalent circuit models. Single diode models are difficult to implement as these primary parameters are not readily available on the

module's datasheet and need to be derived using measured I-V curves. In the past, several modified versions of SDM have been developed such as De Soto's five parameter model, California Energy Commission's (CEC) 6 parameter model, etc. [24, 54]. These models differ from each other based on the auxiliary equations proposed to describe how the primary parameters [1] of the single diode equation are affected by cell temperature and irradiance.

In this thesis, De Soto's model has been used to evaluate the performance of SDM. In this model, the five primary parameters are obtained using auxiliary equations whose details can be found in the reference [24]. Further, this model requires few parameters which are not readily available in the module's datasheet. For the modules used in e-bike station, they were obtained from CEC's database [55].

5.2. Energy Yield

Energy yield (kWh) is defined as the power generated by a PV system over a fixed period. The DC side energy yield (E_{DC}) is given by eqn. 5.4.

$$E_{DC} = A_{tot} \int_{timeperiod} P_{DC,M} dt \qquad (5.4)$$

where A_{tot} is the total area of the PV modules and $timeperiod$ is the period over which energy yield is to be calculated. Generally, daily, monthly and yearly yields are calculated for monitoring and designing purposes.

5.3. Model comparison

Scope of electrical models

The electrical models discussed in sections 5.1.1 and 5.1.2 are used to estimate the power and energy generated by the solar modules installed at the e-bike station. Initially, to evaluate the performance difference between the models, G_{POA} and T_m measured at the e-bike station are used. It is assumed that, at any instant of time, the irradiance received by the modules is equal to that measured by the weather station installed at the e-bike station. Since the weather station is installed at one corner of the e-bike station it might happen that it is shaded and some modules might be receiving irradiance but given the small area of the e-bike station, this will happen only for a few minutes and won't have much effect on the power prediction. Further, the effect of partial shading is not considered and this might add up to some of the error in the power estimation.

Also, as already mentioned in section 4.3.1, it is assumed that the temperature of the cells is equal to the module temperature. Further, while modeling power output, it is assumed that all modules are at the same temperature. This is a valid assumption as all the modules are subjected to similar weather conditions (T_{amb}, W_s and G_{POA}) except during partial shading conditions which occur only for a few minutes during the whole day. The resolution of weather data is one minute and while calculating the energy output of the PV modules, it is assumed that the power predicted at a given time step, remains constant for the next one minute. This assumption might add some error to the energy calculations as the data recorded by weather station and DC side of the panels are not time synchronized.

Additional losses

While calculating the power generated by a PV system, it is also important to take into consideration additional losses due to the resistance of cables, interconnections, module mismatch and soiling. Typically, to account for all these losses, the system performance is de-rated by 3% [19]. Additionally, one should also take care of losses due to the MPPT module which is around 1% of the total output. In this thesis, while calculating the power generated by the modules, a de-rating factor of 2.5% was

---

[1] I_{ph}, I_o, R_s, R_{sh} and R_{sh} are the primary parameters which are common to all single diode equivalent circuit models

considered to account for additional losses due to module mismatch and soiling. Ohmic losses were calculated using eqn. 5.5.

$$P_{cable} = I^2 R_{cable} \tag{5.5}$$

where R_{cable} is the resistance of the cables used. In the e-bike station, $6mm^2$ "PV1-F" cables are used and they have a resistance of $0.00339\ \Omega/m$ at $20\ °C$ [56]. The total length of the cables is approximately $8m$ per module.

Module connections

The e-bike station is installed with 8 PV modules which are connected to each other as shown in the schematic 5.4. The modules on the top and bottom in each column are connected in series, thus forming four strings of modules. These are connected in parallel. The configuration was chosen to minimize the shading losses due to the shadow of the EEMCS building.
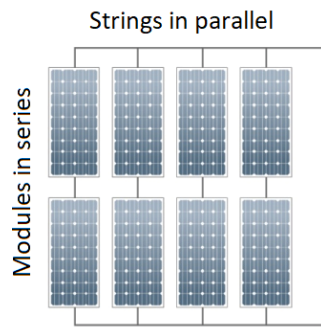
Figure 5.4: Schematic of module connections.

5.3.1. Evaluation of electrical models

In this section, the performance of the two electrical models, namely Point Value Model (PVM) and Single Diode Model by De Soto (SDM), are evaluated. Table 5.1 summarizes the datasets used in this section to evaluate the models. Two different types of statistical parameters, Root Mean Square Difference (RMSD) and percentage Relative Difference (%RD), were used to compare the performance of the models.

Table 5.1: Summary of database used in this chapter.

Datasetname	Source	Period	Variables used	Purpose
e-bike data	E-bike station, Delft, Nl	March-May '17	$T_{amb}, T_m,$ W_s, G_{POA}	Used to compare accuracy thermal and power models
Cabauw data	CESAR, Nl	April '17	$T_{amb}, W_s,$ $GHI, DNI,$ DHI	Evaluating effect of using data from nearby meteorological station
Cabauw data	CESAR, Nl	Oct'16-May'17, 2013	$T_{amb}, W_s,$ $GHI, DNI,$ DHI	To compare the models used to design the e-bike station with the improved models suggested in this thesis

To compare the accuracy of the models, measured module temperature (T_M) and incident irradiance (G_{POA}) at the e-bike station were used as inputs to the electrical models. The predicted values were compared with the actual generated power. E-bike data from March-May 2017 was used for this part of the study and more information about the dataset is available in section 4.3.1.
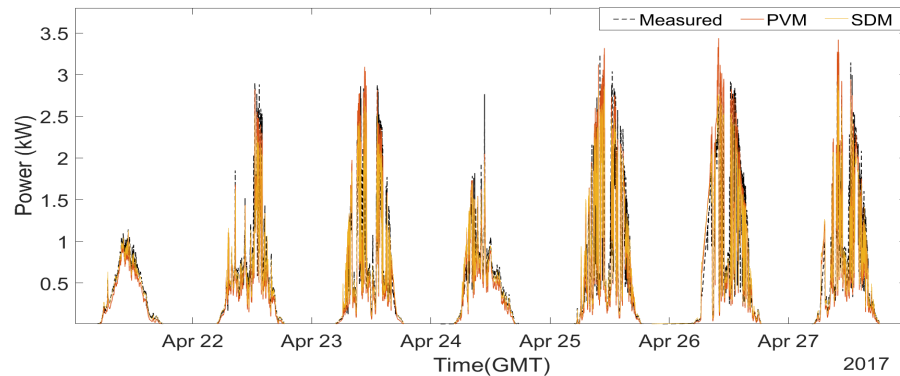
Figure 5.5: Instantaneous power prediction at the e-bike charging station.

Figure 5.5 shows the power predicted by the two models as compared to the measured value for one week in April 17. It can be seen that, both the models mostly over-predict the power produced by the models. To get a complete picture of the performance of the models, %RD was obtained for each of the models. Figure 5.6a shows the cumulative % relative difference between modeled and measured power for the two models, where the total number of samples were 69,759. In the bar chart, each bar shows the percentage of the total number of samples which are in different ranges of %RD for the corresponding model. The bottom most box (dark green) in each bar shows % of total samples less than 10% RD (also indicated by number) whereas the topmost box (red) shows the % of samples having %RD greater than 80%. A model performs the best if it has the highest percentage of samples in the bottom most box and least percentage of samples in the topmost box of the bar graph. Results of cumulative %RD for electrical models imply that a much higher fraction (48.8% of total samples) of the results have an %RD less than 10% for SDM as compared to PVM (21%). The results agree with the reported performance of the two models in literature [27].
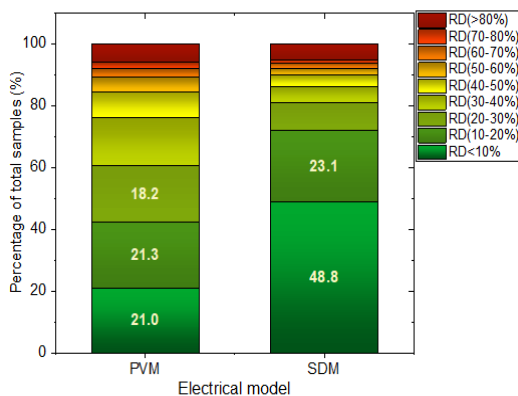
(a) Cumulative %RD .
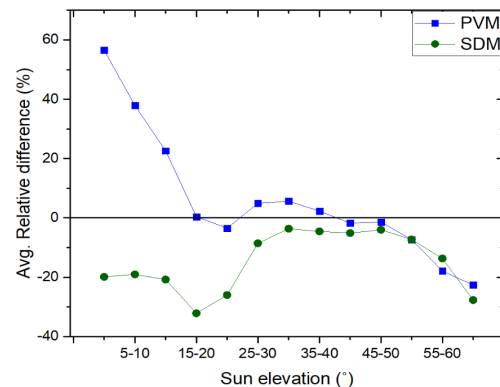
(b) Average %RD vs the solar elevation.

Figure 5.6: Comparison of % relative difference results for the two electrical models (based on e-bike data March-May'17).

The results (5.6a) also indicate that despite using T_m and G_{POA} measured at the e-bike station, more than 25% of results (for SDM) have % relative difference greater than 20%. It could be because of multiple reasons, like not accounting for the effect of partial shading, the variation of other module

losses (as a function of power produced) and low sensitivity of pyranometer when the sun is near the horizon [57]. Figure 5.6a shows the plot of average %RD against the sun elevation and it is visible that both the models have the highest average %RD for elevation angles below 15° and above 50°. The average %RD is large at low sun elevation angles due to the low sensitivity of the pyranometer. On the other hand, for elevation greater than 50°, the modules on the e-bike station are shaded by the EEMCS building and since the effect of partial shading is not accounted for, the average %RD becomes high.

Discussion

Comparing the results of cumulative %RD, it is clear that the SDM performs better than the PVM. The reason behind the underperformance of PVM is that it is highly dependent on the thermal coefficients provided on the module's datasheet and does not takes care of factors like module's ideality factor, its series and shunt resistance values and their variation with T_m and G_{POA}. On the other hand, SDM does not have this drawback as it uses experimentally derived module parameter and thus predicts power output more accurately. Figure 5.7 shows the scatter plot of modeled and measured module efficiency with increasing incident irradiance. Since PVM uses a negative thermal coefficient (κ) to calculate the operating efficiency, it predicts efficiency close to zero for lower irradiance values. It can be observed that the values predicted by SDM have the most overlap with measured efficiencies but it is still not able to cover the low values of efficiency.
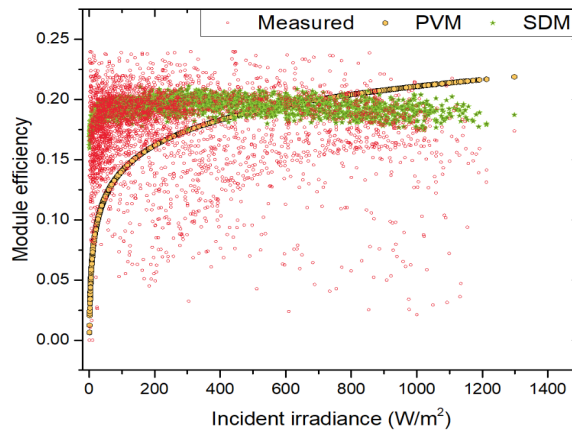
Figure 5.7: Comparison of modeled and measured η (T_m, G_{POA}) for increasing incident irradiance (based on e-bike data March-May '17).

Energy yield comparison

The energy yield for the whole duration of the study was calculated using eqn. 5.4. The difference between predicted and measured energy on a daily basis is shown in figure 5.8a. It can be seen that, the difference in the prediction of daily energy yield is less than 0.20 kWH/m^2 for PVM and 0.15 kWH/m^2 for SDM. The average daily difference for PVM is 0.037 kWH/m^2 and 0.027 kWH/m^2 for SDM. Further, it can be said that both the models tend to overestimate the energy produced.

Figure 5.8b shows a comparison of the monthly energy yield predicted and measured. Both the models predict the energy yield in a close approximation of the measured values. It is important to point out that the error in yield prediction decreases on a monthly basis because the underestimated and overestimated values balance out each other during the integration step involved in yield calculation.

Effect of using modeled input data

In contrast to monitoring a PV system where measured G_{POA} and T_m could be available, while designing a PV system irradiance and thermal models are needed to obtain G_{POA} and T_m using weather data from a nearby meteorological station.

(a) Comparison of difference between energy predicted and measured.

(b) Monthly energy predicted and measured.
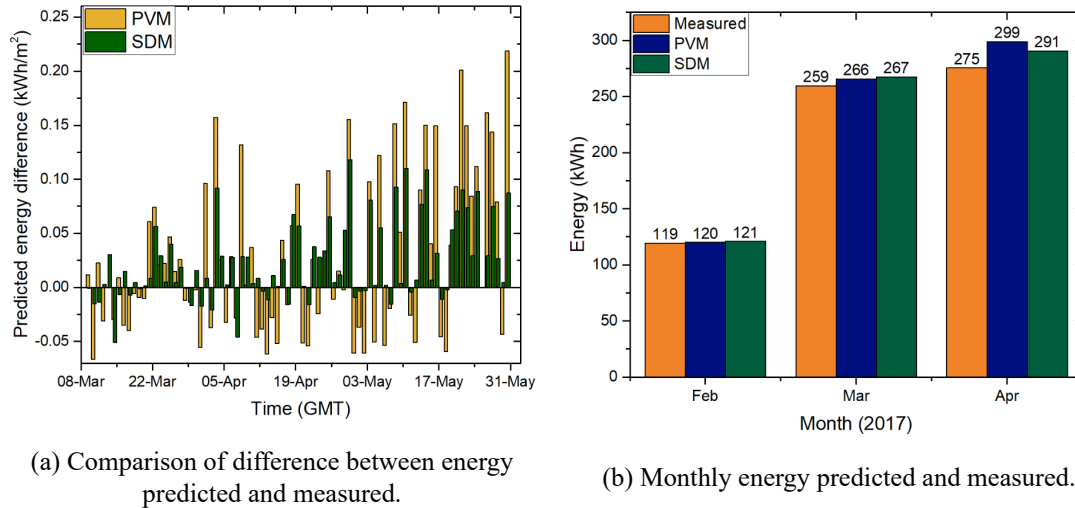
Figure 5.8: Energy yield (based on e-bike data March-May '17).
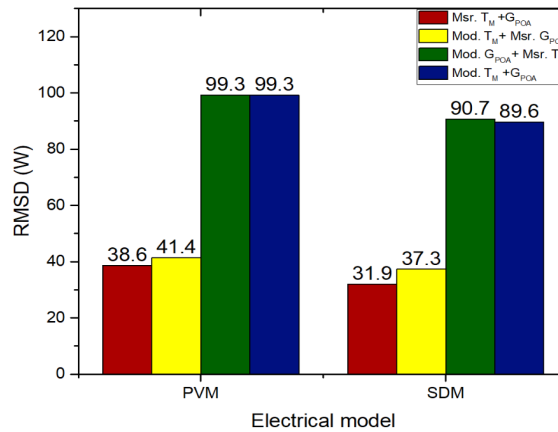
Figure 5.9: Root mean squared differences between modeled versus measured power when using data from nearby weather station. (based on Cabauw and e-bike data Apr. '17).

To evaluate the effect of using modeled G_{POA} and T_m on the performance of the electrical model, simulations were run using Cabauw data for the month of April-17. G_{POA} was modeled using Reindl model (refer chapter 3) and T_m was modeled using FD-TR (see chapter 4). Figure 5.9 shows the bar chart of RMSD for four different cases : first, when both G_{POA} and T_m are measured at the e-bike station (Msr. $T_m + G_{POA}$), second, when G_{POA} is measured whereas and T_m is modeled (Mod. $T_m +$ Msr. G_{POA}), third, when only irradiance is modeled using Cabauw data (Mod. $G_{POA} +$ Msr. T_m) and finally when both G_{POA} and T_m are modeled (Mod. $T_m + G_{POA}$). It can be observed from the results that, using modeled irradiance, the RMSD increases by around 60 W for both the models. The use of modeled T_m does not have a significant effect. Thus, the performance of electrical models is seriously affected by the quality of incident irradiance data available.

5.3.2. Comparison of design methodologies

In this section, the methodology used by G.G. Nair to design the e-bike station will be compared with the findings of this thesis. The e-bike station was designed using Isotropic (Irradiance model), DuffieB (Thermal model) and PVM (electrical model) models based on Cabauw data for the year 2013 [1]. The shading analysis was done with the help of Meteonorm-Horicatcher and factors like location-specific

SVF and albedo were not considered. However, in this thesis, it was found that Reindl, FD-TR and SDM are the best performing irradiance, thermal and electrical models respectively. Further, the performance of the irradiance models improves when shading factor and SVF calculated using Sketchup and elevation dependent albedo is incorporated. Cabauw data (Oct'16-Apr'17) was used as an input to both the methods. The results were verified using the e-bike data.
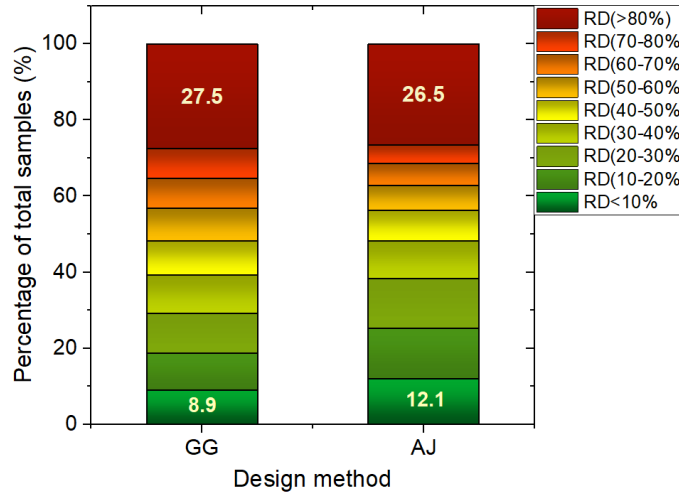
Figure 5.10: Comparison of cumulative %RD for each of the two methods (based on Cabauw and e-bike data Oct'16-Apr'17). The bottom most box (dark green) in each bar shows % of total samples less than 10% RD whereas the topmost box (red) shows the % of samples having %RD greater than 80%.

Table 5.2: Root mean squared and mean bias differences between modeled versus measured for the two methodologies (based on Cabauw and e-bike data Oct'16-Apr'17).

Methodology	RMSD	
	Power (W)	Energy (kWh)
GG Nair (GG)	577.56	34.65
This thesis (AJ)	430.16	25.81

Figure 5.10 and table 5.2 show the comparison of cumulative %RD and RMSD for the two methodologies. 'GG' refers to the results when models used by Nair were implemented for predicting the power produced at the e-bike station. 'AJ' refers to the case when the best models and modifications suggested in this thesis were used. It is seen that results improved significantly when the methodology proposed in this thesis was used. The number of samples having %RD less than 10% increased by 3.2% and those having %RD greater than 80% decreased by 1%. 61,173 samples were compared. Similar improvements were also seen in RMSD results for both power and energy modeling. The RMSD in power prediction decreased by more than 145 W whereas that for energy by almost 9 kWh. The total energy yield measured for the duration of Oct'16-Apr'17 was 418.13 kWh (excluding missing data), whereas GG and AJ predicted it to be 373.88 kWh and 432.83 kWh respectively. Both the models underestimate the total energy produced, but clearly, yield predicted by AJ is closer to the actual value as compared to GG.

A comparison of monthly DC energy yield predicted by the two methods (GG and AJ), based on Cabauw data for the year 2013, is shown in figure 5.11. The total energy produced by each module was 226 kWh/yr and 290 kWh/yr respectively. Since the actual yield would be slightly higher than

that predicted by AJ, it is safe to assume that the energy produced per module would be around 300 kWh/yr.

A quick calculation shows that, for the complete year, GG underestimates the energy yield by 511 kWh (64 kWh per module) than AJ. This means that the design of the PV system for the e-bike station was based on an underestimated value of the energy yield. Though, in the case of the e-bike station, this difference in yield does not require redesigning the whole system, for a larger system such errors could lead to an oversized design. For instance, if the system to be designed had more than 100 panels, the method of GG would underestimate the total energy yield by more than 6400 kWh/yr which might lead to installation of more than 20 extra solar panels (6400 kWh/yr/300 kWh/yr) to cover the energy demand. Note that the calculation of the number of panels, required to cover the energy loss, is based on the assumption that the actual energy produced by each module is slightly higher than that predicted by AJ's method. It will not only affect the cost of the system but also the required area. Using a more accurate designing methodology, as one suggested in this thesis, one can significantly save on space as well as capital costs.
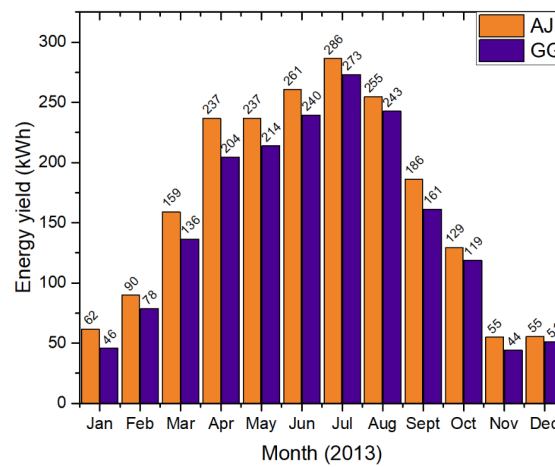
Figure 5.11: Energy predicted using the two methods (based on Cabauw data 2013).

5.4. Conclusions

Electrical models are critical to determining the module efficiency and its power output under operating conditions. In this chapter, the most commonly used electrical models, namely single diode model and point value model, for predicting the DC side power output of a PV module were evaluated.

The following research questions were addressed :

How accurate are the existing electrical models?

It was found that SDM is much more accurate than PVM as it computes the effect of T_m and G_{POA} on the complete I-V curve and it is not just based on thermal coefficients. For the studied period, around 75% of the results predicted by SDM and 41% by PVM had %RD less than 20%. Further, daily energy yield prediction was compared, and on an average, the difference between predicted and measured yield was 0.027 kWh/m^2 for SDM and 0.037 kWh/m^2 for PVM. As the system is grid-connected, the prediction error is almost insignificant.

How much effect do the inaccuracies in irradiance and thermal models have on the performance of electrical models?

The effect of using thermal and irradiance models on instantaneous power prediction was studied using Cabauw data (April-17). Statistical results showed that the RMSD increased by more than 60 W, mainly due to inaccuracies in G_{POA} prediction.

Using the method of the designer of the e-bike station, how well does the energy yield predicted match with the measured data after installation?

When the methodology used to design the e-bike station (designed by G.G Nair [1]) was implemented to predict the power and energy yield at the e-bike station, results showed that it has an RMSD of 577 W and only 8.9% of percent of total samples used, had an %RD less than 10%. Also, this method was found to underestimate the energy produced by the e-bike station by almost 76 kWh (based on Cabauw and e-bike data from Oct'16-Apr'17).

Do the improvements suggested in this thesis, improve the quality of prediction of energy yield?

The methodology proposed in this thesis improves the performance of energy yield prediction. The energy yield predicted was only 17 kWh less than the measured value (based on Cabauw and e-bike data from Oct'16-Apr'17). As compared to Nair's methodology, the RMSD in power prediction decreased by more than 140 W and by almost 9 kWh for energy prediction. Also, the number of samples having %RD less than 10% increased by more than 3.2%.

In general, it was observed that SDM model is best suited for modeling the PV modules installed on the e-bike station. The only disadvantage with SDM is that it requires knowledge of experimentally derived parameters which are usually not provided by the module manufacturer. PVM is a good alternative to develop a simple electrical model of the PV module using the information available on the module's datasheet. Further, the improvements suggested in this thesis significantly improve the energy yield prediction as compared to the models used by the designer of the e-bike station.

6

Conclusions and Recommendations

6.1. Conclusions

The motivation of this thesis is to study different irradiance, thermal and electrical models used to model a PV system and suggest methods to improve their performance. The models are evaluated using meteorological data from Cabauw and data measured at the e-bike charging station. The following research questions were formulated and resolved in this thesis.

1. For the climate of the Netherlands, study and improve decomposition models

    (a) *Which is the most accurate decomposition model ?*
    It was found that amongst the existing decomposition models, RE-2 and OH perform the best for the climatic conditions of the Netherlands.

    (b) *What are the drawbacks of existing decomposition models and how can they be improved?*
    The best performing existing models are developed using hourly irradiance data and they ignore the fluctuating nature of solar radiation. Nowadays, irradiance data having a temporal resolution as low as a minute is available and it should be used to update the coefficients of existing models.

    (c) *Is it possible to improve the performance of decomposition models using local irradiance data?*
    Two new decomposition models, Dutch-I and Dutch-II, were developed using minute data from Cabauw, NL and were found to be more accurate than the existing ones. Therefore, it can be concluded that the performance of existing models can be improved by using location-specific irradiance data to derive the coefficients of the piecewise correlations.

2. Evaluate and optimize transposition models to compute the irradiance on the plane of array of the e-bike station

    (a) *Which are the most accurate transposition models to be used in urban location?*
    It was found that Reindl and Hay/Davies models are most suited for the climate of Netherlands.

    (b) *How important is shading analysis to irradiance modeling and what is the most reliable technique to incorporate it?*
    For the location of the e-bike station, shading analysis can reduce RMSD in irradiance prediction by almost $50\ W/m^2$ (i.e almost 5% of incident power during noon) for all the models. Two different methods of shading analysis : Meteonorm-Horicatcher and 3-D modeling were compared. It was found that using Sketchup is the most accurate way to do shading analysis.

(c) *How can the performance of existing models be improved by using location-specific pa-rameters like sky view factor and albedo?*

Using both location-specific SVF and elevation dependent albedo significantly improved the prediction of G_{POA}. The number of samples having %RD below 10% increased by al-most 1% and those having %RD greater than 80% decreased by almost 7% for the all the models. It is a significant percentage as the number of samples compared were 56,243.

(d) *What is the effect of using decomposition models instead of measured diffuse and direct irradiance?*

When a combination of decomposition and transposition models was used, they produced almost equivalent results as compared to the use of just transposition models.

3. Evaluate thermal models best suited for predicting module temperature of a closed system like the e-bike station

(a) *Which is the best performing thermal model?*

FD-TR is best suited for predicting the module temperature at the e-bike station. It has the an RMSD of $1.91°C$ and an MBD of $-0.71°C$. Also, almost 69% of values predicted were having %RD less than 10%.

(b) *Does the time step between the data used for modeling have an impact on the performance of the models?*

The models are not affected by the time-step of the data used except for the FD-SS model. Even for the FD-SS model, the performance with minute data is poor only for higher values of incident irradiance. The overall performance of FD-SS increases significantly when the time step between samples is increased to an hour instead of a minute.

(c) *What is the effect of using weather data from nearby meteorological stations on the perfor-mance of thermal models?*

Use of modeled G_{POA} and W_S introduces higher errors in the prediction of module tem-perature as compared to the case when measured G_{POA} and W_S are used, but the errors are within the acceptable range. It was also observed that most of the error gets introduced due to inaccuracies in the transposition model and not by the thermal model itself.

4. Compare existing solar cell electrical models to compute the DC power and energy output of the e-bike charging station

(a) *How accurate are the existing electrical models?*

It was found that the single diode model by De Soto is much more accurate than point value model. For the duration of Mar-May'17, around 75% of the results predicted by SDM and 41% by PVM had %RD less than 20%.

(b) *How much effect do the inaccuracies in irradiance and thermal models have on the perfor-mance of electrical models?*

The effect of using thermal and irradiance models on instantaneous power prediction was studied using Cabauw data (April'17). Statistical results showed that the RMSD increased by more than $60\ W$ mainly due to inaccuracies in G_{POA} prediction.

(c) *Using the method of the designer of the e-bike station, how well does the energy yield predicted match with the measured data after installation?*

When the methodology used to design the e-bike station (designed by G.G Nair [1]) was implemented to predict the power and energy yield at the e-bike station, results showed that it has an RMSD of 577 W and only 8.9% of percent of total samples used were having an %RD less than 10%. Also, this method was found to underestimate the energy produced

by the e-bike station by almost 76 kWh (based on Cabauw and e-bike data from Oct'16-Apr'17).

(d) *Do the improvements suggested in this thesis, improve the quality of prediction of energy yield?*

The methodology proposed in this thesis improves the performance of energy yield prediction. The energy yield predicted was only 17 kWh less than the measured value (based on Cabauw and e-bike data from Oct'16-Apr'17). As compared to Nair's methodology, the RMSD in power prediction decreased by more than 145 W and by almost 9 kWh for energy prediction. Also, the number of samples having %RD less than 10% increased by more than 3.2%.

Finally, it can be concluded the findings of this thesis will help to predict the power and energy yield of e-bike station more accurately.

6.2. Recommendations

Though this report is comprehensive, the author had to restrict himself to meet various goals in a limited time. However, some more improvements could be considered to improve the performance of an irradiance, thermal and electrical models of the PV system.

6.2.1. Irradiance modeling

Decomposition models

The performance of decomposition models could be further improved by evaluating the dependence of the diffuse fraction on factors like air mass, cloud cover etc. Cloud imagery obtained from satellites could be processed to get more details about the cloud cover and hence, can be used to predict diffuse irradiance. Also, advanced programming techniques like neural networks could be used to improve the performance of decomposition models.

Transposition models

The transposition models are the most important part of PV system modeling and there is a lot of scope to improve their performance, especially the sky diffuse and ground reflected component. The new irradiance model based on ray tracing showed promising results and showed that the reflected irradiance from nearby structures can also be taken into consideration. However, this model underperforms during partly cloudy conditions and a combination of best performing standard transposition model and the ray tracing method could be used based on the clearness index of the day.

Shading analysis

While doing the shading analysis in this project, the effect of only big structures like EEMCS and CEG building was taken into consideration. It could be improved by considering effect of trees and other small structure. Further, methods, like the use of LIDAR data, could be implemented along with Sketchup to incorporate the effect of the far-off objects on the horizon of the e-bike station.

6.2.2. Thermal modeling

The thermal model could be further improved by evaluating the temperature of each module separately and creating a detailed structure of the e-bike station. Also, the losses due to conduction could be taken into account.

6.2.3. Electrical modeling

The performance of electrical models could be further improved by considering partial shading on the modules.

A

Irradiance models

Table A.1: List of symbols used to describe decomposition and transposition models

Nomenclature

GHI	global horizontal irradiance (W/m^2)	T_a	outdoor air temperature $(°C)$
DHI	diffuse horizontal irradiance (W/m^2)	ϕ	relative humidity (%)
DNI	direct normal irradiance on a horizontal surface (W/m^2)	G_t	monthly average global irradiance on a horizontal surface (W/m^2)
E_{sc}	extraterrestrial solar irradiance (W/m^2)	AM	air mass at actual pressure (dimensionless)
G_{POA}	total solar irradiance on plane of array (W/m^2)	A_s	solar azimuth angle (°)
G_{dir}	total direct irradiance on a tilted surface (W/m^2)	A_m	module azimuth angle (°)
G_{ground}	total ground reflected irradiance on a tilted surface (W/m^2)	α	sun altitude (°)
G_{dif}	total diffused irradiance on a tilted surface (W/m^2)	β_m	module tilt angle with horizontal surface (°)
$G_{dif,Hb}$	horizon-brightening component of G_{dif} (W/m^2)	θ_z	solar zenith angle
$G_{dif,Iso}$	isotropic component of G_{dif} (W/m^2)	θ_i	air mass at standard pressure (1013.25 mbar) (dimensionless)
$G_{dif,Cs}$	circumsolar component of G_{dif} (W/m^2)	AM_r	
E_a	extraterrestrial solar constant irradiance (1367 W/m^2)	p	the local air-pressure (mbar)
k_t	clearness index (dimensionless)	N	day number in the year (No.)
k_d	diffuse fraction (dimensionless)	n	number of data
A_i	anisotropic index (dimensionless)		

A.1. Irradiance modeling

A.1.1. Decomposition models

In all the models, once diffused fraction (k_d) is determined from the piecewise correlations, the diffused irradiance (DHI) is then obtained by eqn. A.1.

$$DHI = k_d \times GHI \tag{A.1}$$

And the direct irradiance (DNI) is obtained from eqn. A.2.

$$DNI = \frac{GHI - DHI}{\cos(\theta_z)} \tag{A.2}$$

Orgill and Holands model (OH)

Orgill and Hollands (1977) adapted the Liu and Jordan model for hourly clearness index k_t and diffused fraction k_d using 4 years of irradiance data from Toronto, Canada [10]. They divided the data set into three ranges based on the value of k_t to represent clear, partly cloudy and complete overcast and found linear relations between k_d and k_t in those ranges as per eqns. A.3, A.4 and A.5.

$$\text{Interval: } k_t < 0.35 \quad k_d = 1 - 0.249 k_t \tag{A.3}$$

$$\text{Interval: } 0.35 \le k_t \le 0.75 \quad k_d = 1.577 - 1.84 k_t \tag{A.4}$$

$$\text{Interval: } k_t > 0.75; \quad k_d = 0.177 \tag{A.5}$$

Erbs model (ER)

Erbs et al. (1982) used higher order polynomial fit to find correlations between k_d and k_t but they used DNI and GHI data from 5 stations in USA [11]. DHI was obtained from DNI by rearranging eqn. A.2. The relations between k_t and k_d is as per eqns. A.6, refeqn:Ap-7 and A.8.

$$Interval : k_t \le 0.22; \quad k_d = 1 - 0.09 k_t \tag{A.6}$$

$$Interval : 0.22 < k_t \le 0.8 \quad k_d = 0.9511 - 0.1604 k_t + 4.39 k_t^2 - 16.64 k_t^3 + 12.34 k_t^4 \tag{A.7}$$

$$Interval : k_t > 0.8 \quad k_d = 0.165 \tag{A.8}$$

Reindl model (RE)

Reindl et al. (1990) found piecewise correlations between k_d and k_t based on GHI and DHI data obtained from 5 different locations in the USA and Europe [12]. They proposed three different relations. First relation uses only clearness index, second uses sun altitude(α) in addition to k_t, whereas the third one uses clearness index, sun altitude, outdoor air temperature (T_a) and the relative humidity (ϕ) of the location. These three models will be referred as Re-1, Re-2 and Re-3 respectively and are given by eqns. A.9-A.17.

RE-1

$$\text{Interval: } 0 < k_t \le 0.3 \quad k_d = 1.020 - 0.248 k_t \tag{A.9}$$

$$\text{Interval: } 0.3 < k_t \le 0.78 \quad k_d = 1.45 - 1.67 k_t \tag{A.10}$$

$$\text{Interval: } k_t > 0.78 \quad k_d = 0.147 k_t \tag{A.11}$$

RE-2

$$\text{Interval: } 0 < k_t \le 0.3 \quad k_d = 1.020 - 0.254k_t + 0.0123\sin\alpha \tag{A.12}$$

$$\text{Interval: } 0.3 < k_t \le 0.78 \quad k_d = 1.4 - 1.749k_t + 0.177\sin\alpha \tag{A.13}$$

$$\text{Interval: } k_t > 0.78 \quad k_d = 0.486k_t - 0.182\sin\alpha \tag{A.14}$$

RE-3

$$\text{Interval: } 0 < k_t \le 0.3 \quad k_d = 1.0 - 0.232k_t + 0.0239\sin\alpha - 0.000682T_a + 0.019\phi \tag{A.15}$$

$$\text{Interval: } 0.3 < k_t \le 0.78 \quad k_d = 1.329 - 1.716k_t + 0.267\sin\alpha - 0.00357T_a + 0.106\phi \tag{A.16}$$

$$\text{Interval: } k_t > 0.78 \quad k_d = 0.426k_t + 0.256\sin\alpha - 0.00349T_a + 0.0734\phi \tag{A.17}$$

Maxwell's Direct Insolation Simulation Code Model (DISC)

Maxwell developed a quasi-physical decomposition model to predict direct irradiance (DNI) from GHI. The model was developed using 1 year data from Atlanta, Georgia, USA and was validated using data from three different U.S. sites [13]. DISC differs from other models as it uses direct beam clearness index (K_n) and a clear sky Kn denoted by K_{nc} instead of diffused fraction(k_d) as a dependent variable. Eqns. A.18-A.26 explains the implementation of DISC model. DNI is calculated from extraterrestrial irradiance using eqn. A.18.

$$DNI = E_a K_n \tag{A.18}$$

Where

$$K_n = K_{nc}\Delta K_n \tag{A.19}$$

and

$$\Delta K_n = a + b\exp^{(C*AM)} \tag{A.20}$$

The clear sky limit K_{nc} is obtained from air mass AM using eqn. A.21.

$$K_{nc} = 0.8660.122AM + 0.0121AM^2 0.000653AM^3 + 0.000014AM^4 \tag{A.21}$$

where,

$$AM = AM_r\left(\frac{p}{1013.25}\right) \tag{A.22}$$

The air mass (AM), is obtained from the standard pressure AM_r using Kasten's formula as per eqn. A.23 [33].

$$AM_r = [\cos(\theta_z) + 0.15(93.885 - \theta_z)^{-1.253}]^{-1} \tag{A.23}$$

Further, the constants a, b and C re obtained from k_t from eqns.A.24-A.26 as given below.

$$\text{Interval: } k_t \le 0.6 \tag{A.24}$$

$$a = 0.512 - 1.56k_t + 2.286k_t^2 - 2.222k_t^3$$

$$b = 0.37 + 0.962k_t$$

$$c = -0.28 + 0.923k_t - 2.048k_t^2$$

$$\text{Interval : } k_t > 0.6 \tag{A.25}$$

$$a = -5.743 + 21.77k_t - 27.49k_t^2 + 11.56k$$

$$b = 41.4 - 118.5k_t + 66.05k_t^2 + 31.9k_t^3$$

$$c = -47.01 + 184.2k_t - 222k_t^2 + 73.81k_t^3 \tag{A.26}$$

A.1.2. Transposition model

Isotropic model

It is the simplest of all transposition models and assumes that the diffuse irradiance is uniformly distributed over the sky dome [15]. It calculates the diffused irradiance received by a tilted surface by eqn. A.27 . This model performs well for completely cloudy skies but as the sky becomes clearer its performance decreases.

$$G_{dif} = DHI \left(\frac{1 + \cos \beta_m}{2} \right) \tag{A.27}$$

Hay & Davies

The Hay and Davies (Hay/Davies) model takes into account circumsolar and isotropic diffused components. They defined an "anisotropy index" given by eqn. A.28 to give weightage to the circumsolar ($G_{dif,Cs}$) and isotropic components [14]. A part of the diffused irradiance is treated as circumsolar and is projected onto the tilted surface similar to beam radiation(see eqn. A.29).

$$A_i = \frac{DNI}{E_a} \tag{A.28}$$

$$G_{dif,Cs} = DNI.A_i.\cos(\theta_i) \tag{A.29}$$

The remaining diffused component is considered to be isotropic in nature and transposed using eqn. A.30. Equation A.31 gives the complete relation for the sky diffused component on module.

$$G_{dif,Iso} = A_i.DHI.\left(\frac{1 + \cos \beta_m}{2} \right) \tag{A.30}$$

$$G_{dif} = G_{dif,Cs} + G_{dif,Iso} \tag{A.31}$$

Hay/Davies models is suited for clear sky days when anisotropy index is high and circumsolar diffuse has a significant contribution to Gdif.

Reindl

Reindl et al. proposed a model to predict sky diffused component on tilted surface which takes care of all three components of the diffused irradiance [58]. It extends the work of Hay/davies and adds a term to calculate diffused component due to horizon brightening ($G_{dif,Hb}$) given by eqn. A.32. Equation A.33 gives the complete relation used by Reindl to calculate the G_{dif}.

$$G_{dif,Hb} = DHI.\left[(1 - A_i).\left(\frac{1 + \cos \beta_m}{2} \right).\sqrt{\frac{DHI}{GHI}} \sin^3 \left(\frac{\beta_m}{2} \right) \right] \tag{A.32}$$

$$G_{dif} = DHI.A_i.\cos(\theta_i) + DHI.(1 - A_i).\left(\frac{1 + \cos \beta_m}{2} \right).\left[1 + \sqrt{\frac{DHI}{GHI}} \sin^3 \left(\frac{\beta_m}{2} \right) \right] \tag{A.33}$$

Sandia Model

A new empirical model was developed by David King at Sandia national laboratories using measured irradiance data. It is given by eqn. A.34 , where the first term accounts for isotropic diffuse component and second term is an empirically derived correction term to account for the circumsolar and horizon brightening diffuse components.

$$G_{dif} = DHI\left(\frac{1 + \cos\beta_m}{2}\right) + GHI\left(\frac{(0.012\theta_z - 0.04) \times (1 - \cos(\beta_m))}{2}\right) \tag{A.34}$$

Additionally, Sandia model uses an empirical relation(eqn. A.35) to derive the albedo factor, which is used for calculating the ground reflected component.

$$\rho = 0.012 \times (\theta_z - 0.04) \tag{A.35}$$

Perez Model

It is the most complex transposition model which computes all the three sub-components of the sky diffuse irradiance [16, 17]. It uses empirically derived coefficients to determine the contribution of isotropic, circumsolar and horizon brightening components. The sky diffused component is given by equation A.36.

$$G_{dif} = DHI\left[(1 - F_1)\left(\frac{1 + \cos(\beta_m)}{2}\right) + F_1\frac{a}{b} + F_2\sin(\beta_m)\right] \tag{A.36}$$

Here, $F1$ and $F2$ are circumsolar and horizon brightness coefficients, respectively, and a and b are factors dependent on angle of incidence and tilt of the module. The terms a and b are computed using eqns. A.37 and A.38, respectively.

$$a = \max(0°, \cos\theta_i) \tag{A.37}$$

$$b = \max(\cos 85°, \cos\theta_z) \tag{A.38}$$

The coefficients $F1$ and $F2$ depend on two other sky condition parameters clearness $varepsilon$ and brightness Δ. These factors are defined in eqns. A.39 and A.40, respectively.

$$\varepsilon = \frac{\frac{DHI+DNI}{DHI} + 1.041\theta_z^3}{1 + 1.041\theta_z^3} \tag{A.39}$$

$$\Delta = m\frac{DHI}{E_a} \tag{A.40}$$

F1 and F2 are then computed in Eqs. A.41 and A.42, respectively.

$$F_1 = \max\left[0, \left(f_{11} + f_{12}\Delta + \frac{\pi\theta_z}{180}f_{13}\right)\right] \tag{A.41}$$

$$F_2 = f_{21} + f_{22}\Delta + \frac{\pi\theta_z}{180}f_{23} \tag{A.42}$$

The coefficients $f11$, $f12$, $f13$, $f21$, $f22$, and $f23$ were derived using statistical analysis of empirical data for specific locations. Two different sets of coefficients were derived for this model [17, 17].

B

Extra results

B.1. Decompostion models

Table B.1: Percentage of results with corresponding maximum % relative difference for decomposition models based on CESAR data.

Model	<10%	10-20%	20-30%	30-40%	40-50%	50-60%	60-70%	70-80%	>80%
2016									
OH	57.05	11.74	9.21	7.13	5.30	3.70	2.99	1.22	1.66
Er	56.77	13.77	8.93	6.30	4.93	3.88	3.10	1.29	1.01
Re-1	52.95	13.70	10.86	7.71	5.22	3.68	2.85	1.66	1.37
Re-2	56.22	11.72	8.76	6.59	4.93	3.82	2.65	1.55	3.77
Re-3	55.47	14.70	10.06	6.65	3.91	2.63	1.68	0.90	4.01
DISC	51.59	14.49	10.93	8.86	6.01	3.84	2.69	1.26	0.33
Dutch-I	59.66	10.60	7.89	6.37	4.89	3.22	2.19	1.19	4.01
Dutch-II	62.05	11.65	8.12	6.34	4.25	2.94	1.88	0.99	1.79
2014									
OH	58.47	12.45	9.33	6.84	5.29	3.77	2.40	1.07	0.38
Er	57.67	13.70	8.94	6.57	5.15	3.91	2.68	1.13	0.25
Re-1	54.09	14.86	10.38	7.34	5.32	3.54	2.80	1.48	0.20
Re-2	58.40	12.38	9.17	7.10	4.87	3.28	2.18	1.20	1.42
Re-3	56.06	14.73	10.16	7.08	4.28	2.65	1.51	0.78	2.75
DISC	50.38	13.29	10.29	8.91	7.18	4.84	3.40	1.46	0.25
Dutch-I	62.50	11.68	8.69	6.28	4.54	2.72	1.49	0.83	1.28
Dutch-II	63.93	11.71	8.59	6.11	4.29	2.68	1.31	0.62	0.76

Table B.2: Comparison of the models based on MBD, RMSD and CRSS for three years.

Model	MBD (W/m^2)			RMSD(W/m^2)			CRSS		
	2016	2015	2014	2016	2015	2014	2016	2015	2014
OH	-16.0	-17.0	-19.5	55.4	54.7	56.8	4182.3	4074.6	4270.4
Er	-18.7	-20.2	-22.4	58.3	57.9	60.3	4338.0	4273.1	4521.1
Re-1	-20.2	-21.4	-23.8	60.3	59.6	62.0	4767.9	4680.3	4927.5
Re-2	-6.2	-7.7	-10.1	50.9	50.2	50.4	3928.0	3749.1	3786.4
Re-3	0.1	-1.2	-4.7	65.7	65.8	63.0	4882.0	4802.8	4932.9
DISC	-24.6	-25.9	-29.0	57.4	58.1	61.8	5549.7	5712.9	6193.7
Dutch-I	1.9	0.7	-2.8	45.6	44.5	43.5	3253.8	3088.2	3132.5
Dutch-II	-2.4	-2.9	-6.6	44.3	45.5	46.4	3125.2	3072.3	3291.1

B.2. Transposition models
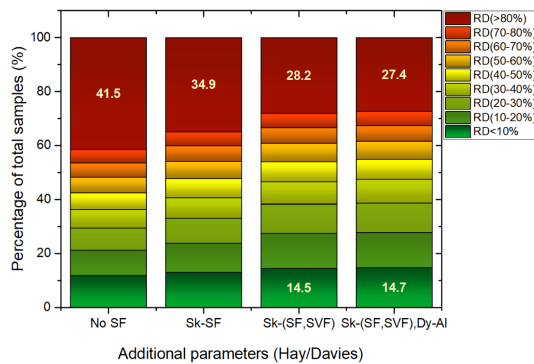
(a) Without any shading factor
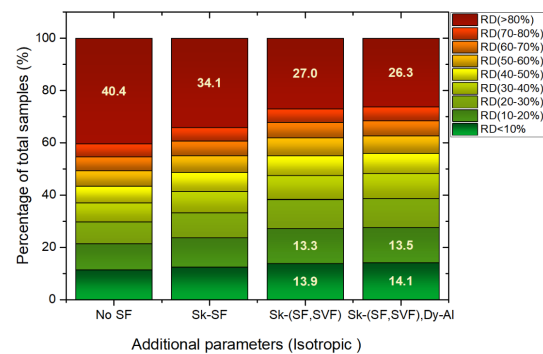
(b) After using shading factor from Sketchup

Figure B.1: Comparison of standard transposition models based on cumulative % relative difference (using e-bike data Oct.'16-Apr.'17). The bottom most box (dark green) in each bar shows % of total samples less than 10% RD whereas the topmost box (red) shows the % of samples having %RD greater than 80%. versus measured for each of the five transposition models (Oct,16- Apr,17).

C

Data descritpion

C.1. Detail about missing data

C.1.1. CESAR data

Decomposition models were evaluated using CESAR data from the year 2014-2016. Figures C.1 and C.2 below shows the number of hours of missing data in each month.
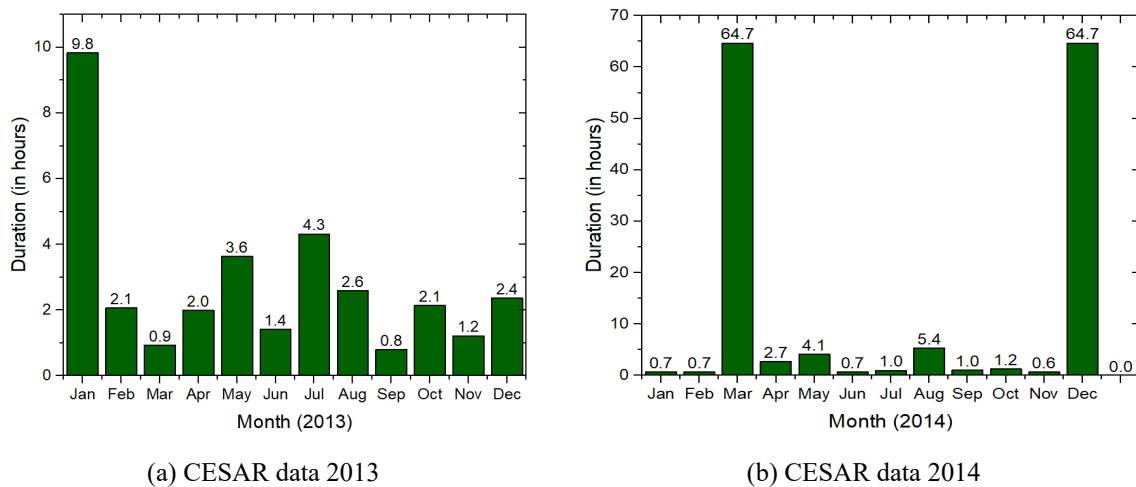
(a) CESAR data 2013

(b) CESAR data 2014

Figure C.1: Hours of missing data from CESAR database for year 2013 and 2014.

(a) CESAR data 2015
(b) CESAR data 2016
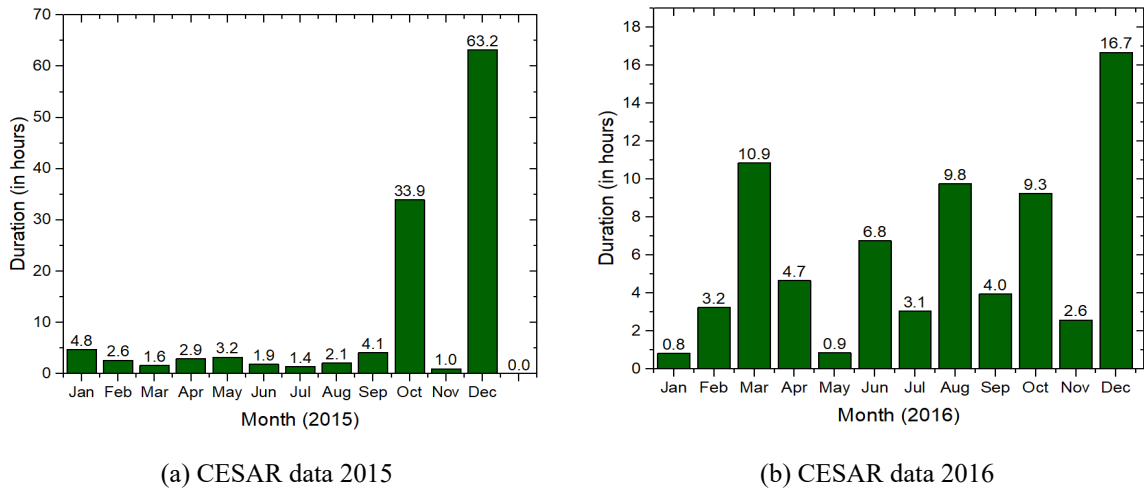
Figure C.2: Hours of missing data from CESAR database for year 2015 and 2016.

For the year 2017, CESAR data was available till April-17 except for the month of March. Figure C.3 shows the bar chart of number of hours of missing data per month for year 2017.
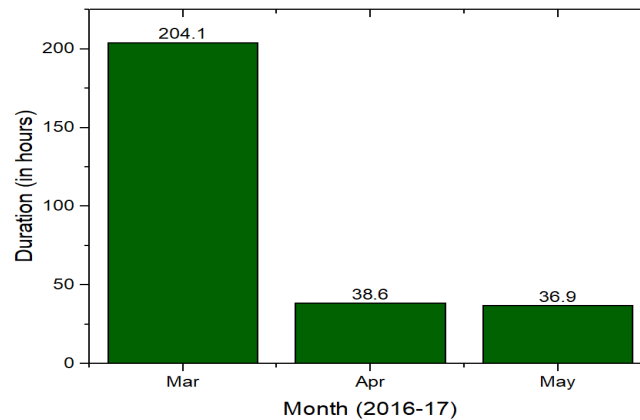
Figure C.3: Hours of missing data from CESAR database for year 2017.

Ebike data

E-bike data was used for validation of transposition, thermal and power models. For validating the transposition models data from Oct-16 to May-17 was used whereas for thermal and power models, data from Mar-17 to May-17 was used as module temperature data became available only after 8th-Mar-17. Figure C.4 and C.5 shows the plot of number hours of missing data per month for e-bike weather station and module temperature data respectively. It should be noted that while validating thermal and power models, it was made sure that only those samples were used were data for both weather station and module temperature was available.
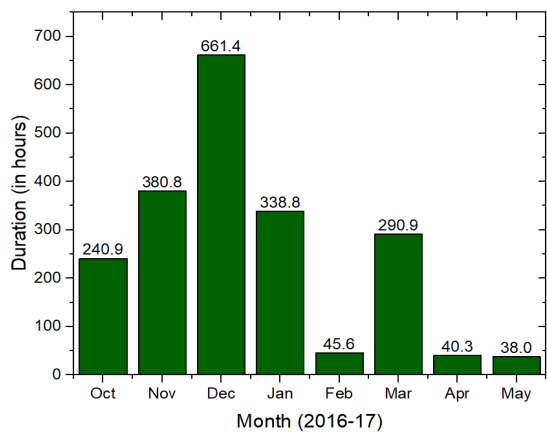
(a) Monthly distribution of missing data
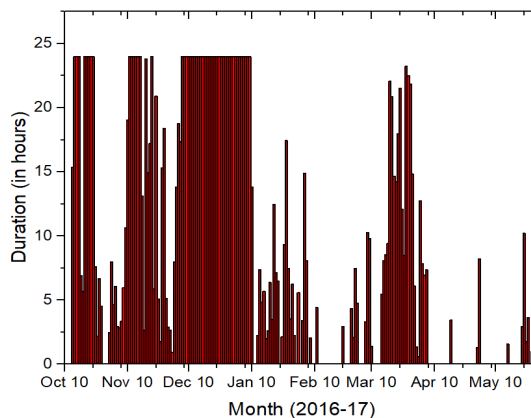
(b) Daily distribution of missing data

Figure C.4: Hours of missing data from E-bike weather station data for the period of Oct-16 to May-17
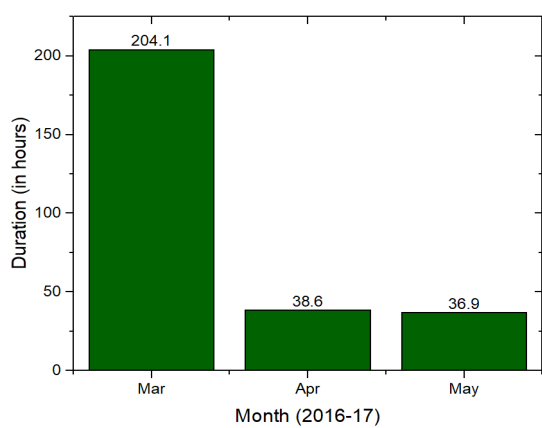
(a) CESAR data 2015
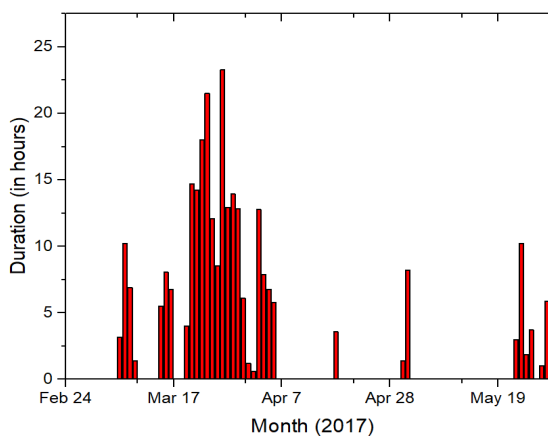
(b) CESAR data 2016

Figure C.5: Hours of missing data from CESAR database for year 2015 and 2016.

D

Wind speed scaling

Table D.1: Roughness Classes and Roughness Length Table [49]

Rough-ness Class	Roughness Length	Energy Index (%)	Landscape Type
0	0.0002	100	Water surface
0.5	0.0024	73	Completely open terrain with a smooth surface, e.g.concrete runways in airports, mowed grass, etc.
1	0.03	52	Open agricultural area without fences and hedgerows and very scattered buildings. Only softly rounded hills
1.5	0.055	45	Agricultural land with some houses and 8 metre tall sheltering hedgerows with a distance of approx. 1250 metres
2	0.1	39	Agricultural land with some houses and 8 metre tall sheltering hedgerows with a distance of approx. 500 metres
2.5	0.2	31	Agricultural land with many houses, shrubs and plants, or 8 metre tall sheltering hedgerows with a distance of approx. 250 metres
3	0.4	24	Villages, small towns, agricultural land with many or tall sheltering hedgerows, forests and very rough and uneven terrain
3.5	0.8	18	Larger cities with tall buildings
4	1.6	13	Very large cities with tall buildings and skycrapers

Module datasheet

• **20.3% efficiency**
Ideal for roofs where space is at a premium or where future expansion might be needed.

• **Maximum performance**
Designed to deliver the most energy in demanding real world conditions, in partial shade and hot rooftop temperatures.[1,2,3]

• **Premium aesthetics**
SunPower™ sleek black X-Series panels blend harmoniously into your roof. The most elegant choice for your home.
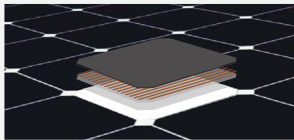
Maxeon™ Solar Cells: Fundamentally better.
Engineered for performance, designed for durability.

Engineered for peace of mind
Designed to deliver consistent, trouble-free energy over a very long lifetime.[4,5]

Designed for durability
The SunPower Maxeon Solar Cell is the only cell built on a solid copper foundation. Virtually impervious to the corrosion and cracking that degrade Conventional panels.[4,5]

Same excellent durability as E-Series panels. **#1 Ranked** in Fraunhofer durability test.[10] **100% power** maintained in Atlas 25+ comprehensive PVDI Durability test.[11]

UNMATCHED PERFORMANCE, RELIABILITY & AESTHETICS

X20 - 327 PANEL

X20 SERIES

HIGHEST EFFICIENCY[6]

Generate more energy per square meter

X-Series residential panels convert more sunlight to electricity producing 44% more power per panel,[1] and 75% more energy per square meter over 25 years.[3,4]

HIGHEST ENERGY PRODUCTION[7]

Produce more energy per rated watt

High year one performance delivers 8-10% more energy per rated watt.[3] This advantage increases over time, producing 21% more energy over the first 25 years to meet your needs.[4]
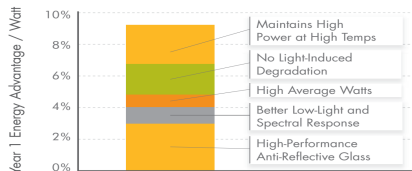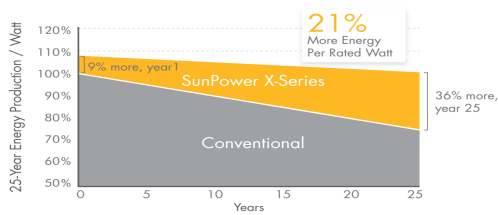
global.sunpowercorp.com

83

SUNPOWER
MORE ENERGY. FOR LIFE.

X-SERIES SOLAR PANELS

SUNPOWER OFFERS THE BEST COMBINED POWER AND PRODUCT WARRANTY

POWER WARRANTY
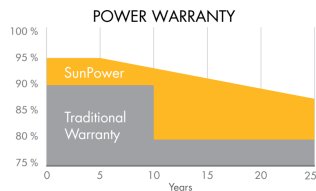
More guaranteed power: 95% for first 5 years,
-0.4%/yr. to year 25.[8]

PRODUCT WARRANTY
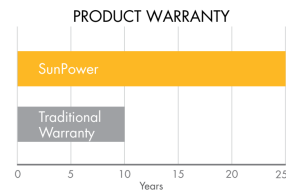
Combined Power and Product defect 25 year coverage
that includes panel replacement costs.[9]

ELECTRICAL DATA

	X20-327-BLK
Nominal Power[12] (Pnom)	327 W
Power Tolerance	+5/–0%
Avg. Panel Efficiency[13]	20.3%
Rated Voltage (Vmpp)	57.3 V
Rated Current (Impp)	5.71 A
Open-Circuit Voltage (Voc)	67.6 V
Short-Circuit Current (Isc)	6.07 A
Max. System Voltage	1000 V IEC & 600 V UL
Maximum Series Fuse	20 A
Power Temp Coef.	–0.30% / °C
Voltage Temp Coef.	–167.4 mV / °C
Current Temp Coef.	3.5 mA / °C

OPERATING CONDITION AND MECHANICAL DATA

Temperature	– 40°C to +85°C
Max load	Wind: 2400 Pa, 245 kg/m² front & back Snow: 5400 Pa, 550 kg/m² front
Impact resistance	25mm diameter hail at 23 m/s
Appearance	Class A+
Solar Cells	96 Monocrystalline Maxeon Gen III
Tempered Glass	High transmission tempered Anti-Reflective
Junction Box	IP-65 Rated
Connectors	MC4
Frame	Class 1 black anodised (highest AAMA rating)
Weight	18,6 kg

TESTS AND CERTIFICATIONS

Standard tests	IEC 61215, IEC 61730, UL1703
Quality tests	ISO 9001:2008, ISO 14001:2004
EHS Compliance	RoHS, OHSAS 18001:2007, lead free, PV Cycle
Ammonia test	IEC 62716
Salt Spray test	IEC 61701 (passed maximum severity)
PID test	Potential-Induced Degradation free: 1000V[10]
Available listings	TUV, MCS, UL, CEC

REFERENCES:
1 All comparisons are SPR-X21-345 vs. a representative conventional panel: 240W, approx. 1.6 m², 15% efficiency.
2 PVEvolution Labs "SunPower Shading Study," Feb 2013.
3 Typically 8-10% more energy per watt, BEW/DNV Engineering "SunPower Yield Report," Jan 2013, with CFV Solar Test Lab Report #12063, Jan 2013 temp. coef. calculation;
4 SunPower 0.25%/yr degradation vs. 1.0%/yr conv. panel. Campeau, Z. et al. "SunPower Module Degradation Rate," SunPower white paper, Feb 2013; Jordan, Dirk "SunPower Test Report," NREL, Oct 2012.
5 "SunPower Module 40-Year Useful Life" SunPower white paper, Feb 2013. Useful life is 99 out of 100 panels operating at more than 70% of rated power.
6 Higher than E series which is highest of all 2600 panels listed in Photon Int'l, Feb 2012
7 1% more energy than E-Series panels, 8% more energy than the average of the top 10 panel companies tested in 2012 (151 panels, 102 companies), Photon International, March 2013.
8 Compared with the top 15 manufacturers. SunPower Warranty Review, Feb 2013.
9 Some exclusions apply. See warranty for details.
10 X-Series same as E-Series, 5 of top 8 panel manufacturers were tested by Fraunhofer ISE, "PV Module Durability Initiative Public Report," Feb 2013.
11 Compared with the non-stress-tested control panel. X-Series same as E-Series, tested in Atlas 25+ Durability test report, Feb 2013.
12 Standard Test Conditions (1000 W/m² irradiance, AM 1.5, 25° C).
13 Based on average of measured power values during production.

1046 mm

46 mm

1559 mm

See http://www.sunpowercorp.com/facts for more reference information.
For more details, see extended datasheet: www.sunpowercorp.com/datasheets. Read safety and installation instructions before using this product.
©July 2013 SunPower Corporation. All rights reserved. SUNPOWER, the SUNPOWER logo, MAXEON, MORE ENERGY. FOR LIFE., and SIGNATURE are trademarks or registered trademarks of SunPower Corporation. Specifications included in this datasheet are subject to change without notice.

Bibliography

[1] G. G. Nair, *Photovoltaic charging station for Electric bikes and scooters,* , 152 (2014).

[2] IRENA, *ASHRAE Journal,* Tech. Rep. Jan (2017).

[3] Nishant S. Narayan, *Solar Charging Station for Light Electric Vehicles* (Delft, 2013).

[4] Utrecht University, *2.5 million Dutch households on solar power by 2023 - Universiteit Utrecht,* .

[5] International Energy Agency (IEA), *World Energy Outlook 2016,* (2016), http://www.iea.org/publications/freepublications/publication/ WEB$_W$*orldEnergyOutlook*2015*ExecutiveSummaryEnglishFinal.pdf* , arXiv:978-92-64-26494-6 .

[6] International Energy Agency, *Global EV Outlook 2016 Electric Vehicles Initiative,* Iea , 51 (2016).

[7] Fietsersbond, *Bicycles in figures - Cyclists,* .

[8] University of IOWA, *Electric Vehicle Charging Station- Solar Energy - Renewable Energy - Facilities Management -The University of Iowa,* .

[9] Y. Zhao, *Photovoltaics E-Bike charging station,* (2014).

[10] J. Orgill and K. Hollands, *Correlation equation for hourly diffuse radiation on a horizontal surface,* Solar Energy **19**, 357 (1977).

[11] D. G. Erbs, S. A. Klein, and J. A. Duffie, *Estimation of the diffuse radiation fraction for hourly, daily and monthly-average global radiation,* Solar Energy **28**, 293 (1982).

[12] D. T. Reindl, W. A. Beckman, and J. A. Duffle, *Diffuse fraction correlations,* Solar Energy **47**, 311 (1991).

[13] E. L. Maxwell, *A quasi-physical model for converting hourly global to direct normal insolation,* (1987).

[14] J. E. Hay, *Calculating solar radiation for inclined surfaces: Practical approaches,* Renewable Energy **3**, 373 (1993).

[15] D. T. Reindl, W. A. Beckman, and J. A. Duffie, *Evaluation of hourly tilted surface radiation models,* Solar Energy **45**, 9 (1990).

[16] Perez, R. Seals, R. Stewartt, and D. Menicucci, *A new simplified version of the Perez diffuse irradiance model for tilted surfaces,* Solar Energy **39**, 221 (1987).

[17] R. Perez, P. Ineichen, R. Seals, J. Michalsky, and R. Stewart, *Modeling daylight availability and irradiance components from direct and global irradiance,* Solar Energy **44**, 271 (1990).

[18] M. Lave, W. Hayes, A. Pohl, and C. W. Hansen, *Evaluation of global horizontal irradiance to plane-of-array irradiance models at locations across the United States,* IEEE Journal of Photovoltaics **5**, 597 (2015).

85

[19] M. Z. Arno Smets, Klaus Jäger, Olindo Isabella, Rene Van Swaaij, *UIT Cambridge Ltd.*, June.

[20] A. Jones and C. Underwood, *A thermal model for photovoltaic systems,* Solar Energy **70**, 349 (2001).

[21] M. K. Fuentes, *A Simplified Thermal Model for Flat-Plate Photovoltaic Arrays,* Sandia Report (1987).

[22] J. a. Duffie, W. a. Beckman, and W. M. Worek, *Journal of Solar Energy Engineering*, Vol. 116 (2003) p. 67, arXiv:arXiv:1011.1669v3 .

[23] E. Skoplaki and J. A. Palyvos, *Operating temperature of photovoltaic modules: A survey of pertinent correlations,* Renewable Energy **34**, 23 (2009).

[24] W. De Soto, S. A. Klein, and W. A. Beckman, *Improvement and validation of a model for photovoltaic array performance,* Solar Energy **80**, 78 (2006).

[25] M. Suthar, G. K. Singh, and R. P. Saini, *Comparison of mathematical models of photo-voltaic (PV) module and effect of various parameters on its performance,* 2013 International Conference on Energy Efficient Technologies for Sustainability , 1354 (2013).

[26] J. S. Stein, J. Sutterlueti, S. Ransome, C. W. Hansen, and B. H. King, *Outdoor PV performance evaluation of three different models: single-diode, SAPM and loss factor model,* Proceedings of the 28th European Photovoltaic Solar Energy Conference, Hamburg , 2865 (2013).

[27] N. J. Blair, A. P. Dobos, and P. Gilman, *Comparison of Photovoltaic Models in the System Advisor Model Preprint,* (2013).

[28] C. P. Cameron, W. E. Boyson, and D. M. Riley, *Comparison of Pv System Performance-Model Predictions With Measured Pv System Performance,* , 2 (2008).

[29] *WMO Climate Normals for ALBUQUERQUE/INT'L ARPT NM 1961–1990* (National Oceanic and Atmospheric Administration).

[30] L. Wong and W. Chow, *Solar radiation model,* Applied Energy **69**, 191 (2001).

[31] B. Y. Liu and R. C. Jordan, *The interrelationship and characteristic distribution of direct, diffuse and total solar radiation,* Solar Energy **4**, 1 (1960).

[32] A. Skartveit and J. A. Olseth, *A model for the diffuse fraction of hourly global radiation,* Solar Energy **38**, 271 (1987).

[33] M. Iqbal, *An introduction to solar radiation* (Academic Press, 1983) p. 390.

[34] S. Dervishi and A. Mahdavi, *Computing diffuse fraction of global horizontal solar radiation: A model comparison,* Solar Energy **86**, 1796 (2012).

[35] A. Woyte, R. Belmans, and J. Nijs, *Fluctuations in instantaneous clearness index: Analysis and statistics,* Solar Energy **81**, 195 (2007).

[36] *KNMI - KNMI Kennis- & datacentrum, .*

[37] P. G. Loutzenhiser, H. Manz, C. Felsmann, P. A. Strachan, T. Frank, and G. M. Maxwell, *Empirical validation of models to compute solar irradiance on inclined surfaces for building energy simulation,* Solar Energy **81**, 254 (2007).

[38] D. L. King, W. E. Boyson, and J. A. Kratochvil, *Photovoltaic array performance model,* Sandia Report No. 2004-3535 **8**, 1 (2004).

[39] V. Quaschning and R. Hanitsch, *Shade Calculations in Photovoltaic Systems,* ISES Solar World Conference , 1 (1995).

[40] Meteotest, *Meteonorm: Horicatcher,* .

[41] C. Bern, B. Huguenin-landl, and C. Studer, *Handbook part I : Software Global Meteorological Database Version 7 Software and Data for Engineers , Planers and Education,* (2017).

[42] Trimble, *3D modeling for everyone | SketchUp,* .

[43] P. Ineichen, O. Guisan, and R. Perez, *Ground-reflected radiation and albedo,* **44** (1990).

[44] R. Perez, *The importance of correct albedo determination for adequately modeling energy received by tilted surfaces,* (1987), 10.1016/S0038-092X(87)80016-6.

[45] S. Wang, *Pavement albedo assessment : methods , aspects , and implication,* (2015).

[46] R. Santbergen, V. A. Muthukumar, R. M. Valckenborg, W. J. van de Wall, A. H. Smets, and M. Zeman, *Calculation of irradiance distribution on PV modules by combining sky and sensitivity maps,* Solar Energy **150**, 49 (2017).

[47] V. Weeda, *Solar Powered Infotainment Spot*, Ph.D. thesis, TU Delft (2014).

[48] W. Li, Y. Shi, K. Chen, L. Zhu, and S. Fan, *A Comprehensive Photonic Approach for Solar Cell Cooling,* ACS Photonics **4**, 774 (2017).

[49] D. DTU, *Roughness and Wind Shear,* .

[50] Minitab, *Regression Analysis: How Do I Interpret R-squared and Assess the Goodness-of-Fit?* .

[51] A. Colin Cameron and F. A. Windmeijer, *An R-squared measure of goodness of fit for some common nonlinear regression models,* Journal of Econometrics **77**, 329 (1997).

[52] S. Ransome, J. Sutterlueti, and S. Sellner, *PV technology differences and discrepancies in modelling between simulation programs and measurements,* Conference Record of the IEEE Photovoltaic Specialists Conference , 3061 (2012).

[53] E. Lorenz, T. Scheidsteger, J. Hurka, D. Heinemann, and C. Kurz, *Regional PV Power Production For Improved Grid Integration,* 25th European Photovoltaic Solar Energy Conference and Exhibition / 5th World Conference on Photovoltaic Energy Conversion, 6-10 September 2010, Valencia, Spain. , 6 (2010).

[54] A. P. Dobos, *An Improved Coefficient Calculator for the California Energy Commission 6 Parameter Photovoltaic Module Model,* Journal of Solar Energy Engineering **134**, 021011 (2012).

[55] CEC, *Libraries and Databases | System Advisor Model (SAM),* .

[56] E. Cables, *Photovoltaic Solar PV1-F Cable,* , 1 (2007).

[57] Kip & Zonen, *Solar Radiation Measurements for Solar Energy Applications,* (1830).

[58] H. C. Hottel and B. B. Woertz, *Performance of flat-plate solar-heat collectors,* Transactions of American Society of Mechanical Engineers **64**, 91 (1942).

A

Glossary

A.1. List of Acronyms

PV   Photovoltaic

KNMI   Koninklijk Nederlands Meterological Instituut

CESAR   Cabauw Experimental Site for Atmospheric Research

GMT   Greenwich Mean Time

GHI   Global Horizontal Irradiance

DHI   Diffuse Horizontal Irradiance

DNI   Direct Normal Irradiance

POA   Plane of Array

ER   Erbs

OH   Orgill and Hollands

Re   Reindl

DISC   Direct Insolation Simulation Code Model

RMSD   Root Mean Square Difference

MBD   Mean Bias Difference

RD   Relative Difference

CRSS   Composite Residual Sum Square

MATLAB   Matrix Laboratory

EEMCS   Electrical Engineering, Mathematics and Computer Science

CEG   Civil Engineering and Geoscience

AM   Air Mass

SF   Shading Factor

SVF   Sky View Factor

Al   Albedo

LT   LightTools

SK   Sketchup

FD   Fluid Dynamic

NOCT   Nominal Operating Cell Condition

STC   Standard Test Conditions

SDM   Single Diode Model

PVM   Point Value Model

DC   Direct Current

NREL   National Renewable Energy Laboratory

SAM   System Advisory Model

CIGS   Cadminum Indium Gallium Selenide

A.2. List of symbols

k_t Clearness index

k_d Diffuse fraction

k_{tm} Modified clearness index (Dutch-I and Dutch-II)

E_a Extraterrestial irradiance

E_{sc} solar constant

θ_z Solar zenith angle

n Number of samples

α_s Sun elevation angle

A_s Sun azimuth angle

Am Module azimuth angle

θ_i Angle of incidence on module

G_{POA} Irradiance on plane of array

G_{dir} Direct beam irradiance

G_{ground} Ground reflected component

W_s Wind speed

T_{NOCT} Module temperature are NOCT

T_{amb}	Ambient temperature
η	Module efficiency
T_m	Module temperature
α	Absorption by Solar Module
τ	Transmission coefficient of solar module
T_{cell}	Cell temperature
V_{oc}	Open-circuit voltage
I_{sc}	Short- circuit current
V_{mpp}	Maximum Power point Voltage
P_{mpp}	Maximum Power Point Power
I_{mpp}	Maximum Power point Current